SiOx-SiCz MEMS-DBR-Based Tunable Optical Devices

Cesar, Julijan

(2020)

SiO_x-SiC_z MEMS-DBR-Based Tunable Optical Devices

Vom Fachbereich Elektrotechnik und Informationstechnik
der Technischen Universität Darmstadt
zur Erlangung der Würde eines
Doktor-Ingenieurs (Dr.-Ing.)
genehmigte

Dissertation

von

M.Sc.
Julijan Cesar
geboren am 18.08.1987
in Tettnang, Deutschland

Referent:	Prof. Dr. rer. nat. Thomas Kusserow
Korreferent:	Prof. Dr. rer. nat. habil. Stefan Sinzinger
Tag der Einreichung:	17.03.2020
Tag der mündlichen Prüfung:	25.06.2020

D17
Darmstadt 2020

Cesar, Julijan: SiOx-SiCz MEMS-DBR-Based Tunable Optical Devices
Darmstadt, Technische Universität Darmstadt
Jahr der Veröffentlichung der Dissertation auf TUprints: 2020
URN: urn:nbn:de:tuda-tuprints-135633
Tag der mündlichen Prüfung: 25.06.2020

Erkärungen laut Promotionsordnung

§8 Abs. 1 lit. c PromO
Ich versichere hiermit, dass die elektronische Version meiner Dissertation mit der schriftlichen Versionübereinstimmt.

§8 Abs. 1 lit. d PromO
Ich versichere hiermit, dass zu einem vorherigen Zeitpunkt noch keine Promotion versucht wurde.

§9 Abs. 1 PromO
Ich versichere hiermit, dass die vorliegende Dissertation selbstständig und nur unter Verwendung der angegebenen Quellen verfasst wurde.

§9 Abs. 2 PromO
Die Arbeit hat bisher noch nicht zu Püfungszwecken gedient.

Darmstadt, den 17.03.2020

_____

Julijan Cesar

Acknowledgment

This work could not have flourished without the support and opportunities given by people accompanying my path.

First of all, I am thankful that my three supervising professors gave me the opportunity to investigate and finish such an exciting topic. I am grateful to Prof. Dr.-Ing. Franko Küppers, who offered me this position back in 2014, after I decided to pursue a PhD. He offered me freedom in my work and did not hesitate when new opportunities appeared. During his leave, Prof. Dr. rer. nat. Thomas Kusserow took over the role as supervisor. I would like to show my greatest appreciation for his new insights and viewing points towards my topic, which offered me the opportunity to extend my investigations remarkably. I am grateful to Prof. Dr. rer. nat. Sascha Preu who supported me immensely during my last year by including me in his own group.

Secondly, I am thankful for all my colleagues for a wonderful, relaxed and professional working atmosphere. Foremost I thank Dr.-Ing. Sujoy Paul for introducing me into the world of MEMS-VCSEL devices and helping me not to give up during long hours of intensive clean-room fabrication. We could always discuss and find solutions for any problem. Dear Dr.-Ing. Tanvir Haidar, I am very grateful for all comments and suggestion on topics involving filters, setups and measurement peculiarities. I would like to express my gratitude to Ahid Hajo, my years-long office mate, for all the encouragement during times when motivation was at a low, and of course, for the fun times we shared in our office. Further, I am happy to have been at IMP at the same time as Dr.-Ing. Mohammadreza Malekizandi, Yasameen Al-Mafrachi, Dr.-Ing. habil. Oktay Yilmazoglu, Dr. rer. nat Trung Le, Dr.-Ing. Ali Emsia, Dr.-Ing. Christian Gierl, Alaa Saleh, Dr. Velimir Ilić, Dr.-Ing. Alex Wiens, Dr.-Ing. Bernd Kubina und Ion Oprea. I am indebted to Amlan Mukherjee, Fahd Faridi, Anuar Fernandez,

Uttam Nandi, Dr.-Ing. Stefan Regensburger and Mario Aller for their open-hearted welcome to their group in 2019. Without you, I couldn't have finished the last couple of stressful months.

I would particularly like to thank Andreas Semrad for his helping hands. On many occasions, he repaired all clean-room systems. Especially our PECVD reactor offered a new fault to identify each time it stopped working, certainly in the most time-critical moments imaginable. Through him, I learnt a great deal about how, or why not, fabrication facilities work. Further, I have greatly benefited from Dr. -Ing. Holger Maune, Peter Kießlich and Silke Schober through their help in solving additional technological issues arising every now and then.

I am deeply grateful for my friendships to people I met a long time ago in FN, KN, Maha Sarakham, who are still by my side when an adventure calls.

I owe my deepest gratitude to my Madeleine for her constant support, her motivating words, her smile and warmth during times of motivational decrepitude. She always helped me in every situation and showed me solutions where I only saw problems. I couldn't have finished this work without her. Seeing her discipline motivated me as much as her weekly Bürosnacks which kept me going and my energy levels high. We created a home together where we can see life beyond occupational duties.

Lastly, I would like to thank my mother for opening such possibilities for me, to be able to move from home, to study and dare the next step of doing a PhD. I am indebted to her calming nature, offering true relaxation during visits or holidays, supported by my brother, both showing me what it is to be home.

Julijan Cesar

Darmstadt
17.03.2020

Abstract

Wavelength tunable devices are required in many fields like spectroscopy of gases, biomedical absorption experiments, wavelength division multiplexing in optical data networks, among others. Usually the devices are limited by the technology implemented to change the transmitted frequencies and are specific to their usage scenario. Thus extending the regime in which a single device can function, will reduce the need for many different devices with a narrow application window. For example, having a tunable laser for telecommunication networks around 1550 nm, that can support both L- and C-bands (1530 nm to 1625 nm). It opens much more flexibility, either by applying new coding mechanisms that require wavelength switching. Or simply by reducing storage requirements, because only one type of device serves as hot-backup for all channels.

Investigation on tunable lasers on the basis of a VCSEL (vertical cavity surface emitting laser) in combination with a SiO_x-SiN_y MEMS-DBR, which offer up to 107 nm of tuning around 1550 nm, went on for more than two decades. It is time to overcome the material-specific limitation of those DBR materials. With a refractive index difference of 0.45 only 120 nm of high reflectivity around 1550 nm are supported by SiN_y and SiO_x.

In this work, silicon carbide (SiC_z) is introduced as a replacement for SiN_y to grow DBR stacks with a refractive index contrast of 1, when paired with SiO_x. This increases the reflectivity stopband by more than a factor of 2, while the number of layer pairs is reduced for similar maximum reflectivities. So, in the end, wider tuning and smaller devices are feasible.

The first step towards a MEMS-DBR tunable Fabry-Pérot VCSEL is investigating the behavior of the new material by processing passive filters based on the same principle. MEMS stands for micro-electro-mechanical system. Here a Farby-Pérot resonator consisting of two DBRs - one fixed, one movable - and an adjustable air-gap in between, enables continuous shifting of the resonant wavelength through displacement of the MEMS-DBR. After investigations on single layers deposited by low-temperature PECVD to enable compatibility

with the active substrates, layer stacks are grown and structured into MEMS-DBRs. They can be actuated electro-thermally and electro-statically to tune the resonator cavity length and ultimately the transmission wavelength. First tests provided proof that the idea is working, but the tuning range was limited by the large cavity length.

To increase the free spectral range, the cavity length had to be reduced. By creating a Comsol Multiphysics model for SiO_x-SiC_z MEMS-DBR, harnessing packages for structural mechanics and electro-thermal physics, the number of experimental testing could be lowered. Changing several variables led to the need of reducing the lateral MEMS-size by at least a factor of 2. After a redesign of the photolithography masks, new small-sized MEMS were processed successfully, reducing the air-gap to the desired lengths of 1 µm to 4 µm.

Those new devices could be tuned over 250 nm, limited only by the measurement equipment. Moreover, increasing the number of layer pairs of the DBR decreased transmission linewidth below 30 pm (or 4 GHz) over a tuning range beyond 250 nm around 1550 nm.

MEMS-DBR surface-micro-machining technology was furthermore transferred to both photodiode and half-VCSEL substrates successfully. Both SiO_x-SiN_y and SiO_x-SiC_z MEMS-DBR tunable photodiodes were able to detect and separate two neighboring lasers in a dense wavelength division multiplexing grid with 100 GHz (or 0.8 nm) spacing.

SiO_x-SiC_z MEMS-DBR VCSELs showed a tuning range of only 57 nm around 1530 nm due to processing related issues. A much higher potential for wider tuning is available, but could not be achieved within the time frame of this work. Nevertheless, SiO_x-SiC_z MEMS-DBR VCSEL were found to be much less prone to temperature changes, considering emission wavelength shift, than SiO_x-SiN_y MEMS-DBR VCSEL published previously. This decreases environmentally induced temperature-dependent wavelength changes immensely.

Kurzfassung

Wellenlängenabstimmbare Bauteile werden in vielen Bereichen benötigt, für Spektroskopie von Gasen, bei biomedizinischen Absorptionsexperimenten, in wellenlängenmultiplex Netzwerken zur optischer Datenübertragung und vielen weiteren. Üblicherweise sind die Abstimmbereiche der Bauteile durch die eingesetzte Technologie begrenzt, sodass sie sehr spezifisch für ihren Einsatzbereich konstruiert werden müssen. Wenn der Bereich nun erweitert wird, kann ein einziges Bauteil für mehrere Einsatzzwecke benutzt werden, wodurch die Menge an benötigten unterschiedlichen Geräten verringert werden kann. Zum Beispiel kann ein wellenlängenabstimmbarer Laser für ein optisches Datennetzwerk um 1550 nm verwendet werden, welcher sowohl das L- als auch das C-Band bedienen kann (1530 nm bis 1625 nm). Dies erlaubt eine erhöhte Flexibilität, sei es durch das Ermöglichen von Modulationsverfahren, welche eine Änderung der Wellenlänge fordern. Oder es verringert den benötigten Lagerbedarf, da nur noch eine Sorte an Ersatzlasern für alle Kanäle bereitgehalten werden muss.

In den vergangenen zwei Jahrzehnten wurden wellenlängenabstimmbare Laser vorgestellt, einer Kombination aus VCSEL (oberflächenemittierende Halbleiterlaser) und SiO_x-SiN_y MEMS-DBR, welche bis zu 107 nm Abstimmung um 1550 nm erlauben. Nun ist es an der Zeit die materialspezifischen Beschränkungen dieser Braggspiegel (DBR) zu überwinden. Der Einsatz von SiN_y und SiO_x erlaubt nur einen Brechungsindexunterschied von 0,45 und damit nur eine Stopbandbreite hoher Reflektivität um 1550 nm von 120 nm.

In dieser Arbeit wird Siliziumcarbid (SiC_z) als Ersatz für SiN_y vorgestellt. Gepaart mit SiO_x sind dadurch Braggspiegel mit einem Brechungsindexunterschied von 1 möglich. Dies verdoppelt die Stoppbandbreite und reduziert gleichzeitig die benötigte Anzahl an Schichtpaaren, um dieselbe Reflektivität zu erlangen. Letztendlich wird dadurch der Abstimmbereich erweitert und die Möglichkeit zur Verringerung der Bauteile erschaffen.

Der erste Schritt zu einem MEMS-DBR abstimmbaren Fabry-Pérot VCSEL ist die Untersuchung des neuen Materials in Form von passiver Filter, agierend nach demselben Prinzip. MEMS steht dabei für mikroelektromechanisches System.

Ein Fabry-Pérot Resonator besteht hierbei aus zwei Braggspiegeln - einem festen und einem beweglichen - welche durch einen veränderbaren Luftspalt voneinander getrennt sind. Durch eine Verschiebung des beweglichen MEMS-DBR kann die resonante Wellenlänge kontinuierlich verändert werden. Zunächst wurden einzelne Schichten untersucht, gewachsen durch eine plasmaunterstützte Gasphasenabscheidung (PECVD) bei niedrigen Temperaturen, um die Prozessverträglichkeit mit den VCSEL Substraten zu gewährleisten. Danach wurden Schichtstapel abgeschieden und in der MEMS Form strukturiert, welche schließlich sowohl elektrothermisch, als auch elektrostatisch ausgelenkt werden konnten, um die Resonatorlänge und schließlich die Transmissionswellenlänge zu verändern. Erste Test zeugten von Erfolg, jedoch war der Abstimmbereich durch die große Resonatorlänge begrenzt.

Um den freien Spektralbereich zu vergrößern musste die Kavität verkleinert werden. Durch das Erstellen eines Comsol Multiphysics Modells für SiO_x-SiC_z MEMS-DBR, welches Pakete für strukturmechanische und elektrothermische Begebenheiten verwendet, konnte die Anzahl an experimentellen Versuchen verringert werden. Veränderungen von verschiedenen Parametern ergab, dass die laterale Größe der MEMS mindestens um den Faktor 2 verkleinert werden muss. Der Luftspalt konnte durch eine entsprechende Umgestaltung der Photolithographiemasken auf 1 µm to 4 µm erfolgreich reduziert werden.

Diese Filter konnten um mehr als 250 nm um 1550 nm abgestimmt werden. Begrenzt war dies lediglich durch die Messgeräte. Darüber hinaus hat die Erhöhung der DBR Schichtpaare eine schmale Transmissionsbandbreite unter 30 pm (oder 4 GHz) über einen Abstimmbereich von über 250 nm um 1550 nm zur Folge.

Die MEMS-DBR Oberflächenmikrostrukturierungstechnologie wurde nach erfolgreichen Tests mit Filtern auf Photodioden- und VCSEL-Substrate übertragen. Sowohl SiO_x-SiN_y, als auch SiO_x-SiC_z MEMS-DBR abstimmbare Photodioden konnten benachbarte Laser eines DWDM Rasters von 100 GHz oder 0,8 nm detektieren und unterscheiden.

SiO_x-SiC_z MEMS-DBR VCSEL zeigten lediglich einen Abstimmbereich von 57 nm um 1530 nm aufgrund von prozessbedingter Aspekte. Das große Potential für einen viel größeren Abstimmbereich konnte innerhalb des Zeitfensters dieser Arbeit nicht mehr ausgeschöpft werden. SiO_x-SiC_z MEMS-DBR abstimmbare VCSEL zeigen aber bereits jetzt eine viel kleinere Empfindlichkeit auf Temperaturschwankungen im Vergleich zu bisher veröffentlichten SiO_x-SiN_y MEMS-DBR VCSEL. Dies verringert den äußeren Einfluss auf temperaturbedingte Wellenlängenänderung drastisch.

Contents

List of Figures

List of Tables

1 Introduction

We live in a world which more and more relies on decentralized data-storage and processing. All files need to be accessed remotely, stored in clouds, backed-up automatically. We grow more and more dependent on online services feeding us with information, entertainment or knowledge. In the past newspapers were, for example, the most recent collection of news, now the time between an event and the report or live footage on it, races towards zero. We need to know everything immediately. In the opposite direction, people feel the need to share every aspect of their life through networking services. So not only direction from a data center, where the information is stored, but also the upload from millions of users towards the data center will grow in its demand.

Further examples which need large up- and download speeds, are growing distrust in large companies which offer paid or free services for data-storage, causing individuals to move to self-hosted servers in private households. Decentralized video games are currently arising, although not yet showing the same experience as local machines, due to response time between the user input and the software's reaction. However, in general, the idea is good if implemented with user-friendly contracts in mind. Thus, demand only arises while people are awake, reducing the requirement for powerful local hardware and sharing decentralized processors.

In industrial areas currently, companies are globally connected. The entire knowledge is not located at the headquarter, but spread over numerous locations, subcontractors or partners, specialized in their topics. To manage to work together, they need to be connected via networks. For example, while today, many operations are handled in person by employees travelling to each site discussing and taking decisions. In the future, this might reduce because people might, at some point, change their view towards the environment. Many demonstrations in recent years raise awareness of climate change and personal influences. This change will probably come faster than expected supported by current pandemic spreading of a viral disease, which does stop people from travelling quite effectively. Suddenly discussions and decisions can be handled

via the internet. In the future companies might increase the demand for live video transmission. When paying customers depend on such a technology, it has to be stable, reliable and mostly it has to be fast to ensure high quality. Among other applications, here response time is essential. Time difference between input on one end and output on the other end needs to be minimal to be able to have real-life-like discussions.

High-speed modulated lasers send data pulses through glass fibers, enabling data transmission. Equally fast responding detectors receive the signal on the other end. Using light to transfer information holds many advantages. It is fast, is not influenced by the environment; it works with a low power budget and is relatively secure towards manipulations from outside. The first possibility to transmit digital data is to turn it on and off to generate two states, 1 and 0. The second step is to do this very fast, reaching several tens of GHz. Here lies the limit for one laser emitting at one wavelength located at a minimum loss of the transmitting medium (around 1550 nm for a glass fiber). Higher-order modulation schemes increase the transmission capacity of a laser, by using more than two states or utilizing orthogonal polarization of light. This increases capacity by a factor of 4 or 8. Ultimately more than one wavelength is required. Although losses are at a minimum at 1550 nm, the region around it does also experience low losses. Now several wavelengths can travel in one fiber simultaneously carrying independent data streams. Such a battery of lasers spaced by 100 GHz or approximately 0.8 nm allow 40 channels in the C-band (1530 nm to 1565 nm). Additional channels can be found in the L-band (1565 nm to 1620 nm). Reducing the spacing to 50 GHz or 25 GHz increases capacity accordingly.

For each channel in a wavelength-multiplexing network, separate semiconductor lasers handle one specific channel each. For each laser, several backup units need to be kept in storage all over the world, which is expensive and requires managing of resources. The solution is a wavelength-tunable laser, which can be set to the required channel while in use. Now a hot-backup is in storage which can replace every single channel. This flexibility could even support the redesign of a system on the fly if for example a smaller spacing should be used at one point. A tunable laser selects the required wavelength itself. Such high-speed vertical-cavity surface-emitting lasers (VCSEL) were published for 10 Gbps and a tuning range of 85 nm for telecom wavelengths and a continuous wavelength tuning range of 107 nm [57, 60]. A VCSEL is especially interesting for fiber-based communication due to the possibility to create a circular output beam, which has an excellent coupling efficiency. The tuning mechanism for those lasers relies on a MEMS-DBR mirror with adjustable air-gap L_{air}, shown

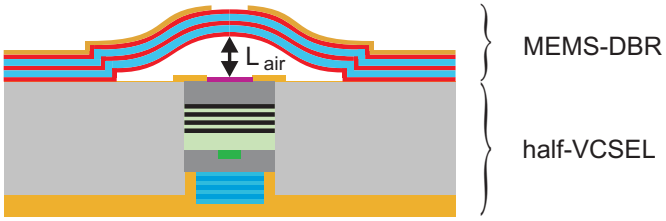

Figure 1.1: Cross-section of a MEMS-DBR VCSEL with a tunable air-gap L_{air}.

in fig. 1.1. MEMS stands for a micro-electro-mechanical system (MEMS), an integrated system on a micrometer scale, combining electrical and moving mechanical components, connected by thermal or electrostatic phenomena. A DBR is a distributed Bragg reflector consisting of alternating layer pairs with high and low refractive index, creating a highly reflective mirror with a wide stopband.

Determined by the cavity length, the resonant wavelength emerges from the output aperture. Two factors are essential for wide tunability. The first is the active medium itself. It needs a wide gain so that stimulated emission can occur. Strained quantum wells buried in the semiconductor enable such an active region. The second factor is mirrors with high reflectivities for an equal or broader wavelength range. Because VCSELs are grown epitaxially, the active region only offers a thickness in the sub-micrometer range. Mirrors with reflectivities beyond 99.5 % overcome the threshold gain because the light crosses the active region multiple times. A DBR fulfils such requirements. In the case of previously mentioned< publications, these materials are dielectrics SiO_x and SiN_y. The defining parameter is the refractive index difference of 0.45, which creates a high-reflectivity stopband of 120 nm.

Halbritter presents tunable pin-photodiodes based on SiO_x-SiN_y MEMS-DBR fabricated with bulk-micromachining [27]. The free spectral range limits the tuning range to 44 nm. Surface-micromachining, used in this work, opens the possibility for fabricating numerous devices on one chip.

To improve the tuning range of previous devices based on SiO_x-SiN_y MEMS-DBR, now silicon carbide (SiC_z) is being introduced. SiC_z is well established technologically and can be deposited with a low-temperature PECVD creating amorphous layers. Moreover, due to the presence of H atoms in the reaction chamber removed from SiH_4 during plasma deposition, they are incorporated as well. The resulting layer composition might look like the presentation in fig. 1.2. SiC_z has previously been used for MEMS applications as well, such as

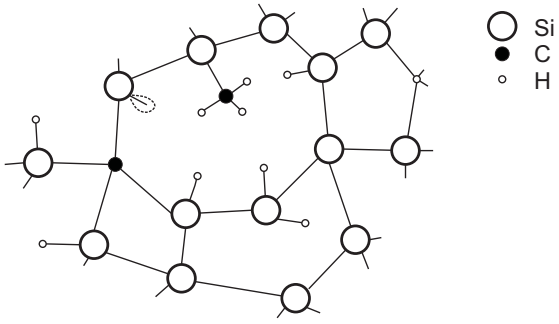

Figure 1.2: Proposed structure of an amorphous SiC_z layer deposited with SiH_4 and CH_4 precursor gases, according to [1].

cantilevers with electro-thermal actuation or high-temperature applications [19, 36].

The main advantage of a plasma deposited SiC_z layer is its high refractive index around 1550 nm of 2.56 [72, 76] for hexagonal crystal 6H-SiC_z polytype. Assisted ion-beam deposition resulted in a refractive index of 2.6 [14]. Even a value 3.18 for thin-films was claimed by [40, 41], although their main focus was on extreme UV characterization. The layers deposited in this work - with low-temperature PECVD - show a refractive index of approximately 2.45. The high refractive index is important for DBR, creating a wider reflectivity stopband, required for widely tunable resonators. In combination with SiO_x, a refractive index difference of 1 can be achieved. Higher index contrast also reduces the number of layer pairs required for high reflectivity. Presented in [22], calculations for much wider tunability based on SiO_x-SiC_z MEMS-DBR approach in comparison to well-investigated SiO_x-SiN_y MEMS-DBR, are presented. Here especially refractive index difference supports the suitability for this task.

SiC_z is widely used in extreme environments as a base material for high frequencies, high power, high voltages and high temperatures [33, 45]. Another application that overlaps with the goal of this work is MEMS or NEMS, because of its easy integrability with Si-based micro-fabrication technology [35, 36]. Low temperature processing below 400 °C and even as low as 80 °C used in this work, does offer suitability for IC compatible MEMS processing [35, 69].

Looking at the absorption in the near-infrared region around 1550 nm does show measurable values above zero [23, 40] of approximately $k = 0.03$. Thus, discussing the SiO_x-SiC_z MEMS-DBR transmission requires the consideration of absorption. Nevertheless, wide reflectivity stopband should outweigh the disadvantages.

Another candidate is titanium dioxide (TiO_2) which can be deposited with low-temperature PECVD as well. Precursor titanium tetra-isopropoxide $Ti(OC_3H_7)_4$ in liquid form is used, which was not available for the PECVD reactor at our institute. Moreover, no absorption is present in NIR. While an older publication reports a similar refractive index of 2.45 [17] more recent studies only show a value of 2.28 for an atomic layer deposition [71] and 2.06 by e-beam evaporation [68]. Furthermore amorphous silicon (a-Si) offers a very high refractive index of $n_{\text{a-Si}} = 3.38$ with zero absorption [64]. Deposition at low temperatures is possible, but in order to reduce layer stress to values needed in this work, still, a deposition temperature of 200 °C is required which is too high to work with half-VCSEL samples [32].

In conclusion, albeit having some absorption in the NIR, SiC_z offers the best combination of deposition possibilities and layer properties. After the successful development of the SiO_x-SiC_z MEMS-DBR technology, it is applied to photodiode and VCSEL substrates. For both previous publications for MEMS-tunable devices exist, but limited in their tuning ranges.

Thesis Overview

This thesis is divided into six chapters. The introduction gives a motivation for investigating SiO_x-SiC_z MEMS-DBR and tunable devices in general.

Chapter 2 sheds light on the physics of a MEMS-DBR approach to tunable devices. First, propagation of light in vacuum and media is described to understand, what happens at interfaces between two different materials. Next, the effects of transmission, reflection and resulting interferences of many waves are used to understand a Fabry-Pérot resonator and which conditions have to be met to create a stable cavity. Next, the influence of optical thin-films on the reflectivity of substrates is investigated to create both anti-reflective coatings (ARC) and distributed Bragg reflectors (DBR) with very high reflectivities within a broad stopband. Combining a Fabry-Pérot principle with MEMS-DBR mirrors eventually opens the possibility to create stable tunable filters. Moreover, processing basics like deposition and structuring of dielectrics are presented along with optical and structural characterizations. Here, especially ellipsometry to determine optical constants and measurements of layer stress are essential. Furthermore, photolithography to structure each layer and depositions of metal layers are presented. At the end of chapter 2, the basics of photodiodes and VCSELs are presented to understand their fundamentals.

In chapter 3, step by step designing of a SiO_x-SiC_z MEMS-DBR is performed. First, single layer deposition parameters of plasma-enhanced chemical vapor deposition (PECVD) are examined to create a layer with suitable layer stress. Next, the requirements for a DBR are presented. Stability of depositions is essential because a DBR deposition can take several hours, and reproducibility of the desired layer is crucial. After growing a DBR, it needs to be structured by dry-etching in a fluoride-containing plasma. Finally, the connection between the displacement of the MEMS-DBR and resulting wavelength-shift is investigated by simulating corresponding layer stacks and solving it by transfer matrix method.

In chapter 4, experimental results of fabricated and characterized passive SiO_x-SiC_z MEMS-DBR filters are summarized. First, standard-sized photolithography masks from previous works are used. Processing is shown in a step-by-step procedure. Next, the behavior of tuning by electro-thermal MEMS current and the change of substrate temperature are presented. Moreover, transmission linewidth is shown for both SiO_x-SiN_y and SiO_x-SiC_z MEMS-DBR filters. Since this MEMS size does not result in an extensive tuning range, a Comsol model for SiO_x-SiC_z MEMS-DBR is developed to minimize experimental testing by predicting the air-gap. This resulted in the reduction of MEMS-arm sizes by at least a factor of 2. Subsequently, such photolithography masks are designed, and new small-sized SiO_x-SiC_z MEMS-DBR filters are produced. Those devices enable much broader tuning ranges. Furthermore, an increase of DBR layer pairs shows a remarkable reduction in the transmission linewidth. Lastly, SiO_x-SiC_z MEMS-DBR filters are fabricated with an additional electrode to enable electro-static actuation.

Finally, in chapter 5, MEMS-DBR technology is transferred to both photodiode and half-VCSEL substrates to create tunable receivers and sources, respectively. Both SiO_x-SiN_y and SiO_x-SiC_z MEMS-DBR photodiodes can be tuned electro-thermally. SiO_x-SiC_z MEMS-DBR VCSELS are tunable across a limited tuning range and mark the first step towards much wider tuning ranges and higher temperature stability than previously published with SiO_x-SiN_y MEMS-DBR VCSEL.

The work concludes with a summary and an outlook in chapter 6.

Appendices A to C give more details on chemical reactions, present additional graphs on DBR reflectivity and show the newly designed small-sized photolithography masks, respectively.

2 MEMS-DBR Approach to Tunable Devices

A Fabry-Pérot resonator consists of two highly reflective broadband mirrors (DBRs) at a specific distance, determining the cavity length and the resonant wavelengths. Tunable devices presented in this work, are based on adjustable cavity lengths realized by a movable mirror. One surface is flat, while the other is a concavely bent, displaceable MEMS-DBR. Thus, a change in cavity length induces a shift in the resonant wavelength, which defines a tunable device. The first section presents light propagation through matter, including reflection and transmission at interfaces to understand how light travels through dielectric layers. A Fabry-Pérot resonator relies on the interference of many waves. Similarly, a multilayered DBR uses interference to create highly reflective broadband mirrors, required for narrow filtering and broad wavelength tuning. Two different tuning mechanisms to adjust cavity length follow, either by thermal heating induced through a heating current or an electrostatic force exerted by two electrodes. Certain technologies are required to build a MEMS-DBR (distributed feedback reflector), which are presented in detail. Finally two modules - detector and laser source - are shown in the last two sections of this chapter, because the ultimate goal is to create not only passive tunable filters but also active tunable detectors and laser sources.

2.1 Theory of Light Propagation

Property of Light

Light as a wave has two main properties. The first property is the wavelength λ, which describes the distance between two points with the same phase. In this work the infrared region is investigated, where $\lambda \approx 1550\,\text{nm}$, corresponding to a frequency of 193.4 THz. The second property is the speed of light $c_0 \approx 3 \cdot 10^8\,\text{m/s}$ in vacuum (absence of molecules and atoms). The wave property of

light enables superposition by adding up all amplitudes of the electrical fields of all waves at a distinct point to receive their resulting sum. When two waves with the same wavelength are in phase, constructive interference is the result. If they are out of phase 180° (the distance between both maxima is $\lambda/2$) they interfere destructively, cancelling out each other entirely at each point in space, given they have the same amplitude and wavelength.

The direction of propagation in a homogeneous medium is always forward, described by the Huygens-Fresnel principle. It assumes each point of the wavefront is the source for a new spherical wave. These secondary waves interfere with each other, resulting in a plane wavefront travelling in a straight line. In case of low-density environments like gases, where the mean distance between molecules is larger than the wavelength λ and the distance between any two molecules is not constant over time, scattering of light creates random phases in lateral and backward directions. In case of an optically dense material like solids or liquids (within a cube with side length λ many molecules are present) there is always deconstructive interference of emitted waves in both lateral and backward direction. Due to the small and constant mean distances between molecules, the condition of $\lambda/2$ is always met for two emitted waves. There are always pairs of oscillators that cancel out each other in lateral and backward direction [29, 15]. The forward direction is independent of molecule distribution, creating a plane wavefront. Interferences create a redistribution of energy due to energy conservation. There is extinction in certain regions (lateral direction) and enhancement in other directions (forward direction), the only possibility for the propagation of light is forward. While light is travelling forwards through a medium, as mentioned before, there are primary and secondary waves. The primary wave excites an electron of a molecule, which itself emits a secondary wave if the photon energy is too low for absorption. The secondary wave shows a phase shift of approximately 90° towards the primary wave. Both waves travel at the speed of light in the space between the molecules. In most cases (frequency $\omega < \omega_0$, where ω_0 is the material-dependent resonance frequency), the combination of both waves lags behind the primary wave with a phase shift of 90°-180°. In other words, the propagation speed c within a medium is less than the travelling speed of photons (speed of light c_0). The refractive index n defines the proportionality, where

$$c = c_0/n. \tag{2.1}$$

The refractive index abstractly describes the damping of the oscillator - the molecule. Intensity is unaffected when the absorption of the molecule is zero. If the damping is high, more time is required for the oscillator to remit the

secondary wave, thus delaying the combined wave by a greater extent. Propagation is slower in a high refractive index material.

Next, a light beam is considered traveling through air ($n_{air} = 1$) incident perpendicularly on a glass surface ($n_{glass} = 1.4$). A sudden refractive index change Δn occurs (change of refractive index within a distance of less than $\lambda/4$). Here propagation direction is not limited to forward any more. Close to the surface of a medium, there is an asymmetric distribution of oscillators. Within a distance of $\lambda/2$ no pairs of oscillators to cancel out each other exist anymore, as $n_{air} \neq n_{glass}$. This creates reflection and transmission simultaneously. Light propagates both in backward and forward directions from the air-glass interface. Reflection and transmission intensity is defined by the ratio of refractive indices according to eqs. (2.9) and (2.10).

Light Propagation in Dielectrics

A dielectric material is electrically neutral and does not conduct electric current. (More details on the differences between dielectrics, semiconductors and metals is presented in section 2.6.) Within a dielectric media, the propagation velocity of electromagnetic waves is given by

$$c = (\varepsilon_R \varepsilon_0 \mu_R \mu_0)^{-1/2}, \tag{2.2}$$

where

ε_R is the dielectric constant (relative permittivity) of the medium
ε_0 is the electric permittivity of free space
μ_R is the relative permeability of the medium and
μ_0 is the magnetic permeability of free space.

So, in conclusion, it is the speed c_0 in free space, affected by the presence of the medium.

$$c = \frac{c_0}{(\varepsilon_R \mu_R)^{1/2}} = \frac{c_0}{n}, \tag{2.3}$$

which results in equation 2.1. In a dielectric medium in general $\mu_R \approx 1$ and $\varepsilon_R > 1$, so

$$n \approx \sqrt{\varepsilon_R} \tag{2.4}$$

All media investigated within this work (such as silicon (Si), silicon oxide (SiO_x), silicon nitride (SiN_y), silicon carbide (SiC_z) and air) are dielectrics.

Reflection and Transmission

As mentioned before, at the occurrence of a rapid refractive index change, light is split into reflection and transmission. When light incides at an angle Θ_i, reflection angle Θ_r and transmission angle Θ_t can be described with the law of reflection

$$\Theta_r = \Theta_i \tag{2.5}$$

$$\sin\Theta_t = \frac{n_i}{n_t} \cdot \sin\Theta_i, \tag{2.6}$$

where n_i is the refractive index of the incidence medium and n_t is the refractive index of the transmission medium. With these equations, which base on the assumption of boundary conditions for a continuous component of the electric field $\vec{E}$ tangential to the interface is equal in both media, it is possible to derive the Fresnel equations. They describe both amplitude reflection and amplitude transmission coefficients r and t, respectively in perpendicular and parallel polarization according to eqs. (2.7) and (2.8)

$$r_\perp = \left(\frac{E_r}{E_i}\right)_\perp = \frac{n_i\cos\Theta_i - n_t\cos\Theta_t}{n_i\cos\Theta_i + n_t\cos\Theta_t}, \quad -r_\parallel = \left(\frac{E_r}{E_i}\right)_\parallel = \frac{n_t\cos\Theta_i - n_i\cos\Theta_t}{n_i\cos\Theta_t + n_t\cos\Theta_i}, \tag{2.7}$$

$$t_\perp = \left(\frac{E_t}{E_i}\right)_\perp = \frac{2n_i\cos\Theta_i}{n_i\cos\Theta_i + n_t\cos\Theta_t}, \quad t_\parallel = \left(\frac{E_t}{E_i}\right)_\parallel = \frac{2n_i\cos\Theta_i}{n_i\cos\Theta_t + n_t\cos\Theta_i}. \tag{2.8}$$

A distinction between an electric field perpendicular $E_\perp$ (s-polarized) and parallel $E_\parallel$ (p-polarized) to the plane of incidence needs to be taken into account, which is why there are in total four Fresnel equations. In the particular case of perpendicular incidence angle ($\Theta_i = 0$), used in this thesis, the following equations follow:

$$r_\perp = \frac{n_i - n_t}{n_i + n_t}, \qquad -r_\parallel = \frac{n_t - n_i}{n_i + n_t} \tag{2.9}$$

$$t_\perp = \frac{2n_i}{n_i + n_t}, \qquad t_\parallel = \frac{2n_i}{n_i + n_t}. \tag{2.10}$$

With these equations it is immediately visible, that reflection amplitude is large with a larger refractive index difference $\Delta n = |n_1 - n_2|$ between medium 1 (n_1) and medium 2 (n_2). Also it can be seen, that $r_\perp$ is negative for $n_t > n_i$. A change of sign for the electric field E_t means a phase shift of π. Finally, the reflectivity

R can be defined as the ratio of incident power ($I_\mathrm{i} A \cos\Theta_\mathrm{i}$) and reflected power ($I_\mathrm{r} A \cos\Theta_\mathrm{i}$), where I_i and I_r are the flux densities for incidence and reflected wave and A is the area of the beam. Since both incident and reflected waves are propagating within the same medium, the reflectivity is

$$R = \frac{I_\mathrm{r} A \cos\Theta_\mathrm{i}}{I_\mathrm{i} A \cos\Theta_\mathrm{i}} = \frac{I_\mathrm{r}}{I_\mathrm{i}} = \left(\frac{E_\mathrm{r}}{E_\mathrm{i}}\right)^2 = r^2. \tag{2.11}$$

Transmittance T shows an additional dependence on the refractive indices, so

$$T = \left(\frac{n_\mathrm{t} \cos\Theta_\mathrm{t}}{n_\mathrm{i} \cos\Theta_\mathrm{i}}\right) t^2. \tag{2.12}$$

2.2 Fabry-Pérot Resonators

A Fabry-Pérot resonator (FPR) comprises two plane-parallel mirrors, facing each other with reflectivities of R_1 and R_2. The optical distance $L = nL_0$ between these mirrors defines the wavelengths, which are capable of creating a steady-state within the resonator, called modes. Now n is the refractive index and L_0 is the geometric distance between the mirrors. The standing wave is projected on itself after one round trip, reproducing phase, and amplitude. Only if L is an integer multiple of half the wavelength, such a condition is fulfilled. (In this assumption both mirrors are made out of metal, so standing wave nodes occur at the metal interface.)

$$L = nL_0 = \frac{m\lambda}{2}, \tag{2.13}$$

where m is an integer, called the axial (or longitudinal) mode order, representing the number of intensity maxima within the resonator. When light with wavelength λ enters an FPR with R_1,$R_2 < 1$, a portion of the intensity reflects at the first mirror. The transmitted light is reflected back and forth within the resonator. At each round trip, a part of the intensity is transmitted through both mirrors and leaves the resonator. The total reflectivity R and transmittance T can be described as follows:

$$R = \frac{\left(\sqrt{R_1} - \sqrt{R_2}V\right) + 4\sqrt{R_1 R_2}V \sin^2\left(2\pi\frac{L}{\lambda}\right)}{\left(1 - \sqrt{R_1 R_2}V\right) + 4\sqrt{R_1 R_2}V \sin^2\left(2\pi\frac{L}{\lambda}\right)} \tag{2.14}$$

$$T = \frac{(1-R_1)(1-R_2)V}{\left(1 - \sqrt{R_1 R_2}V\right) + 4\sqrt{R_1 R_2}V \sin^2\left(2\pi\frac{L}{\lambda}\right)}, \tag{2.15}$$

where V is the loss factor per transit [30]. The cavity length has to fulfil the resonance condition $L = \lambda/2$ to get rid of the periodic part in the denominator to maximize T. For an ideal resonator without losses ($V = 1$) one obtains $T_{max} = 1$ for $R_1 = R_2$. When λ fulfils the condition for a steady-state within a loss-free resonator (eq. (2.13)), the entire light travels through the resonator. This even holds for high reflectivities above 99.5 %. Since the condition in eq. (2.13) can be fulfilled simultaneously by several axial modes (wavelengths with different number of intensity maxima within the resonator), the distance between these modes can be written both in frequency and wavelength ranges

$$\Delta\nu = \frac{c_0}{2L} \qquad \Delta\lambda_{m,m+1} = \frac{lambda_m^2}{2L} = FSR \tag{2.16}$$

In this work the wavelength definition will be used, describing the free spectral range (FSR).

To shift the resonant wavelength by Δ_lambda a displacement of ΔL is required.

$$\Delta L = m\frac{\Delta\lambda}{2} \tag{2.17}$$

Equation (2.17) is still dependent on m, as the cavity length shifts for each contained half-wavelength. This linear behavior is valid with the assumption that a node of the contained electric field is at the mirror surface, for example, when using metal mirrors. In the case of broadband dielectric DBR (this work), an adjustment needs to be considered, described in section 3.4.

The linewidth $\delta\lambda$ of the transmitted spectrum is defined as

$$\delta\lambda = \left|\ln\left(\sqrt{R_1R_2}V\right)\right| \frac{\lambda^2}{2\pi L}. \tag{2.18}$$

Equation 2.18 shows that the bandwidth is narrow for high reflectivities ($R_i \to 1$) and low losses ($V \to 1$). In figure 2.1, visualizations of equation 2.15 are shown. In the left graph, a distance $L = 5\,\mu m$ without cavity losses and mirrors with reflectivities $R_1 = R_2 = R$ is assumed, while the incident wavelength is varied. At certain wavelengths, which fulfill condition 2.13, T reaches a value of 1. At these wavelengths this resonator is transparent. The reflectivities (0.1, 0.5 and 0.9) do not have an influence on maximum transmittance but the linewidth of the transmission peak. Higher reflectivities create narrower transmission peaks. In the right graph, the incident wavelength ($\lambda = 1550\,nm$) is fixed while the mirror distance L is varied. Here a similar behavior can be observed. Transmittance is maximum when a steady-state condition is met. Note that

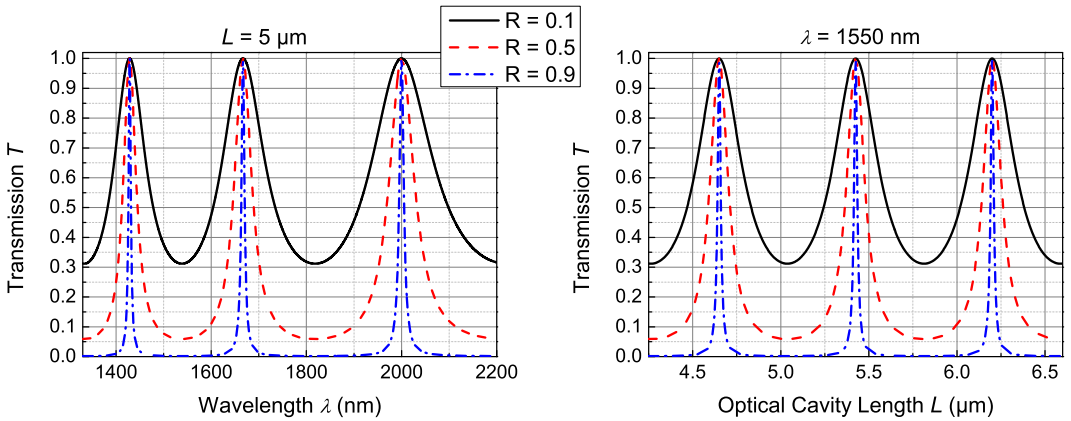

Figure 2.1: Fabry-Pérot resonator with two mirrors of identical reflectivities $R_1 = R_2 = R$. The results are presented for three different R. **Left:** Transmittance T for a fixed loss-less resonator cavity length of $L = 5\,\mu\text{m}$ for variable incident wavelength λ. **Right:** Transmittance T for a loss-less resonator for a fixed incident wavelength of $\lambda = 1550\,\text{nm}$ depending on variable optical cavity length L.

while the peaks are equidistant when L is varied, they are not for different λ at a fixed L. In fig. 2.2, a loss dependent maximum transmittance is plotted. Higher losses (lower V) within the cavity reduce maximum transmittance, while R defines how fast T drops.

The effect of $T \to 1$ can be explained by constructive interference within the cavity when they are $m\lambda/2$ apart. This results in the intensity leaving the resonator at mirror 2 equals the intensity entering mirror 1. Within the resonator, the intensity is much higher than the incident intensity due to multiple internal reflections. For $R = 0.995$ for example the intra-cavity intensity is 200 times larger. Two quantities finesse $\mathcal{F}$ and quality factor Q, are commonly used to characterize an FPR:

$$\mathcal{F} = \frac{FSR}{\delta\lambda} = \frac{\pi}{|\ln(\sqrt{R_1 R_2}V)|} \tag{2.19}$$

$$Q = \frac{\nu}{\delta\nu} \tag{2.20}$$

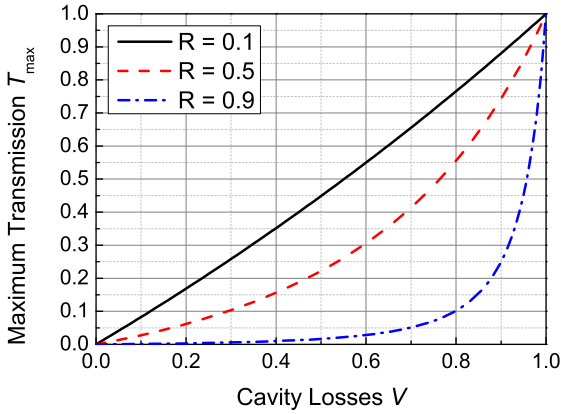

Figure 2.2: A Fabry-Pérot resonator consists of two mirrors of identical reflectivities $R_1 = R_2 = R$. The results are presented for three different R. Maximum transmittance $T_{\max}$ of a Fabry-Pérot resonator depending on cavity losses V.

Conditions for a Stable Resonator and its Modes

A resonator is stable when an introduced light beam parallel to the resonator axis stays within the resonator after an infinity number of reflections, assuming reflectivities of 1 for both mirrors. A g-factor defines the stability mathematically

$$g_{\mathrm{i}} = 1 - \frac{L}{\rho_{\mathrm{i}}}, \tag{2.21}$$

where L is the optical resonator length and ρ_{i} is the radius of curvature for mirror 1 and 2, respectively. Note that a concave mirror has a positive ρ, while a convex mirror has a negative ρ. The condition for a stable resonator is

$$0 < g_1 g_2 < 1. \tag{2.22}$$

Having considered a Fabry-Pérot resonator, made from two plane-parallel mirrors in the previous section, now stability issues arising from that setup are investigated. A plane mirror has a ρ_{plane} of infinity, so $g_{\mathrm{plane}} = 1$ and the condition in eq. (2.22) is not met, because $g_{\mathrm{plane}} g_{\mathrm{plane}} = 1$. Conclusively when trying to build a stable Fabry-Pérot filter, at least one mirror needs to be bent concavely to fulfil the upper condition of eq. (2.22). Assuming a plane concave resonator (one mirror is plane and the other is concavely bent), the lower condition can be fulfilled by

$$\frac{L}{\rho} < 1 \quad \Rightarrow \quad L < \rho. \tag{2.23}$$

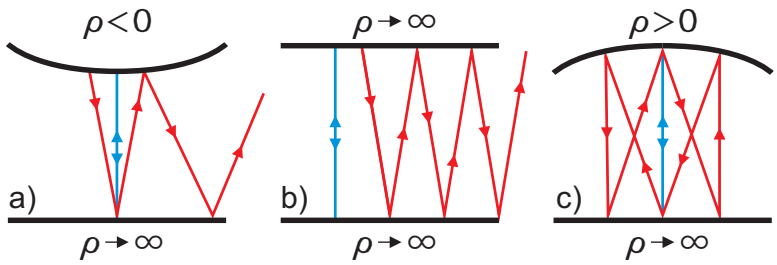

Figure 2.3: Angled reflection in three resonators, **a)** unstable because $g_1 g_2 < 0$, **b)** unstable because $g_1 g_2 = 1$ and **c)** stable because $0 < g_1 g_2 < 1$.

To visualize why only a concave resonator can be stable, fig. 2.3 presents three resonators. In each, an angled reflection results in a lateral displacement. All bottom mirrors are plane, giving $g_1 = 1$. In a) the top mirror is convex; the reflected beam quickly leaves the resonator and energy is lost. In b) both mirrors are flat; the beam also leaves the resonator after enough reflections, especially if the mirrors are not perfectly parallel. In c) a concave top mirror creates a stable resonator. Hereafter a certain number of reflections, the reflected beam reproduces its previous path, never leaving the resonator. The resonators investigated in this work are all stable, because of case c) with $L << \rho$ for the concave mirror.

As mentioned earlier, the electric field distribution E_1 on one mirror needs to reproduce itself after one round trip. The following condition in polar coordination system must be fulfilled:

$$E_1(r,\Phi) = \gamma E_2(r,\Phi), \tag{2.24}$$

where γ is the complex eigenvalue, describing the losses after one round trip. Within the resonator, there is an unlimited number of eigensolutions - eigenmodes - for a steady-state electric field E. In the case of circular symmetry, these modes are called Gauss-Laguerre Modes [20].

$$E_{pl}(r,\Phi) = E_0 \left(\frac{\sqrt{2}r}{w_i}\right)^l L_{pl}\left(\frac{2r^2}{w_i^2}\right) \exp\left(\frac{-r^2}{w_i^2}\right) \cos(l\Phi) \tag{2.25}$$

$$\gamma = \exp\left[\mathrm{i}\frac{2\pi}{\lambda}\left(2L - \frac{\lambda}{\pi}(2p + l + 1)\arccos\sqrt{g_1 g_2}\right)\right], \tag{2.26}$$

where p and l are indices which represent the number of radial and azimuthal nodes, respectively. These transversal modes are called transversal electrical

modes (TEM_{pl}). The beam radius w_i determines the lateral size of the fundamental mode TEM_{00} mode on mirror i

$$w_i = \sqrt{\frac{\lambda L}{\pi}\sqrt{\frac{g_j}{g_i(1-g_1g_2)}}}, \tag{2.27}$$

where i,$j = 1$,2 and $i \neq j$ [30]. Higher order modes have a radius $w_{i,pl}$ of

$$w_{i,pl} = w_i\sqrt{2p+l+1}. \tag{2.28}$$

Because the radii of high order transversal modes are different, so is the distance travelled within one round trip. This results in a shift of the resonant wavelength, thus

$$\lambda_{m,pl} = \frac{2L}{m + \frac{2p+l}{\pi}\arccos\sqrt{g_1g_2}}. \tag{2.29}$$

When inserting values for TEM_{00} ($p = l = 0$), eq. (2.13) for steady-state condition is obtained. Note that higher-order transversal modes always have a shorter wavelength than the fundamental mode.

2.3 Optical Thin-Films

In the last section, it was shown that high reflectivity mirrors are desirable for a narrow optical filter (eq. (2.18)). Furthermore, the distance between two mirrors of an FPR has to fulfil $L = m\lambda/2$ for highest transmission (compare with eq. (2.13)).

This section explains the behavior of optical thin-films when illuminated with a single wavelength. A thin-film is a layer with a thickness in the range of the wavelength under investigation. In the present case, optical thin-films are of interest and have a thickness from several nm to few micrometers. Applying a thin-film on a substrate changes its reflectivity depending on refractive indices of substrate n_3, of incidence medium n_1, and of thin-film itself n_2. Furthermore the thin-film has an optical thickness of $d_2 = n_2 \cdot d_{\mathrm{tf}}$, while d_{tf} being the physical thickness. In fig. 2.4 reflectivity of such a layer stack is presented depending on the optical thickness of the thin-film.

At an optical thickness of zero, no thin-film is present. This position represents the reflectivity of the substrate itself. From this value, it is possible to increase

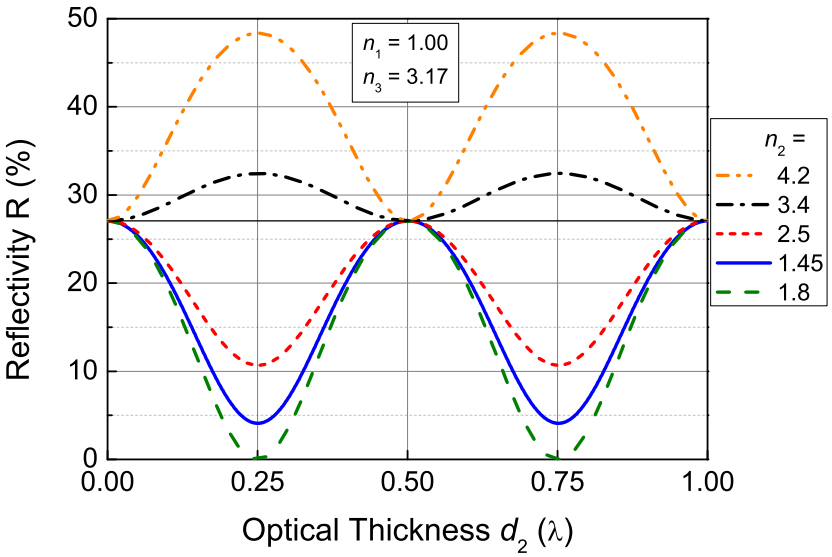

Figure 2.4: Reflectivity of a thin-film with refractive index n_2 between air ($n_1 = 1$) and InP ($n_3 = 3.17$) depending on its optical thickness d_2. Thin layer materials are Ge ($n_2 = 4.2$), Si ($n_2 = 3.4$), SiC_z ($n_2 = 2.5$), SiN_y ($n_2 = 1.8$) and SiO_x ($n_2 = 1.45$).

or decrease the reflectivity by applying a thin-film on the substrate surface. In orange and black, cases for $n_2 > n_1$,n_3 are presented. Refractive index is higher than either medium, and the reflectivity rises till a maximum at $\lambda/4$. It returns to the original value for $\lambda/2$. The behavior reappears for $3\lambda/4$ and λ. In red, blue and olive, cases for $n_1 < n_2 < n_3$ are presented. Reflectivity drops by applying a thin-film with a refractive index between the values of the other two media. At a certain ratio (olive, eq. (2.36)), the reflectivity can even reach zero at $\lambda/4$ and $3\lambda/4$ optical thickness. In the following section, the case for $\lambda/4$ will be investigated in more detail, either reducing or increasing reflectivity.

Anti-Reflective Coating

An anti-reflective coating (ARC) with refractive index n_{ARC} and thickness $\lambda_0/4n_{ARC}$ is a quarter-wave plate on a substrate to reduce reflectivity for wavelength λ_0 of an air-substrate interface, see fig. 2.4. It is essential to respect $n_1 < n_{ARC} < n_3$, where n_1 is the refractive index of the surrounding medium

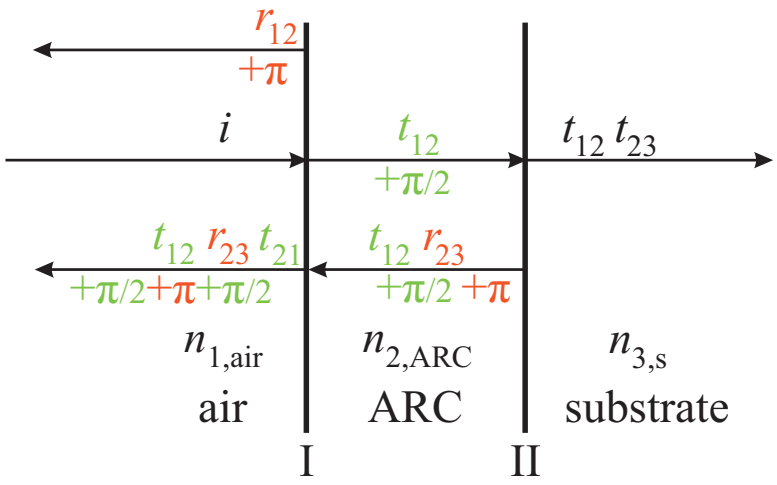

Figure 2.5: Schematic principle with interfaces I and II of an ARC with thickness $\lambda_0/4n_2$ to reduce reflection at an air-silicon interface for wavelength λ_0. Phase shift of $+\pi$ for reflections because $n_\mathrm{t} > n_\mathrm{i}$ marked red and additional phase shifts of $+\pi/2$ marked green for traveling through ARC layer with $\lambda/4$ thickness. The two reflected beams r_{12} and $t_{12}r_{23}t_{21}$ have a total phase difference of π, thus interfering destructively.

and n_3 describes the substrate. It is a resonator with mirror reflectivities well below 1, defined by air-ARC and ARC-substrate interfaces, which are depending on their refractive index differences (compare with eq. (2.9)). When looking at the propagation of light through an ARC, it is important to consider whether a phase shift is occurring at each interface. Remembering eq. (2.9), the reflection coefficient changes its sign for $n_\mathrm{t} > n_\mathrm{i}$ at perpendicular incidence. A sign change is equivalent to a phase shift of π. In fig. 2.5, interfaces of air-ARC and ARC-substrate are shown. An incident light beam (i) with wavelength λ_0 hits interface 1-2 (I) perpendicularly. The reflected light r_{12} has a phase shift of $+\pi$ due to $n_\mathrm{air} < n_\mathrm{ARC}$. The transmitted light t_{12} is travelling through the ARC, creating a phase shift of $+\pi/2$ because of the ARC thickness being $\lambda_0/4n_\mathrm{ARC}$. Reflection at the second interface 2-3 (II) creates another phase shift of $+\pi$ for $t_{12}r_{23}$ as $n_\mathrm{ARC} < n_\mathrm{s}$. Travelling through the ARC a second time, now in the opposite direction, adds a final phase shift of $+\pi/2$. In total, there are two beams at interface 1-2 (I) travelling left, where r_{12} shows a phase shift of $+\pi$ and $t_{12}r_{23}t_{21}$ shows $+2\pi$, which reduces reflection at wavelength λ_0 by destructive interference. Mostly it is not cancelled out entirely, as the reflection amplitudes depend on the interface reflectivities. Only for condition in eq. (2.36), amplitudes match and reflectivity goes to zero (olive case in fig. 2.4). An example for

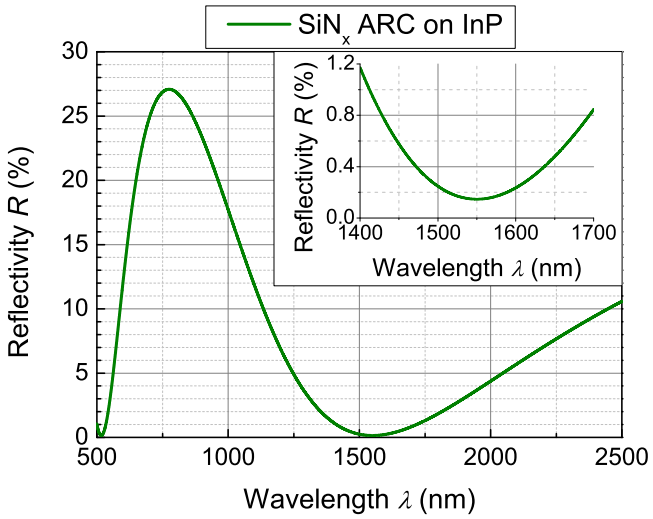

Figure 2.6: Reflectivity reduction of InP by applying SiN_y ARC ($n_{SiN_y} = 1.85$) for $\lambda_0 = 1550\,\text{nm}$. The inset shows that the reflectivity does not reach zero but is below 1 % for a range of 300 nm.

a SiN_y ARC on indium phosphide (InP) is shown in fig. 2.6. Lowest reflection occurs at $\lambda_0 = 1550\,\text{nm}$ (inset shows an enlarged view around the minimum). It does not reach zero, because n_{SiN_y} does not match perfectly. Anyway, reflectivity is below 1 % for a range of 300 nm around λ_0. At $\lambda_0/4 = 775\,\text{nm}$, InP reflectivity in air can be seen ($\approx 27\,\%$).

When looking at the electric fields E_I and E_II at the interfaces I and II, respectively, it is clear that

$$E_\text{I} = E_{i12} + E_{r12} = E_{t12} + E_{t12r23t21} \text{ and} \tag{2.30}$$
$$E_\text{II} = E_{i23} + E_{t12r23} = E_{t12t23}. \tag{2.31}$$

Accordingly, magnetic fields H_I and H_II can be described with

$$H_\text{I} = \sqrt{\frac{\varepsilon_0}{\mu_0}}(E_{i12} - E_{r12})n_1 = \sqrt{\frac{\varepsilon_0}{\mu_0}}(E_{t12} - E_{t12r23t21})n_2 \text{ and} \tag{2.32}$$
$$H_\text{II} = \sqrt{\frac{\varepsilon_0}{\mu_0}}(E_{i23} - E_{t12r23})n_1 = \sqrt{\frac{\varepsilon_0}{\mu_0}}E_{t12t23}n_2. \tag{2.33}$$

When including all refractive indices and phase shifts due to travelling through the layers, it is possible to define a characteristic matrix M_I, which connects the

electric fields on neighboring interfaces I and II.

$$\begin{pmatrix} R_{\mathrm{I}} \\ H_{\mathrm{I}} \end{pmatrix} = M_{\mathrm{I}} \begin{pmatrix} E_{\mathrm{II}} \\ H_{\mathrm{II}} \end{pmatrix} \tag{2.34}$$

Solving eq. (2.34), it is possible to calculate reflectivity R_{ARC} of an ARC at its designed wavelength with refractive index n_{ARC} on top of a substrate (n_{s}) within a surrounding medium (n_1) [29]

$$R_{\mathrm{ARC}} = \frac{(n_1 n_{\mathrm{s}} - n_{\mathrm{ARC}}^2)^2}{(n_1 n_{\mathrm{s}} + n_{\mathrm{ARC}}^2)^2}. \tag{2.35}$$

When the refractive index is matched to surrounding medium and substrate, it is possible to suppress R_{ARC} entirely for one wavelength. This is the case for

$$n_{\mathrm{ARC}} = \sqrt{n_1 n_{\mathrm{s}}}. \tag{2.36}$$

Distributed Bragg Reflector

To create a high reflectivity for light with wavelength λ_0, the phase shift at interface II (fig. 2.5) has to vanish. Then both reflected waves r_{12} and $t_{12}r_{23}t_{21}$ are in phase, and the reflectivity for λ_0 maximizes. This can be achieved by fulfilling $n_2 < n_1$,n_0. The same stands for $n_2 > n_1$,n_0. To harvest both cases simultaneously, a layer stack of $\lambda_0/4$ thin-films with alternating high n_{H} and low refractive index n_{L} can be built, called a distributed feedback reflector (DBR). Figure 2.7 visualizes this case, looking at the phase at interface I for the different paths. The first is the reflection at interface I, which creates a phase shift of π. The second path is transmission at interface I, and reflection at interface II. Here a shift of π occurs due to traversing layer 1 twice and no shift because $n_{\mathrm{L}} < n_{\mathrm{H}}$. The third path describes light transmitting at interface I and II and reflecting at interface III. Here travelling through layer 1 and 2 twice creates a shift of 2π, which is irrelevant due to periodicity. The reflection at interface III adds a phase shift of π. Thus interface III behaves the same way as interface I, and so on. Conclusively, all paths show a phase shift of π travelling left at interface I. An increasing number of layer pairs (HL) is, in conclusion, enhancing the reflectivity of a DBR stack because more waves interfere constructively.

A layer stack of two layers on a substrate with the high refractive index material facing ambient air is termed gHLa, meaning glass-high refractive index-low refractive index-air. When stacking M pairs, it is called

$$\mathrm{g(HL)}^M\mathrm{a}, \tag{2.37}$$

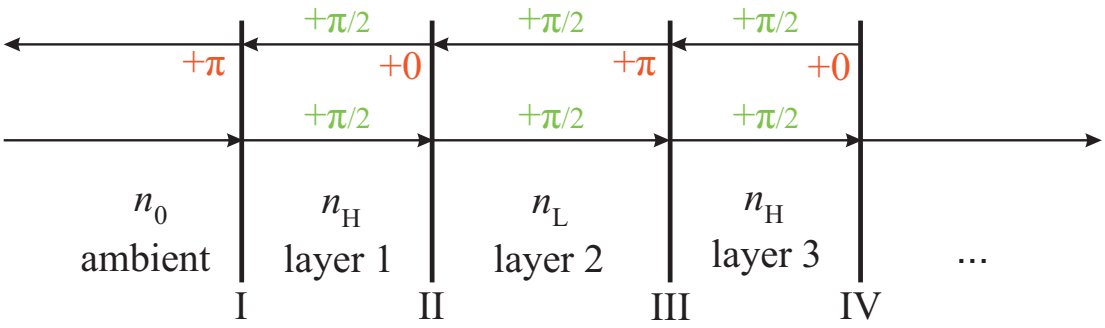

Figure 2.7: Schematic principle of a DBR - an alternating layer stack of high (n_H) and low (n_L) refractive index material with thicknesses $\lambda_0/4n_i$.

where M describes the number of layer pairs. The transfer matrix theory describes each interface with a 2x2 matrix T, containing r and t and phase change due to propagation. A layer stack can then be described by multiplying all interfaces, and a matrix $\mathcal{M}$ can be calculated, connecting incident and transmitted electric fields

$$E_t = \mathcal{M} E_i. \tag{2.38}$$

The resulting maximum reflectivity of a DBR is given by

$$R_{\text{max,DBR}} = \left(\frac{1 - \frac{n_{\text{out}}}{n_{\text{in}}} \left(\frac{n_H}{n_L} \right)^{2M}}{1 + \frac{n_{\text{out}}}{n_{\text{in}}} \left(\frac{n_H}{n_L} \right)^{2M}} \right)^2, \tag{2.39}$$

where M gives the number of layer pairs in the DBR. The reflectivity is increased with higher numbers of M because there are more internal reflections. More waves can interfere with each other. The second important influence in eq. (2.39) are refractive indices of DBR layers, n_H and n_L. Especially difference Δn between high and low refractive index is important. For large values, eq. (2.39) approaches 1 asymptotically. This can be explained with the reflection at a single interface. A higher refractive index step increases reflection amplitude. Thus having a DBR with large Δn, fewer layer pairs M are required to reach high interference amplitude in reflection. Moreover, a large Δn increases DBR stopband, meaning reflectivity is not only high at the designed center wavelength λ_c but also within a certain range around it. Consequently, DBR stopband $\Delta\lambda_c$ is larger for larger Δn according to eq. (2.40), describing the width at which reflectivity drops to 95 %.

$$\Delta\lambda_c = \frac{4\lambda_c}{\pi} \arcsin\left(\frac{n_H - n_L}{n_H + n_L} \right) \tag{2.40}$$

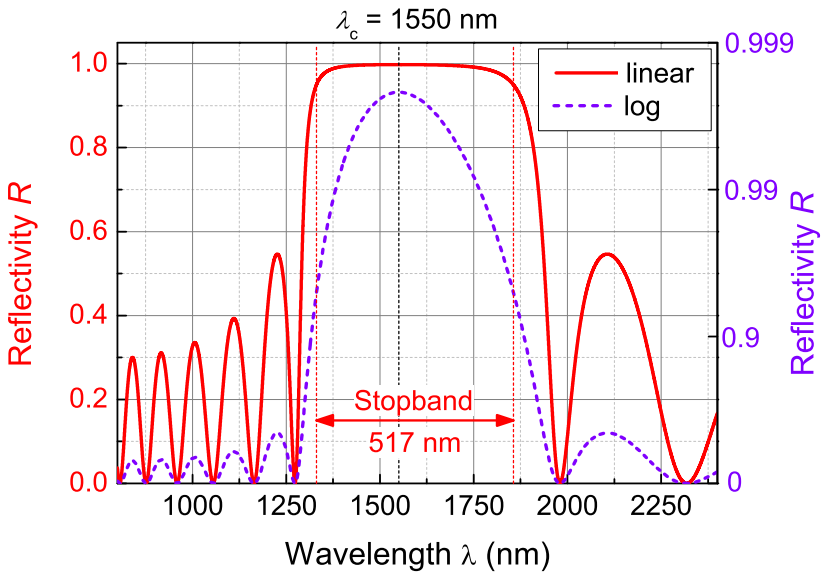

Figure 2.8: Linear (green) and log scale (purple) DBR reflectivity with 6 layer pairs and $\Delta n = 1$ for a center wavelength $\lambda_c = 1550\,\text{nm}$.

In fig. 2.8, the reflectivity stopband of a DBR with $M = 6$ and $\Delta n = 1$ between air and Si is shown. In green, a wide reflectivity plateau is visible. Choosing a logarithmic scale, it can be seen that reflectivity for the designed center wavelength $\lambda_c = 1550\,\text{nm}$ is highest. According to eq. (2.40), $\Delta\lambda_c 517\,\text{nm}$.

2.4 Tunable Optical Filter

Combining two ingredients introduced in sections 2.2 and 2.3 creates an optical FPR with highly reflective mirrors. Two DBRs (with R_{max} beyond 99.5 %) at a distance L_{air}, create an air-filled cavity (air-gap). Changing the optical length $L = n_{air} L_{air}$ of the cavity results in a tuning of the transmission wavelength. So, either the refractive index or the geometrical length L_{air} have to be adjustable. Changing the refractive index through an electro-optic effect (Kerr or Pockels) is possible but limited to a small range [73]. Thus the distance between both mirrors needs to be changed. One of these mirrors needs to be fixed on a substrate and the other needs to be movable, to adjust L_{air}, which then shifts the steady-state condition according to eq. (2.13). At these wavelength regions,

the resonator is transparent, creating a small band-pass filter as all other wavelengths have near-zero T (compare fig. 2.1 left for high R). The top mirror can be actuated in two ways - electro-thermally and electro-statically. Both methods are presented here. Although the effect is the same - displacement of the top mirror - the methods are entirely different. With an appropriate design of electrodes, it is even possible to combine both methods in one device.

Electro-Thermal Displacement

Joule heating of the top mirror results in an electro-thermal displacement ΔL_{et}. Two electric connections are present on opposing sides of the MEMS. When a current I_{MEMS} flows through the electrode, the ohmic resistance generates heat. It is then transferred to the MEMS itself, causing it to expand. Due to initial stress within the layers which already bent the MEMS, the only direction is upwards, away from the bottom mirror. Ultimately the air-gap between the two mirrors extends, moving the resonant wavelength towards larger values - a red-shift occurs. This process is continuous. As heating power P_{heat} is proportional to I^2_{MEMS} and to ΔL_{et}, a proportionality between displacement and heating current can be formulated.

$$\Delta L_{\text{et}} \propto P_{\text{heat}} = I^2_{\text{MEMS}} \cdot R_{\text{MEMS}}, \tag{2.41}$$

where R_{MEMS} is the resistance of the top electrode. When increasing I_{MEMS} further, at some point the next longitudinal mode enters the DBR stopband and appears at lower wavelengths. The distance between both modes is the FSR which describes the ultimate tuning limit determined by the resonator length. With increasing air-gap, FSR narrows consequently. Each higher mode has a lower FSR in the wavelength regime and thus a lower tuning range. The initial position of the MEMS depends on processing, especially on the initial air-gap. Because tuning with I_{MEMS} is only possible one way, the initial cavity length is adjusted by substrate temperature T_{S}. Lower T_{S} contracts the MEMS-DBR more than the substrate, effectively reducing the air-gap. Now it is possible to fine-tune the initial position of the MEMS-DBR and move the resonant wavelength towards the lower edge of the DBR stopband. Due to the volume differences between substrate and MEMS-DBR, it is obvious that heating of the substrate is much slower, so it is used as an offset, whereas I_{MEMS} tunes to the desired wavelength or can be even modulated with higher frequencies.

Electro-Static Displacement

The second method is an electro-static displacement. Here, a second electrode is necessary, which is electrically isolated from the first on top of the MEMS-DBR. It lies below the movable mirror on top of the fixed bottom mirror. A voltage U_{MEMS} between both electrodes causes an attracting force F_{es}, opposing the mechanical restoring force F_{mec} of the MEMS.

$$F_{\mathrm{es}} + F_{\mathrm{mec}} = 0 \tag{2.42}$$

$$-\frac{\varepsilon_0 A_{\mathrm{MEMS}}}{2}\left(\frac{U_{\mathrm{MEMS}}}{L_{0,\mathrm{es}} + \Delta L_{\mathrm{es}}}\right)^2 - k_{\mathrm{m}}\Delta L_{\mathrm{es}} = 0 \tag{2.43}$$

where ε_0 is the vacuum permittivity, A_{MEMS} is the MEMS electrode area, $L_{0,\mathrm{es}} = L_{\mathrm{air}} + d_{\mathrm{DBR}}$ is the distance between both electrodes composed of air-gap and DBR thickness, ΔL_{es} is the displacement from relaxed initial bending, and k_{m} is the MEMS spring constant. The DBR thickness itself needs to consider both thickness and permittivity of each layer. Rearranging eq. (2.43) for small displacements $\Delta L_{\mathrm{es}} << L_{0,\mathrm{es}}$, thus $L_{0,\mathrm{es}}^2\Delta L_{\mathrm{es}} + 2L_{0,\mathrm{es}}\Delta L_{\mathrm{es}}^2 + \Delta L^3 \approx L_{0,\mathrm{es}}^2\Delta L_{\mathrm{es}}$ gives a wavelength shift with eq. (2.17) of

$$\Delta\lambda = \frac{2\Delta L_{\mathrm{es}}}{m} \approx -\frac{\varepsilon_0 A_{\mathrm{MEMS}}}{m k_{\mathrm{m}}}\left(\frac{U}{L_{0,\mathrm{es}}}\right)^2 \tag{2.44}$$

It is independent which electrode is charged with or stripped from electrons. Both ways create an attracting force. Thus proportionality for electro-static actuation is

$$\Delta L_{\mathrm{es}} \propto -U_{\mathrm{MEMS}}^2. \tag{2.45}$$

With both methods, thermal stabilization is necessary as environmental temperature changes can massively change the MEMS-DBR position [57]. In comparison to electro-thermal tuning, electro-static tuning can be used for much larger modulation frequencies as no thermal effects are necessary to change the MEMS-DBR position. The limiting factor for electro-static actuation is the eigenfrequency of the MEMS mirror itself. It can be 3 orders of magnitude above maximum modulation frequency achievable with electro-thermal tuning.

2.5 Technology for MEMS-DBR Processing

This section outlines the essential surface-micro-machining processing steps to build a SiO_x-SiC_z MEMS-DBR. These include the deposition, structuring, and characterization of dielectric and metal layers.

Deposition of Dielectrics

Dielectrics deposited for this work, are silicon oxide (SiO_x), silicon nitride (SiN_y) and silicon carbide (SiC_z). All of them are grown with an inductively-coupled plasma-enhanced chemical vapor deposition (ICP-PECVD) at low temperatures of 80 °C. It is necessary for process compatibility reasons with the half-VCSEL substrates, which cannot sustain temperatures above 150 °C. In a PECVD, gaseous precursors containing the required elements blend inside a vacuum chamber where an electric field excites them. The PECVD reactor used here contains two separate RF generators both operating at 13.56 MHz. The first creates an RF-field between two electrodes located below and above the sample. Since the frequency is high, only lightweight electrons can follow the field. Ions are too heavy and are not excited. Electrons acquire energy from the electric field and collide with gas molecules, causing excitation and ionization [38]. Thus, stripping electrons from the molecules generates radicals. Higher RF-powers (P_{RF}) increase the plasma energy, eventually affecting the deposition rate. The second field (ICP) is introduced into the chamber through a coil above the sample. It has a focusing effect on the plasma, affecting its density. Since the frequency is in the MHz range as well, again only the electrons are affected. The resulting layer is growing on all surfaces in touch with the plasma. This is particularly relevant as it is not a directed deposition, and thus the step coverage is very good [3]. Step coverage is essential in this work because dielectric layers are grown on structured samples containing steps from previous processing. Table 2.1 lists the precursor gases needed for the three dielectrics. Further information on the chemical reactions can be found in appendix A.

The resulting layers show an amorphous structure, mainly due to the low deposition temperature. In contrast to more crystalline layers, formed in PECVD chambers heated above 400 °C, here a rather porous material is grown. It causes stacking faults, pinholes or interstitial atoms, which result in layers under stress. For SiN_y, both compressive and tensile values are possible within a specific range while SiO_x and SiC_z only grow with compressive layer stress. These

Table 2.1: Gases necessary (x) for growth of dielectrics in a low-temperature PECVD chamber.

layer	Ar	CH_4	He	SiH_4	N_2	N_2O
SiO_x			x	x		x
SiN_y			x	x	x	
SiC_z	x	x	x	x		

stresses vary to a small degree through adjustment of the processing parameters like gas flow ratios, plasma power, and chamber pressure. Particularly by changing the precursor gas ratio, a shift in Si percentage can be observed by a shift in the refractive index - more Si increases the refractive index. As a result of growing amorphous non-crystalline layers, there cannot be a specific stoichiometric description of the material. Hence, variables x, y and z accompany the names (SiO_x, SiN_y and SiC_z). Moreover, each layer additionally contains hydrogen atoms trapped in bulk. Further investigations on layer compositions are not performed in this work.

Structuring Dielectrics

Silicon-based dielectrics can be dry-etched in a reactive ion etching (RIE) chamber with radicals containing fluoride. The following gases are available: sulfur hexafluoride (SF_6), tetrafluoromethane (CF_4) and fluoroform (CHF_3). Moreover, oxygen (O_2) and argon (Ar) assist in the removal of created waste products. The processing chamber is built similarly to a PECVD reactor with a 13.56 MHz RF signal between two electrodes. At a pressure around 100 mTorr[1] (0.13 mbar) radicals within the plasma drift towards the sample surface due to a DC bias. At the surface, the radicals react with the dielectrics, effectively removing material isotropically. As there is no reaction at a metal surface, either a Cr or Ni etch mask can be used for structuring. The reactions are summarized in appendix A. The etching speed and selectivity are influenced by processing parameters such as plasma power and ratios of gas mixtures.

[1] PECVD manufacturer Oxford employs pressure unit 1 mTorr $= 1.3 \cdot 10^{-3}$ mbar, which is used accordingly throughout this thesis to represent the recipes.

Optical Characterizations of Thin-Film Dielectric Layers

Ellipsometry is a tool used to characterize thin-films optically, here dielectrics. An ellipsometry measurement characterizes a single layer deposited on a silicon substrate. Hereby, a defined linear polarization (45° towards the incident plane, thus 50 % TE and 50 % TM) hits the sample surface at a certain angle (70°). With an analyzer, compensator, and detector, the reflected polarization state is characterized. This way, the polarization state of the reflected light translates to an intensity signal which can be detected. Since DBRs for a wavelength range around 1550 nm are deposited, measurement range covers the near-infrared region (NIR, 800 nm to 1700 nm). Depending on the layer thickness and optical properties, the reflected light differs from the incident light. The resulting values Δ and Ψ describe the phase change and ratio of amplitudes, respectively. Together they describe the shape of the reflected light with elliptic polarization. Next, a model describes the layer stack (here, a silicon substrate, a dielectric thin-film and ambient air) with appropriate starting values for expected layer thickness $d_{\text{dielectric}}$ and refractive index n_0. The properties for the substrate were either measured before the deposition or taken from a database.

The Cauchy model summarizes the resulting wavelength-dependent optical properties (refractive index n and extinction coefficient k) of the dielectric layer. It works for transparent materials such as SiO_x or SiN_y.

$$n(\lambda) = n_0 + \frac{n_1 \cdot 10^4}{\lambda^2} + \frac{n_2 \cdot 10^9}{\lambda^4} \tag{2.46}$$

$$k(\lambda) = k_0 \cdot 10^{-5} + \frac{k_1 \cdot 10^4}{\lambda^2} + \frac{k_2 \cdot 10^9}{\lambda^4} \tag{2.47}$$

Absorbing materials or regions of a material need a different approach. The Tauc-Lorentz oscillator theory portrays a complex dispersion with dielectric functions ε_1 and ε_2.

$$\varepsilon_2(E) = \frac{A(E - E_g)^2}{(E^2 - E_0^2)^2 + C^2} \cdot \frac{\Theta(E - E_g)}{E} \tag{2.48}$$

$$\varepsilon_1(E) = \varepsilon_1(\infty) + \frac{2}{\pi} P \int_{E_g}^{\infty} \frac{E' \varepsilon_2(E')}{E'^2 - E^2} \mathrm{d}E', \tag{2.49}$$

where E_g is the optical bandgap, A the oscillator strength, C the damping, E_0 the electrical bandgap and normally $\varepsilon_1(\infty) = 1$. P is the Cauchy principal value for the layer, because of a singularity at E_0 [34]. An amorphous material can thus be treated like a crystalline bulk material having unlimited repetitions of a

unit cell, combined with a disturbance [31]. As an example, fig. 3.1 shows n and k traces of a 210 nm SiC_z layer.

Determining Layer Stress of an Optical Thin-Film

A load applied on a solid object with a length l, generates an axial strain. Consequently, it contracts by δl. Additionally, a deformation in the lateral direction is occurring. This strain ε_t is given by

$$\varepsilon_t = \frac{\delta l}{l}. \tag{2.50}$$

Poisson's ratio μ describes the ratio between lateral ε_l and axial strain ε_a.

$$\mu = -\frac{\varepsilon_t}{\varepsilon_l} \tag{2.51}$$

Internal forces in a layer may appear due to influences of neighboring particles on each other, which is described by layer stress σ. It links to the strain via the Young's Modulus E_{layer}

$$\sigma = E_{layer}\varepsilon_t. \tag{2.52}$$

The layer stress is vital for creating a MEMS-bending and is investigated here for each deposited layer. To determine a thin-film layer stress σ_{tf}, the radius of curvature of a 2-inch Si-substrate before ρ_{pre} and after a deposition ρ_{post} is measured. Due to layer stress in the deposited dielectric layers, the Si-wafer deforms and ρ changes. The thin-film layer stress σ_{tf} is described with Stoney's equation

$$\sigma_{tf} = \frac{1}{6}\left(\frac{1}{\rho_{post} - \frac{1}{\rho_{pre}}}\right)\frac{E_{Si}}{1-\nu_{PR}}\frac{d_s}{d_{tf}}, \tag{2.53}$$

where $E_{Si} = 180.5\,GPa$ is the Young's Modulus and $\nu_{PR} = 0.28$ is Poisson's ratio for a crystalline silicon wafer in (100) orientation. d_s and d_{tf} are substrate and thin-film thicknesses, respectively.

Photolithography

A key technique for creating a MEMS-structure is photolithography. It is required to shape each material. For a free-standing MEMS structure, an under-etching of the MEMS-DBR is inevitable. Removing specific areas of the DBR exposes the underlying sacrificial layer. It then can be wet chemically attacked and removed. Furthermore, it is essential to create an aperture in the metal electrodes for light to be able to enter and exit the tunable resonator.

In photolithography, a UV sensitive liquid photoresist (PR) is spin-coated homogeneously on the sample surface. After a pre-bake step at around 100 °C to evaporate the solvent, a semitransparent metal mask is aligned to the sample. UV light exposes sample structures below transparent mask areas. During this time, the photoresist solubility either increases (positive PR, +PR) or diminishes (negative PR, -PR). Areas covered by the metal mask remain unaffected. Lastly, a liquid PR-specific developer removes either exposed (+PR) or unexposed areas (-PR). The developed +PR shows narrowing of the remaining structure towards the PR surface, while developed -PR shows an under-etched shape (narrowing towards the subjacent layer). A third kind, combining properties of +PR and -PR is the image-reversal photoresist (irPR). UV-exposed areas remain in the end (like -PR), but the shape of the photoresist matches a +PR. During processing, an irPR is post-baked after the masked UV exposure and then flood-exposed before development.

For all photoresists, the result is a polymer mask on the sample surface functioning in two ways, etching of subjacent layers or lift-off of subsequent depositions. In the first case, there are areas protected by the developed PR and exposed areas. As an example, a nickel layer below PR is presented. The exposed Ni can be wet-etched (see appendix A) while the protected Ni remains. Finally, acetone and an O_2 plasma remove the PR mask. A structured metal layer remains. For a lift-off process, the desired material is deposited after photolithography. Now a MEMS-electrode composed of a titanium-gold (Ti-Au) layer stack is presented. Evaporated Ti and Au coat surfaces facing the source. Ideally, there is no or insignificant deposition on the PR side walls (fencing). Afterwards, the PR is removed with acetone as well. With the PR, the undesired Ti-Au areas dislodge from the sample surface as well, leaving a structured Ti-Au layer. During the processing of certain material combinations, there are times when either only one case or both can be applied.

Deposition of Metal Layers

Metals are either required as etch masks during dry etching, as they are unaffected, as functional layers such as electrically conductive electrodes, or as a sacrificial layer to release a MEMS-DBR.

Nickel

There are two methods to deposit Ni on a sample, evaporation and sputtering, realized at low pressures around $5 \cdot 10^{-7}$ mbar. An electron beam heats the Ni target during evaporation, causing Ni atoms to leave the target and deposit on the sample surface. Depending on the current, a deposition rate fluctuates around 8 nm/min to 9 nm/min. Deposition via sputtering is done with Ar ions accelerated and focused on a Ni target. This physical bombardment releases Ni atoms from the surface, coating the samples at a rate of 30 nm/min to 40 nm/min. Removing Ni can be done by HNO_3, see appendix A.

Chrome-Gold

MEMS electrodes are made from gold (Au) because it is easy to etch wet-chemically, and it opens the possibility for bonding to larger contact pads. Because of the low adhesion of Au on dielectric layers (MEMS-DBR), a thin chrome-layer (Cr) connects the two. Both are evaporated by heating a boat filled with either Cr or Au. The deposition rates are 2.4 nm/min and 4.2 nm/min, respectively. Structuring is possible via lift-off or wet-chemical etching (seeappendix A).

Titanium-Gold

As an alternative to Cr-Au layer when adhesion is a problem or Cr undesired, Cr can be replaced by Ti. Ti cannot be etched wet-chemically without harming underlying layer. Thus, lift-off is the only option here. Evaporation of Ti is performed with an e-beam heating a Ti target. The evaporated atoms deposit on the sample surface at a rate of 18 nm/min. Subsequently, Au deposits by heating a boat loaded with Au in the same way as for Cr-Au layers.

2.6 Semiconductor Photodetector

Each atom consists of a nucleus and electrons surrounding it. The electrons occupy discrete energy levels. When many atoms create a bulk material, these discrete energy levels become energy bands. Thus, in a bulk material like a

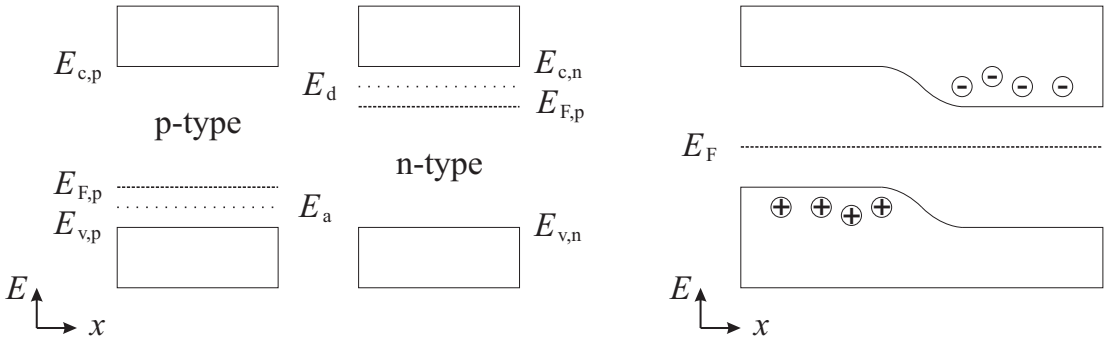

Figure 2.9: Left: Separate band diagrams for p-type and n-type semiconductors with valence-band edge energies $E_{v,p}$ and $E_{v,n}$, conduction-band edge energies $E_{c,p}$ and $E_{c,n}$, Fermi energies $E_{F,p}$ and $E_{F,p}$ and acceptor and donor defect energies E_a and E_d, respectively. **Right:** p- and n-type semiconductor in contact with balanced band diagram. Fermi energy level E_F is now the same in both materials. Equilibrium resulted in free electrons in n-type and free holes in p-type.

crystal, ranges of energy states exist which can be occupied by electrons. These ranges are separated by gaps - the ranges where no electronic states exist. The energetically highest fully occupied band is called the valence band, and the next band at higher energies is called the conduction band, separated by the band-gap. The Fermi energy E_F determines the maximum occupied energy of states at 0 K if they exist. E_F can be in or above a characteristic band-gap when investigating electric conductivity of bulk material. At temperatures above 0 K, some electrons occupy states above E_F while some states below are vacated. The size of the band-gap determines the material-category. For dielectrics, the band-gap is roughly in the range of 5 eV to 10 eV. For semiconductors it is about 0 eV to 5 eV and for metals it is 0 eV. For dielectrics and semiconductors, E_F is inside the band-gap, while for metals it is located in the conduction band. A direct result of this property is a good conductivity for metals even at low temperatures because electrons can move freely inside the conduction band - hence its name. For a semiconductor, an electron first has to be excited above the band-gap to reach the conduction band where it can move to another location.

A semiconductor can be doped with certain other materials which create additional states within the band-gap. Typically, they are either located close to the upper valence-band edge E_v (donor defects, p-type) or close to the lower conduction-band edge E_c (acceptor defects, n-type). It is doping that moves E_F closer to the newly created states. Electrons can be excited across the band-gap

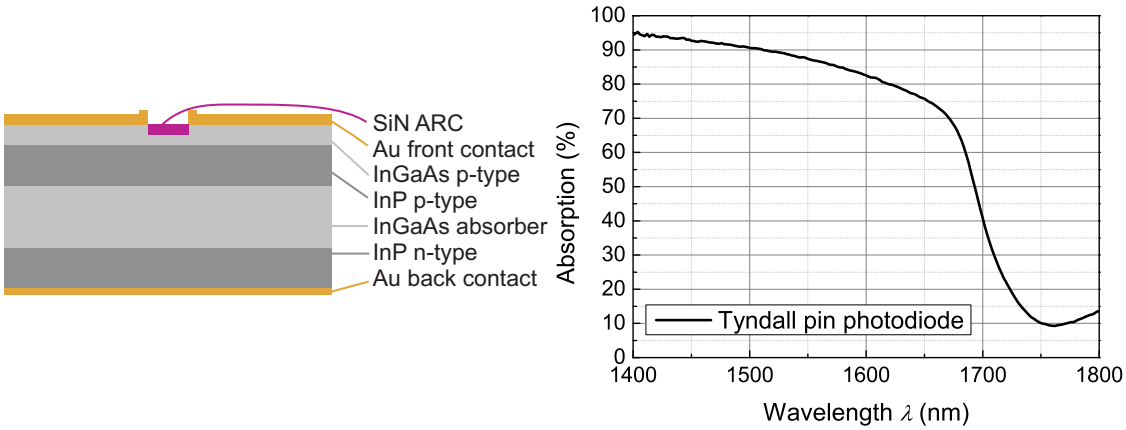

Figure 2.10: Left: Cross-section of a pin-PD with InP p- and n-type layers sandwiching an intrinsic absorption layer InGaAs. On front and back, there are Au contacts. The front shows an SiN_y ARC coating. **Right:** Absorption of a Tyndall pin-PD.

by photon absorption if the photon energy is larger than the band-gap. After a specific relaxation time, the electron will recombine with a hole in the valence band, re-emitting a photon. To utilize the excited electron energy, it has to relocate from the semiconductor into an external circuit. It can be achieved by creating a pn-junction where a p-type and n-type semiconductor meet. Herby E_F will adjust to being on the same level in both materials. It ends in a bending of the band-edges according to fig. 2.9. If an electron is excited within the bending, it separates in space from the hole. The hole moves left in the valence-band while the electron moves right, to reach a lower energy state. A photocurrent I_{ph} arises. Because the thickness of the pn-junction is tiny (in nm range) an intrinsic un-doped layer can be grown between the doped layers (pin-PD). Its Fermi energy is between Fermi energies of separated p- and n-type semiconductors. This leads to a smaller slope of band-gap bending but offers a much thicker layer increasing the absorption probability of an incoming photon. In a photodiode (PD), the photocurrent I_{ph} is given by

$$I_{ph} = \frac{\eta q P_{op}}{\hbar\omega} = R P_{op} \tag{2.54}$$

$$R = \frac{\eta q}{\hbar\omega}, \tag{2.55}$$

where R is the responsivity connecting input optical power P_{op} and generated photocurrent. Moreover $\eta = N_{el}/N_{ph}$ is the quantum efficiency, a ratio between

the number of electrons N_{el} and photons N_{ph}, q is the electron charge and ω the photon frequency.

In this work, the pin-PD was produced at Tyndall[2]. The layer stack can be seen in fig. 2.10 left, where the defining layer is a 2 µm InGaAs intrinsic absorber layer sandwiched between n- and p-type InP layers, respectively. Showing an absorption of more than 50 % for wavelengths below 1690 nm, the PD is perfectly suitable for a widely tunable optical filter to be grown on. The substrate received, already contains a SiN_y ARC ($n_{ARC,PD} = 1.8$) on the surface. In fig. 2.10 right, the absorption spectrum of a pin-PD is presented. The band-gap is located around 1690 nm or 0.73 eV. For higher energies (smaller wavelengths), absorption is increased.

2.7 VCSEL

A vertical-cavity surface-emitting laser (VCSEL) is a semiconductor laser consisting of an FPR with an active region in the cavity. A cross-section of a MEMS-DBR VCSEL is shown in fig. 1.1. Both current flow and photon emission are parallel. With photolithography steps it is possible to manufacture a laterally symmetric cavity, creating a circular beam shape beneficial for coupling into a fiber. In contrast, edge-emitting lasers are always confined to a rectangular aperture and elliptic output beam. Moreover, since current can be confined laterally very well by introducing an aperture through a buried tunnel junction (BTJ), a single-mode operation is possible. VCSELs are epitaxially grown in the direction of the resonator axis and thus have a very thin active region. Consequently, the gain is meagre in a single round trip. These properties raise the need for high reflectivity mirrors - DBR - to overcome the threshold gain g_{th} described by

$$g_{th} = \alpha - \frac{1}{2L} \ln(R_1 R_2), \tag{2.56}$$

where α is the cavity loss, L is the optical cavity length and R_1, R_2 are mirror reflectivities. A short cavity length creates a large FSR which is beneficial for wavelength tuning of the device. Being a VCSEL, it is geometrically possibly to replace the top mirror with an actuated MEMS-DBR to create a tunable cavity. Two equations for carrier density N_e and photon density N_p describe the

[2]Tyndall National Institute, Lee Maltings, Dyke Parade, Cork, Ireland, www.tyndall.ie

rate-equations of a laser [12].

$$\frac{\mathrm{d}N_\mathrm{e}}{\mathrm{d}t} = \frac{\eta_\mathrm{i} I}{q V_\mathrm{ar}} - \frac{N_\mathrm{e}}{\tau_\mathrm{e}} - R_\mathrm{st} \tag{2.57}$$

$$\frac{\mathrm{d}N_\mathrm{p}}{\mathrm{d}t} = \Gamma \underbrace{v_\mathrm{g} g N_\mathrm{p}}_{R_\mathrm{st}} + \Gamma \beta_\mathrm{sp} R_\mathrm{sp} - \frac{N_\mathrm{p}}{\tau_\mathrm{p}} \tag{2.58}$$

Carrier density N consists of electron injection through current I with an internal efficiency η_i. q is the elemental charge of an electron and V_ar is the active region volume. Losses like carrier leakage, spontaneous emission and non-radiative recombinations are included in decay constant τ. Additionally stimulated emission rate R_st needs to be considered in the presence of photons. The temporal change of photon density N_p is described through stimulated R_st and spontaneous emission rates R_sp as well as decay with constant τ_p. $\Gamma = V_\mathrm{ar}/V_\mathrm{p}$ is called confinement factor describing the spatial overlap of volume V_ar of the active region occupied by electrons and cavity volume V_p occupied by photons. v_g is the group velocity, g is the gain per unit length and β_sp is the spontaneous emission factor.

A laser has two regions in a power P versus current I graph, which are connected by the threshold. Below the threshold, a laser behaves like a light-emitting diode (LED), electrical current is transformed into photons by spontaneous emission in all directions. There is no resonator designed specifically to enable multiple round trips, and no stimulated emission is occurring. The output power below threshold P_below can be written as

$$P_\mathrm{below} = \eta_\mathrm{c}\eta_\mathrm{i}\eta_\mathrm{r}\frac{h\nu}{q} I = \eta_\mathrm{ex}\frac{h\nu}{q} I, \tag{2.59}$$

where η_c, η_i, η_r and η_ex are net collection, internal, radiative and external efficiencies, respectively. They describe the efficiency of collecting emitted photons with an aperture (η_c), of carriers created by current I (η_i) and of creating spontaneous emission, respectively. η_ex combines all previous efficiencies. The threshold is given by a steady-state condition where eq. (2.57) equals to zero. Hereby, the losses are balanced by carrier generation while no stimulated emission is present ($R_\mathrm{st} = 0$), thus

$$\frac{\eta_\mathrm{i} I_\mathrm{th}}{q V_\mathrm{ar}} = \frac{N_\mathrm{th}}{\tau}, \tag{2.60}$$

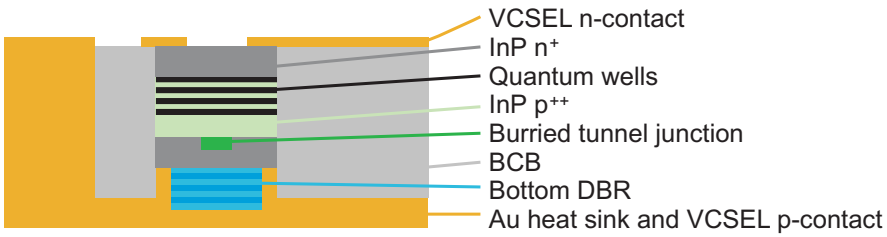

Figure 2.11: Cross-section of a high-speed half-VCSEL.

where I_{th} is called threshold current and N_{th} is threshold carrier density. Inserting eq. (2.60) in eq. (2.57), the behavior above threshold can be written as

$$\frac{\mathrm{d}N}{\mathrm{d}t} = \eta_{\mathrm{i}} \frac{I - I_{\mathrm{th}}}{qV_{\mathrm{ar}}} - v_{\mathrm{g}} g_{\mathrm{th}} N_{\mathrm{p}}, \tag{2.61}$$

where g_{th} is the gain at the threshold. Generally, gain depends on N. At the threshold condition, all carriers N_{th} are lost either by nonradiative recombination, spontaneous emission or carrier leakage. All additional carriers are transformed into photons by stimulated emission. This means that above threshold carrier density $N_{\mathrm{above}} = N_{\mathrm{th}}$ is constant which results in a constant gain $g_{\mathrm{above}} = g_{\mathrm{th}}$. This steady-state of N_{p} can be written as

$$N_{\mathrm{p}} = \frac{\eta_{\mathrm{i}}(I - I_{\mathrm{th}})}{q v_{\mathrm{g}} g_{\mathrm{th}} V_{\mathrm{ar}}}. \tag{2.62}$$

Transforming eq. (2.62) into an output power [12] and including internal and mirror losses, power above threshold P_{above} can be written as

$$P_{\mathrm{above}} = \eta_{\mathrm{d}} \frac{h\nu}{q} (I_{\mathrm{L}} - I_{\mathrm{th}}), \tag{2.63}$$

where η_{d} is the differential quantum efficiency describing the number of photons emitted from the laser per electron. Looking at the shape of a $I_{\mathrm{L}} - P$ graph, there are two linear regions with different slopes meeting at I_{th}. Above the threshold, R_{sp} is constant and creates a noise floor below the stimulated emission, which results in a reduction of output linewidth of the output wavelength with increased driving current. At some point, there is a thermal rollover when increasing I_{L} which is caused by additional carrier losses in the semiconductor due to heating, limiting the laser output power.

Figure 2.11 presents the cross-section of a half-VCSEL as the samples were received from Vertilas GmbH[3] and presented in [57] for example. The target of the design is a broad active region gain around 1550 nm center wavelength and fast direct modulation possibility for data communication purposes. A wide gain is achieved by introducing stress in the active region quantum wells. Minimizing the active mesa area by replacing most of the semiconductor material with insulating high dielectric constant material BCB (Benzocyclobutene) allows fast modulation. In the end, the mesa diameter is only 50 µm. A BTJ within InP p^{++}-layer both favors TEM_{00} mode within the cavity and acts as current confinement for higher efficiency. Within the Au heat sink, a DBR based on CaF_2/ZnS can be seen which in combination with Au has a broad reflectivity stopband above 300 nm. For easier contacting, the backside contact is brought to the front as well. Note that the n-contact leads to the center mesa, while p-contact leads to the backside.

[3] Vertilas GmbH, Daimlerstr. 11d, 85748 Garching, Germany, www.vertilas.com

3 Designing a SiO_x-SiC_z MEMS-DBR

Here, the designing process is explained step by step, beginning with a single-layer thin-film deposition. After several depositions, the available parameter region is outlined, which then is a basis for deciding upon recipes to create a layer stack - the DBR. When released, the DBR bends upwards creating an air-gap depending on the single-layer stresses. In the end, an evaluation of SiO_x-SiC_z MEMS-DBR filter tuning efficiency is performed.

3.1 Single Dielectric Layers

Single-layer depositions are performed and investigated to find a suitable dielectric layer for a MEMS-DBR. The main characteristics of a dielectric layer here, are the layer stress σ and the refractive index $n_{1550\text{nm}}$ at 1550 nm. Mainly, σ will later define the initial air-gap after the release of a MEMS, and as a result, determine FSR and tuning bandwidth. The sacrificial layer is much thinner and has only a limited influence on the air-gap. Larger compressive stress (negative value) increases the air-gap. SiO_x always shows compressive stress of $\sigma_{SiO_x} \approx -120\,\text{MPa}$. So for σ_{SiC_z}, a value as close to zero as possible is desirable here to create a small enough air-gap for a SiO_x-SiC_z-MEMS-DBR filter. $n_{1550\text{nm}}$ for SiC_z defines the maximum reflectivity R_{max} (eq. (2.39)) of a DBR through the refractive index difference $\Delta n = n_{high} - n_{low}$, where $n_{high} = n_{SiC_z}$ is the higher refractive index and $n_{low} = n_{SiO_x}$ is the lower refractive index.

In the following sections, first single-layer deposition parameters are investigated to find suitable characteristics for SiC_z. As a second step, these single layers are stacked to create a DBR. Subsequently, the reflectivity over wavelength is measured to find the position of the reflectivity stopband.

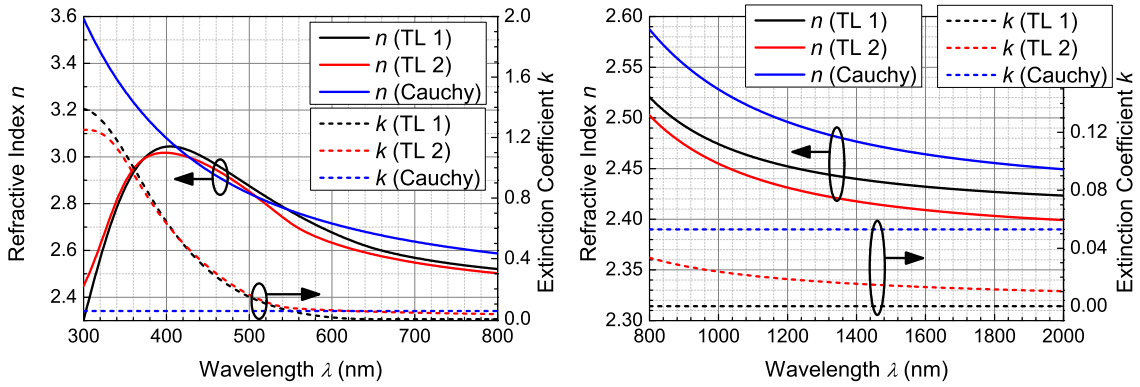

Figure 3.1: Three models used for fitting of Ellipsometry reflection measurements on a SiC_z layer. Two Tauc-Lorentz models with 1 (TL 1) and 2 (TL 2) oscillators, respectively and a Cauchy model. **Left:** Visible region with oscillators. **Right:** Near infrared region.

3.1.1 Characterization of Single Layers

A PECVD deposition grows a single dielectric layer on a two-inch single-side polished silicon substrate with lattice orientation (100). The layer thickness is targeted to be roughly $\lambda_0/(4n_{1550\text{nm}})$, where $\lambda_0 = 1550\,\text{nm}$ and $n_{1550\text{nm}}$ is the refractive index at 1550 nm. After the deposition, an ellipsometry measurement evaluates the wavelength-dependent refractive index and layer thickness of the dielectric layer. While the Cauchy model characterizes SiO_x layers which do not show any absorption in NIR range, a suitable model for SiC_z has to be chosen first. Since many sources claim small absorption in the NIR range, the Cauchy model might not be the right choice here. Although it does offer fitting parameters for the extinction coefficient k, it does not consider oscillators within the material. Tauc-Lorentz (TL) model, on the other hand, does work with oscillators and can reproduce such measurements. Here two TL models with one and two oscillators, respectively, are studied. While for the Cauchy model it is sufficient to measure reflection in NIR, the fitting process for TL works better if both visible (VIS) and near-infrared (NIR) regions are measured (300 nm to 1700 nm) to include the oscillators found in the visible range. The resulting wavelength-dependent n and k are presented in fig. 3.1.

While the difference in shape in NIR is small, in VIS range, the oscillators result in large variations. The most exciting difference is the absorption coefficient in NIR. Here the Cauchy model gives the highest value of 0.053, which

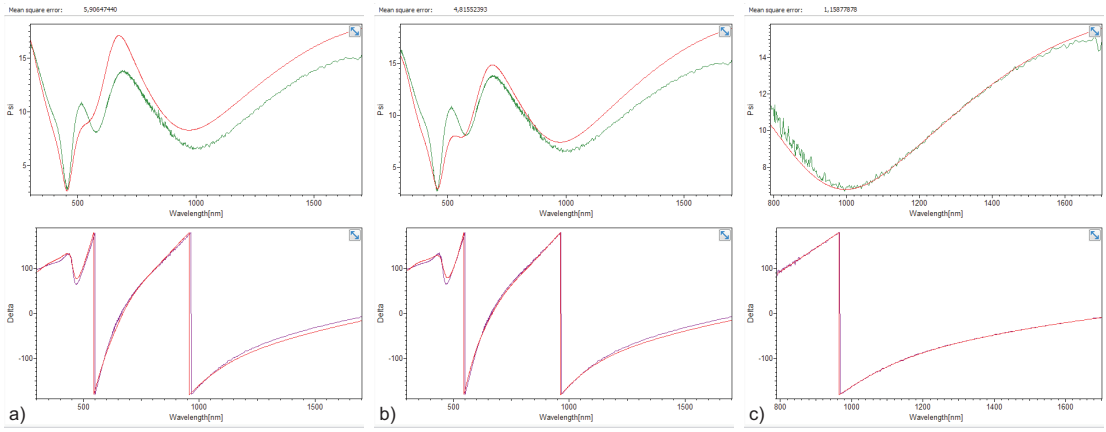

Figure 3.2: Fitting results for Ψ (top) and Δ (bottom) in red with green measurement data for three fitting models a) TL1, b) TL2 and c) Cauchy. Resulting MSE of 5.9, 4.8 and 1.2, respectively. Ranges of x-axes are 300 nm to 1700 nm for a) and b) and 800 nm to 1700 nm for c).

is wavelength-independent. TL1 model only shows absorption until approximately 650 nm at which position fitting assumes the optical bandgap. Above it, absorption cannot occur. TL2 model, on the other hand, includes absorption even in the NIR due to a second broad oscillator. Nevertheless, the value of approximately 0.01 to 0.02 is below the Cauchy model result. The refractive index difference of 0.056 at 1550 nm between TL2 and Cauchy is negligible because the fitted layer thickness behaves inversely (204 nm for Cauchy and 211 nm for TL2). The resulting optical thickness is comparable. The calculated deposition rate and refractive index, which are used to determine the required deposition time for a DBR will result in very similar optical thicknesses for each layer.

Figure 3.2 shows the fittings for Ψ and Δ for all three models. Fitting (red) and measured values (green) agree very well for Δ in all cases, which means the thickness determination is accurate for each model. For Ψ, the differences are larger. While TL1 model (a) does find the oscillator, TL2 (b) represents it much better, showing a smaller mean square error (MSE). In (c), Cauchy fitting is shown. Here only the NIR contributes to the fit. An MSE of 1.2 is the lowest for all, which is mainly due to a smaller wavelength range measured.

In the end, the Cauchy model is used throughout this thesis, because the measurement is less complex (only NIR needs to be measured) and easier to use (less fitting parameters).

Both before and after the deposition, the substrate radius of curvature was measured to calculate layer stress σ of the deposited layer by using eq. (2.53).

3.1.2 Optimization of Deposition Parameters

To deposit a SiC_z layer precursor, gases CH_4, SiH_4 and Ar are required. Ar is present to increase the number of collisions between the molecules, and thus, to increase the variety and amount of radicals present within the plasma. CH_4 and SiH_4 deliver the atoms necessary for a SiC_z layer. In this work, three parameters are investigated - deposition power, SiH_4:CH_4 ratio and deposition pressure[1].

The manufacturer gives a base recipe (see table 3.1) which is used and adjusted. The temperature is kept constant at 80 °C in all depositions. A water heating system delivers the necessary temperature and cannot be increased much further. The resulting layers are compared with σ and n_{1550nm}.

Table 3.1: Base SiC_z PECVD recipe.

Ar	SiH_4	CH_4	p	P_{RF}	P_{ICP}	T
15 sccm	3.5 sccm	3 sccm	7.5 mTorr	0 W	250 W	80 °C

Power Variation

The first variation is ICP power P_{ICP}. Both lower, as well as higher values for P_{ICP} are tested while keeping $P_{RF} = 0$. In one additional run (5), $P_{RF} = 50$ W is introduced. Table 3.2 summarizes all recipes.

P_{ICP} was increased from 200 W to 350 W in 50 W steps. Since the deposition at 200 W could not be evaluated with ellipsometry models, it is neglected in figure 3.3. When observing the black squares, the lowest compressive stress can be found at 250 W with $\sigma = -141$ MPa. Both other powers show a slightly larger value for compressive stress. The red balls show the corresponding refractive index, which behaves oppositely. Depositions at higher P_{ICP}, create a slightly larger refractive index. The connection between these two properties could be explained by larger incorporation of silicon atoms in the dielectric

[1] In all recipes pressure unit 1 mTorr $= 1.3 \cdot 10^{-3}$ mbar is shown to represent recipes used by Oxford controlling software.

Table 3.2: Recipes for power variation of SiC_z PECVD depositions.

#	Ar (sscm)	SiH_4 (sccm)	CH_4 (sccm)	p (mTorr)	P_{RF} (W)	P_{ICP} (W)	T (°C)
1	15	3.5	3	7.5	0	**200**	80
2	15	3.5	3	7.5	0	**250**	80
3	15	3.5	3	7.5	0	**300**	80
4	15	3.5	3	7.5	0	**350**	80
5	15	3.5	3	7.5	**50**	**250**	80

layer. Crystalline silicon has a refractive index of about 3.4 and crystalline carbon about 2.4. In general, it can be said that P_{ICP} has a low influence on the layer stress and refractive index. Where a clear dependency is obvious, is the deposition rate. It grows from 11.3 nm/min at $P_{ICP} = 250$ W through 13.4 nm/min at $P_{ICP} = 300$ W to 14.6 nm/min at $P_{ICP} = 350$ W.

Recipe 5 from table 3.2 additionally applies the RF generator with a power of $P_{RF} = 50$ W. The result (two circled dots in fig. 3.3) is both a much higher compressive stress at almost -300 MPa and a much lower refractive index at $n_{1550nm} = 2.27$. Thus, the addition of the RF generator is excluded from further tests. An explanation for this behavior could be the larger DC bias created between the top electrode and the bottom-electrode where the sample is located. Thus, ions accelerate faster towards the sample surface, creating more defects in the layer, which results in a larger layer-stress.

SiH_4:CH_4-Ratio Variation

In the second run, SiH_4 and CH_4 deposition ratios are investigated. A higher ratio of silicon compared to carbon within the layer increases the refractive index according to [1]. To keep the total gas flow constant only the ratio between SiH_4 and CH_4 changes while the sum (SiH_4 +CH_4 = 6.5 sccm) remains constant. The recipes, thus, are summarized in table 3.3.

First, the black squares in fig. 3.4 are discussed. A larger SiH_4:CH_4 ratio means more SiH_4 molecules and its radicals are present in the plasma, compared to CH_4 molecules and radicals. As a result, a compressive layer is growing (more negative values). As described in section 2.5, layer-stress is introduced through defects in the crystalline structure of the dielectric layer. So, in this case, a bigger SiH_4:CH_4 ratio introduces more defects within the deposited layer. Looking

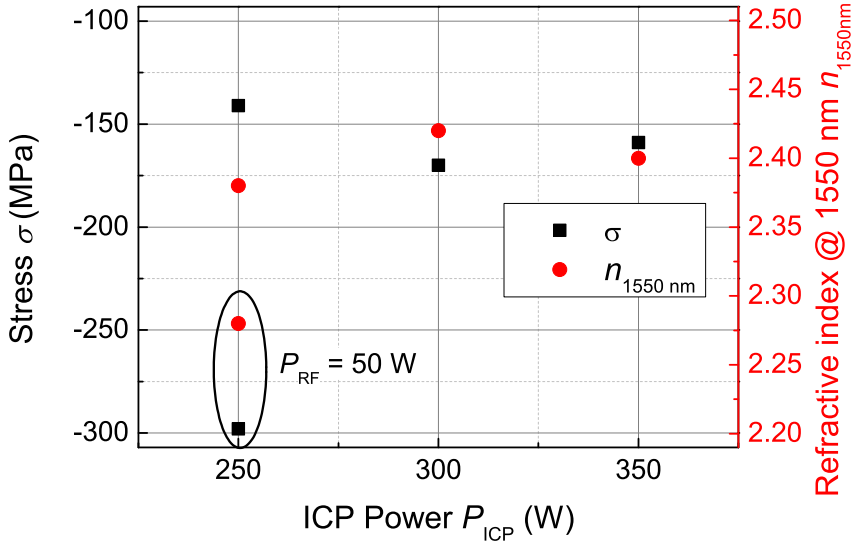

Figure 3.3: Layer stress σ and refractive index at 1550 nm $n_{1550\text{nm}}$ for varying deposition power P_{ICP}. The two points in the lower left show results with additional RF power of the second generator.

Table 3.3: Recipes used for SiH_4:CH_4-variation. The total gas flow is kept constant SiH_4 +CH_4 =6.5 sccm.

#	Ar (sccm)	SiH_4 (sccm)	CH_4 (sccm)	SiH_4:CH_4	p (mTorr)	P_{RF} (W)	P_{ICP} (W)	T (°C)
1	15	**3.5**	**3.0**	**1.17**	7.5	0	250	80
2	15	**3.8**	**2.7**	**1.41**	7.5	0	250	80
3	15	**4.0**	**2.5**	**1.60**	7.5	0	250	80
4	15	**4.3**	**2.2**	**1.95**	7.5	0	250	80
5	15	**5.0**	**1.5**	**3.33**	7.5	0	250	80

at $n_{1550\text{nm}}$ (red balls), it is expected to have a larger value when more SiH_4 is present in the plasma. This step can is partially visible in the increase of $n_{1550\text{nm}}$ from the first to the second point. However, after that, it seems to saturate. So, either more or different defects are resulting, but the refractive index does not change anymore. For the extreme case of SiH_4:CH_4 =5:1.5 (3.33), it is not possible to create an optical model with ellipsometry to describe the layer, which is why this value is not displayed here. In conclusion, here, the desirable recipe

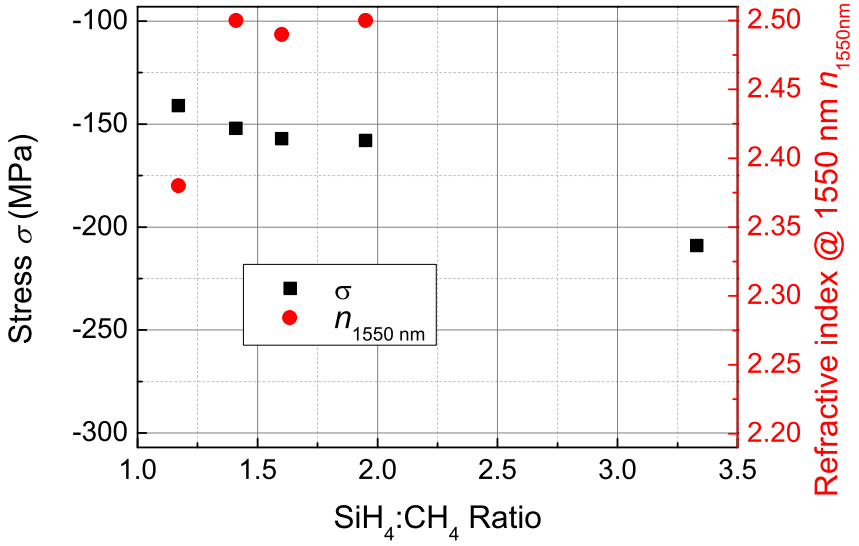

Figure 3.4: Layer stress σ and refractive index at 1550 nm $n_{1550\text{nm}}$ for different gas ratios but constant total gas flow SiH_4 + CH_4 = 6.5 sccm.

is number two.

Deposition Pressure Variation

Finally, the pressure is varied around the base recipe, in 1 mTorr-steps creating recipes from table 3.4.

Table 3.4: Deposition pressure variation for SiC_z layers.

#	Ar (sccm)	SiH_4 (sccm)	CH_4 (sccm)	p (mTorr)	P_{RF} (W)	P_{ICP} (W)	T (°C)
1	15	3.5	3	**5**	0	250	80
2	15	3.5	3	**6**	0	250	80
3	15	3.5	3	**7**	0	250	80
4	15	3.5	3	**7.5**	0	250	80
5	15	3.5	3	**8**	0	250	80
6	15	3.5	3	**9**	0	250	80
7	15	3.5	3	**10**	0	250	80

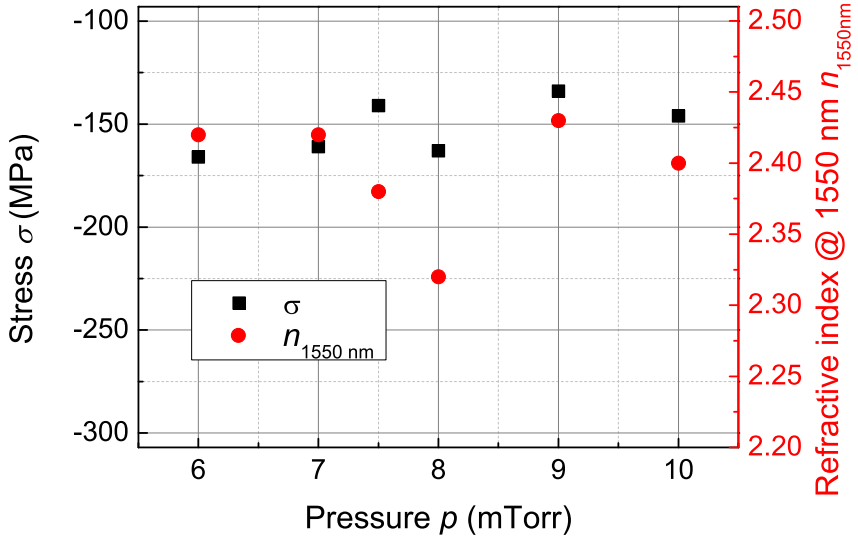

Figure 3.5: Layer stress σ and refractive index at 1550 nm $n_{1550\text{nm}}$ for varying deposition pressures.

The pressure is the most delicate parameter of a low-temperature PECVD deposition as seen in previous tests with SiN_y. There, a change of 0.5 mTorr could already change σ by a great amount, even going from compressive to tensile stress. The first recipe at $p = 5$ mTorr is not shown in figure 3.5, as it is too low for a stable plasma - deposition is not possible. The other depositions show a small change in σ with the best values for 7.5 mTorr and 9 mTorr. As $n_{1550\text{nm}}$ is larger for $p = 9$ mTorr, this is the desirable recipe. Since there is no evident trend visible when comparing p and σ, it is not possible to tell anything about the processes responsible for these results. In general, the pressure defines the mean distance between the radicals in the plasma. Thus, certain pressures might favor the creation of specific radicals by changing the probability of certain collisions. With this view, it can be explained why the jumps of σ seem random. For further analysis of this phenomena, a more stable deposition chamber is necessary where the stability of the pressure can be kept at $\Delta p = 0.1$ mTorr. With such a machine, it could be possible to find a local maximum for a more suitable σ but at a price of that parameter set being very unstable.

Verdict

The investigation of deposition parameters shows that it is possible to deposit SiC_z layers with a layer stress range between $-141\,MPa$ and $-298\,MPa$. Since all values are negative, only compressive stress is possible. In combination with compressive SiO_x layer, a SiO_x-SiC_z MEMS-DBR is bound to have a huge initial air-gap. A beneficial point in the deposition of SiC_z layer is the relative stability of the deposition parameters. Small changes in power and precursor gas mixture, do not influence layer stress drastically. Only the chamber pressure needs to be kept as stable as possible to stay on the local minima for low compressive layer stress.

3.1.3 Dry-Etching Recipe for SiC_z and SiO_x

After a DBR is created by growing a stack of single dielectric layers, at a later point in the processing of a MEMS-DBR, they have to be structured. As mentioned in section A, this can be done with plasma dry-etching employing fluoride-containing gases. The recipe in table 3.5 has a similar etch-rate (approximately $100\,nm/min$ to $150\,nm/min$) for both SiO_x and SiC_z layer. This means a DBR is etched constantly as well. It opens the possibility for a well-defined etch-depth when required.

Table 3.5: Recipe with similar etch rate for both SiO_x and SiC_z.

CF_4	CHF_3	Ar	O_2	p	P_{RF}
25 sccm	25 sccm	20 sccm	50 sccm	75 mTorr	300 W

3.2 Layer Pair Requirements for a DBR

The first question that arises when designing a DBR is the necessary number of layer-pairs to achieve a high reflectivity for a wide stopband. A large reflectivity reduces the linewidth of the filtered signal according to eq. (2.18), and a large reflectivity stopband enables a broad tuning range. Equation (2.39) shows a graphic description of fig. 3.6 with $n_{out} = 3.2$ and $n_{in} = 1$ being refractive indices at the output and input of the DBR, respectively and n_H and n_L describe

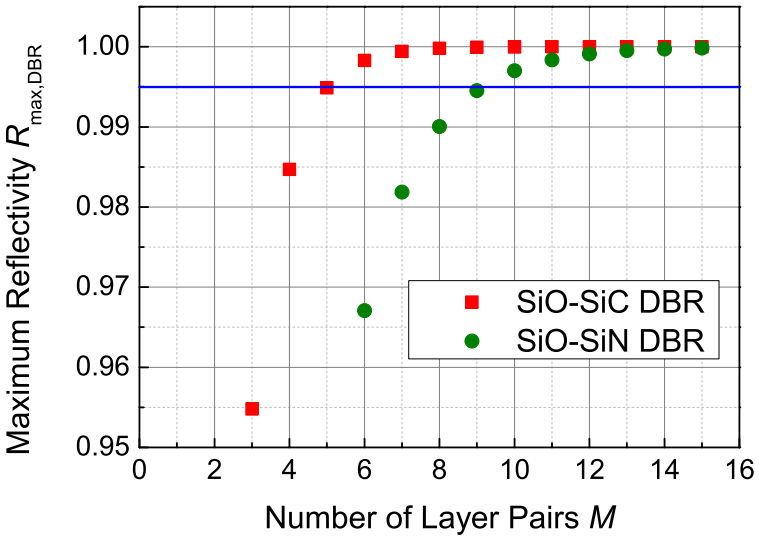

Figure 3.6: Maximum reflectivity depending on number of layer-pairs deposited on a silicon substrate with $n_{Si} = 3.2$. The refractive indices for the dielectric layers are $n_{SiO_x} = 1.45$, $n_{SiN_y} = 1.92$ and $n_{SiC_z} = 2.46$. In blue, a line for 99.5 % is shown.

the high and low refractive index of the alternating layers. The values depend on the number of layer-pairs M deposited on a silicon substrate.

From fig. 3.6, it can be extracted that a SiC_z-based DBR needs less layer-pairs to reach a high reflectivity of $> 99.5\,\%$, in comparison to a SiN_y-based DBR. At least 6 layer-pairs are required for SiC_z, while SiN_y needs at least 10 layer-pairs. This behavior comes from a larger refractive index difference Δn of the two materials used for a DBR.

Next, investigation of the reflectivity stopband depending on layer-pairs on a Si substrate is described. In fig. 3.7, a comparison between a SiO_x-SiC_z (red lines) and SiO_x-SiN_y DBR (olive lines) is shown for different numbers of layer-pairs on a silicon substrate. Both combinations reach high reflectivities as already seen in fig. 2.7 but the bandwidth of the reflectivity plateau is much broader for SiO_x-SiC_z DBR due to its much larger refractive index contrast ($\Delta n_{SiO_x\text{-}SiC_z} = 1$ and $\Delta n_{SiO_x\text{-}SiC_z} = 0.39$ to 0.47). Two different values for SiO_x-SiN_y DBR represent previous publications of SiO_x-SiN_y MEMS-DBR VCSEL [57]. As discussed in section 2.3, more layer-pairs increase the reflectivity. The blue line marks the

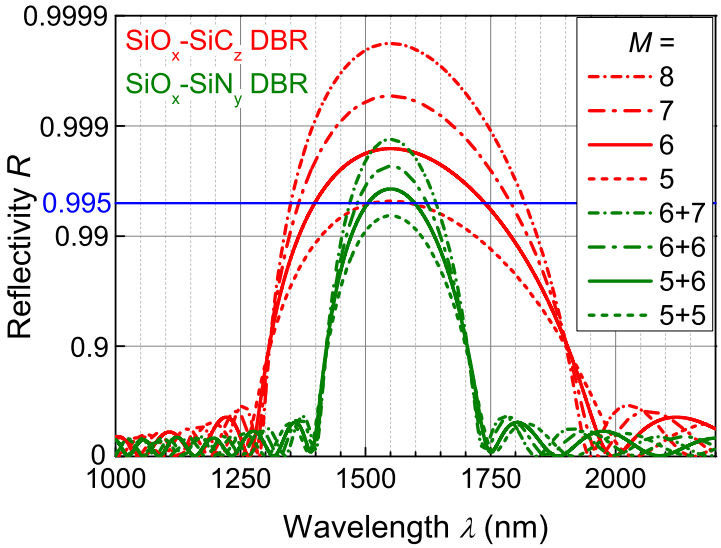

Figure 3.7: Simulated DBR reflectivities on Si substrate surrounded by air. In red, for $M = 5$ to 8 SiO_x-SiC_z DBR with refractive indices $n_{H,SiC_z} = 2.45$ and $n_{L,SiO_x} = 1.45$. In olive, for SiO_x-SiN_y DBR two different values for $n_{H,SiN_y\,1} = 1.84$ and $n_{H,SiN_y\,2} = 1.92$ were taken. In the legend $M = M_{SiN_y\,1} + M_{SiN_y\,2}$ for SiO_x-SiN_y DBR. In blue reflectivity of 99.5 % is visualized.

stopband for very high reflectivities ($R > 99.5\,\%$). While for SiO_x-SiN_y DBR only a high reflectivity stopband of 100 nm is achieved for 11 layer-pairs. 6 layer-pairs of SiO_x-SiC_z have a high reflectivity stopband of 243 nm. Also, 5 pairs of SiO_x-SiC_z barely touch the 99.5 %-line. Please see fig. B.2 for actual reflectivity measurements of SiO_x-SiN_y and SiO_x-SiC_z DBRs on a Si substrate, performed with ellipsometry at 40° incident angle. First, a DBR with 6 layer-pairs is fabricated for a filter to compare the material influence only.

3.3 Stability of Deposition Parameters

During a deposition, dielectrics not only grow on the desired sample but on most surfaces within the PECVD chamber, especially on the electrodes. After deposition of several micrometers, usually after a DBR deposition, the chamber is cleaned with an SF_6 plasma to remove all residues. This is necessary as the porous surface can adsorb humidity which then is slowly released into

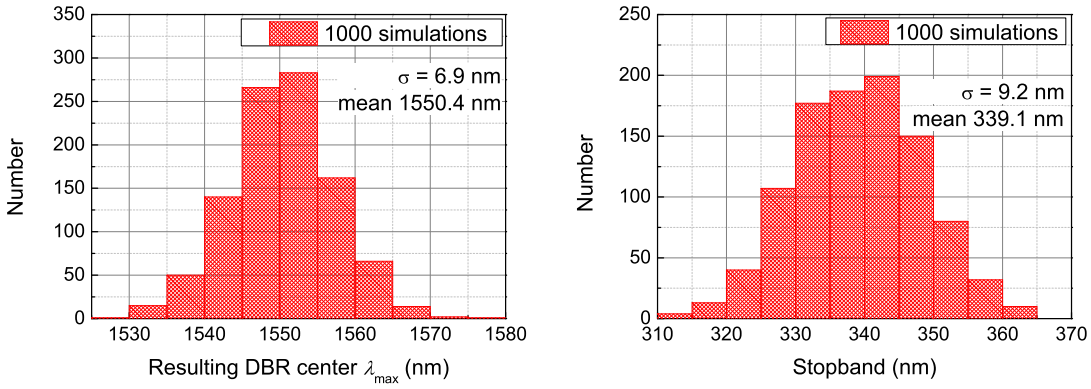

Figure 3.8: 1000 simulations with random individual variations for both thickness and refractive index. **Left:** Resulting DBR center-wavelength. **Right:** Resulting stopband width.

the vacuum resulting in a less efficient pumping. This increases process time and could also influence the deposited layer compositions. Moreover, after approximately 10 µm, the residues on the chamber walls and electrodes can flake off and land on the sample acting as a mask and creating undesired structures. After each cleaning procedure, the chamber is preconditioned with a stack of 3 layer-pairs (SiO_x-SiC_z) having layer thicknesses of approximately 130 nm each. Preconditioning is necessary to cover all surfaces with a dielectric material, so during a deposition on a sample, similar conditions are met. Otherwise, a different layer composition on the sample may result. Cleaning and resetting the chamber conditions after each DBR, raise the question of whether it influences the deposition itself. Whether it is stable in case of deposition rate and layer composition and whether it is necessary to calibrate the deposition after each cleaning and which influences a shifted layer thickness has on DBR reflectivity. After several depositions and cleaning steps, layer properties are investigated. It is perceived that a change in deposition rate r_{dep} of about 4 % and in refractive index $n_{1550\mathrm{nm}}$ of 3 % occurs. Comparisons before and after a DBR deposition do not show a significant shift in either deposition rate or refractive index. This leads to the assumption that during a DBR deposition, r_{dep} and $n_{1550\mathrm{nm}}$ remain constant as well. Several simulations were performed using the transmission matrix method similar to the one used for fig. 3.7 to see the influence of said shift on the position of maximum reflectivity and stopband. As before, layer thickness is set to $\lambda_0/4$ and refractive indices are chosen as $n_{1550\mathrm{nm},SiO_x} = 1.45$ and $n_{1550\mathrm{nm},SiC_z} = 2.45$. However, additionally, a random factor f_1 in the range

of 0.98 and 1.02 was multiplied with each layer thickness independently. It represents a variation in deposition rate by 4 %. A second random factor f_2 in the range of 0.985 and 1.015 is multiplied with each refractive index to represent a maximum variation of 3 %.

Figure 3.8 displays the result for 1000 simulations. On the left, the shift of the DBR center-wavelength is presented. While the center is still at the desired wavelength of 1550 nm a shift of ± 10 nm can occur due to variation in optical thickness. On the right, the stopband width is shown, which also shifts, because each layer is varied individually. In conclusion, a variation does occur, but the effect on the performance of the DBR should be minute.

3.4 Tuning Efficiency

The tuning efficiency explains the correlation between the Farby-Pérot cavity length change and the resonant wavelength shift. It is not linear due to the DBR reflectivity - the reflection of a DBR bases on the interference of multiple back-reflections at each layer interface. Layer thicknesses have an optical length of $\lambda_c/4$. So, for the center-wavelength λ_c, reflectivity is at its maximum and ideally equals to 1. This case is presented in green in fig. 3.9. At this moment, nodes and anti-nodes of the incoming mode coincide with each interface between high (H) and low refractive index material (L). This behavior is the same as for metal mirrors where the nodes are always at the interface. The required displacement to go from one resonant mode to the next at λ_c is $\lambda_c/2$ according to eq. (2.13). However, at the positions in between, the behavior is non-linear. To understand this, fig. 3.9 shows one side of a DBR FPR. When the mirrors move closer together, both cavity length and resonant wavelength shrink. The node, previously located at the first interface (air-H), moves inside the first layer until maximum offset towards the initial configuration is reached (blue case at the top of fig. 3.9). Now, the anti-node occurs close to the air-H interface. The mode's energy is mainly located in material L. The opposite behavior appears for cavity extension. The interface node moves inside the cavity until a $\pi/2$-shift in comparison to the blue case occurs. For a larger cavity length, the energy is mainly located in material H. Thus, the incident wave experiences ultimately different effective wavelength-dependent refractive indices $n_{\text{eff}}(\lambda)$. Please note that the offset is shrinking further inside the DBR, almost fitting to the interface [77]. With larger Δn, the effective refractive index difference also grows. Effective cavity-length does not change at the same speed as geometric

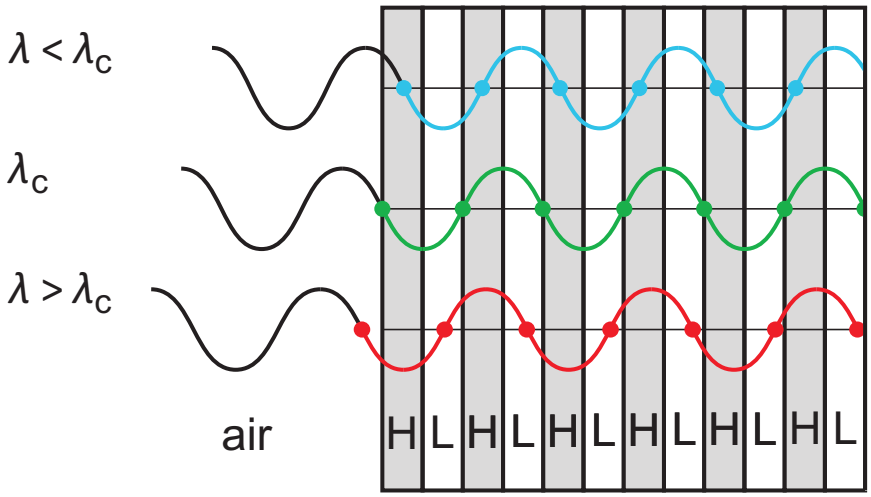

Figure 3.9: E-field distribution within a DBR FPR with high (H) and low refractive index material (L) designed for a center-wavelength λ_c. For simplicity, only the right cavity mirror is shown. Incident light comes from the left (air). Reduction of cavity-length creates top condition (blue) and extension creates bottom condition (red). Exponential decay into the DBR was omitted.

cavity length. Hence, tuning efficiency is non-linear. Accordingly, FSR is not constant while changing cavity length because at different distances from λ_c the offset induced by node movement differs. Figure 3.9 shows the same wavelength for all three cases because of simplification. Moreover, the optical thickness is presented, which results in the same thickness for H- and L-layers.

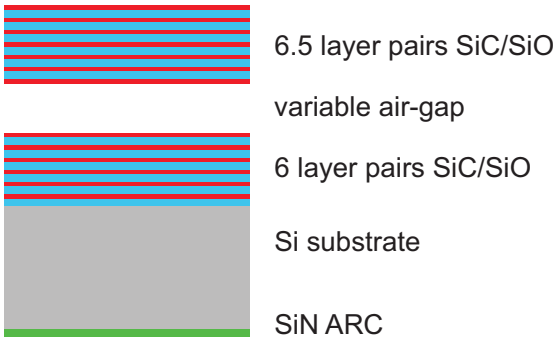

Figure 3.10: Layer stack used to calculate transmission with TMM for variable air-gap. Refractive indices used are: $n_{SiC_z} = 2.45$, $n_{SiO_x} = 1.45$, $n_{Si} = 3.67$ and $n_{SiN_y} = 1.82$.

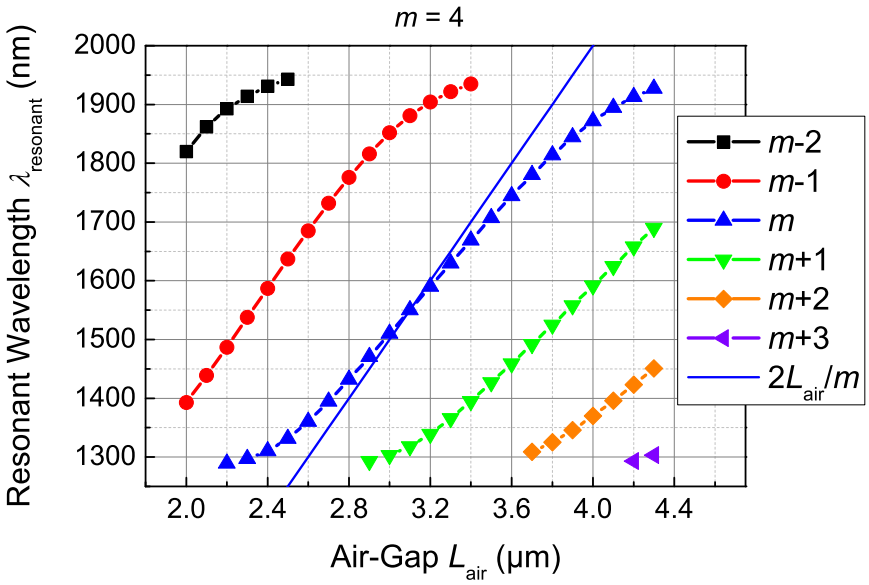

Figure 3.11: Tuning efficiency for mode $m = 4$. Blue line describes linear relation according to eq. (2.17).

The wavelength range between top and bottom cases from fig. 3.9 is called DBR band-gap. It describes the wavelengths which do not have a steady-state inside the DBR. Consequently, energy cannot pass and is reflected instead.

The transfer matrix method is used to calculate transmission of an FPR for different cavity lengths around 10 µm and 3 µm. A layer stack comprising two DBRs separated by a variable air-gap on a 300 µm Si substrate and a SiN_y ARC on the backside are used, shown in fig. 3.10.

In both figs. 3.11 and 3.12, the y-axis ranges display the same range because the tuning range is limited by the DBR stopband. fig. 3.11 shows an air-gap range of 2 µm to 4.3 µm and fig. 3.12 shows a range of 9 µm to 15 µm, respectively. Particularly with lover cavity lengths non-linearity is evident when moving from the designed center-wavelength of 1550 nm. The tuning efficiency shows an S-shape, similar to reports in [13]. The blue and pink lines represent calculated resonant wavelengths depending on the physical cavity length, derived from eq. (2.13).

$$\lambda_{\text{resonant}} = \frac{2L_{\text{air}}}{m}, \tag{3.1}$$

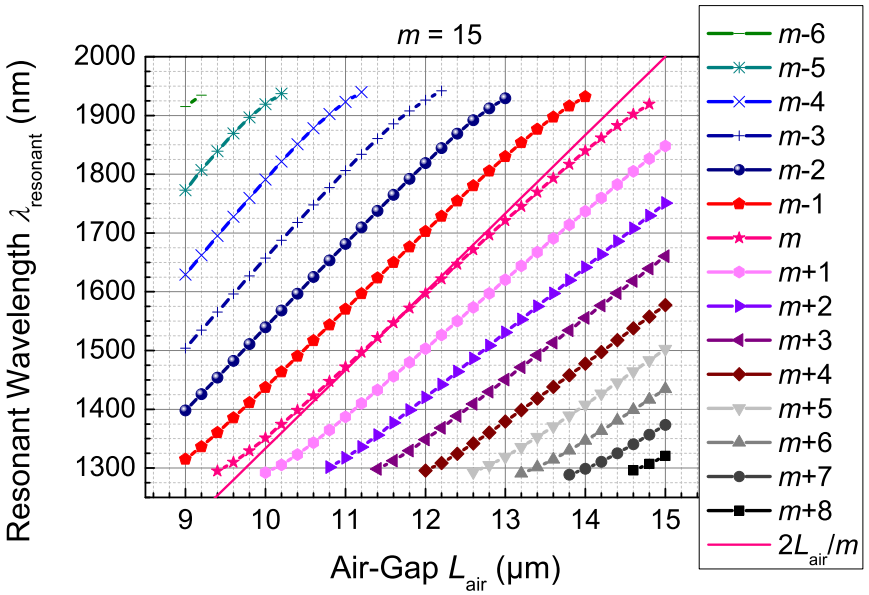

Figure 3.12: Tuning efficiency for mode $m = 15$. Pink line describes linear relation according to eq. (2.17).

with $m = 4$ in fig. 3.11. It is only at this point that the position and slope match the blue line. The reason for this is the DBR center-wavelength. It is comprised of layers with thickness $\lambda_c/4n_i$, where $\lambda_c = 1550\,\text{nm}$. For shorter and longer wavelengths, this requirement is not met. The E-field nodes do not occur at the interface air-SiC_z but either move inside the DBR or the cavity instead. Thus for values below and above the designed DBR center-wavelength, a smaller tuning efficiency is experienced.

In fig. 3.12, many modes are present at every single air-gap value because the FSR (vertical distance between these two points) is much smaller than the DBR reflectivity stopband. Around the center-wavelength where reflectivity is beyond 99.5 %, tuning efficiency is nearly linear but shows a smaller slope than eq. (2.13).

In figs. 3.13 and 3.14, a more detailed look at the FSR between modes 4 and 5, and 15 and 16, respectively, is presented. On the x-axis in both figures, a detuned air-gap shows the offset from a resonant cavity length for λ_c. $0\,\mu\text{m}$ thus describes a cavity length of $L_{\text{air,m}} = m\lambda_c/2$. FSR is, in both cases, highly non-linear and even shows a maximum FSR at a value larger than zero. It means when performing electro-thermal tuning which extends the cavity, the

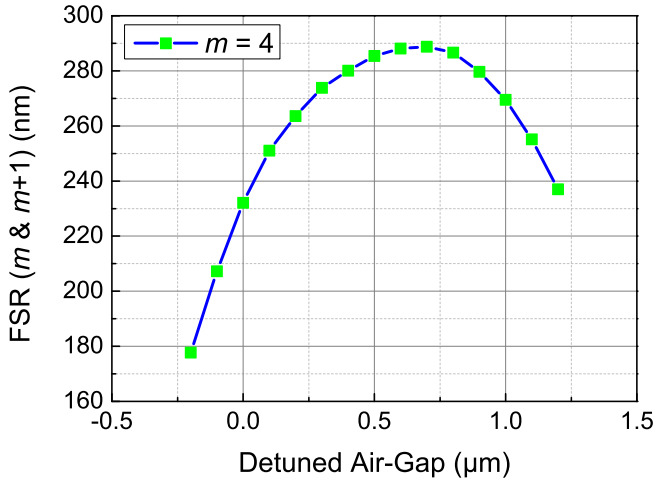

Figure 3.13: FSR between mode 4 and 5 depending on detuned air-gap. 0 µm corresponds to a cavity length $L_{\text{air}} = 4\lambda_c/2$ at the DBR center-wavelength λ_c.

FSR is growing until a certain point. Comparing fig. 3.12 and fig. 3.14, increasing resonant wavelength by 100 nm from λ_c, requires a MEMS-DBR displacement of approximately 1 µm. At this point, the FSR does not yet reach its maximum. So

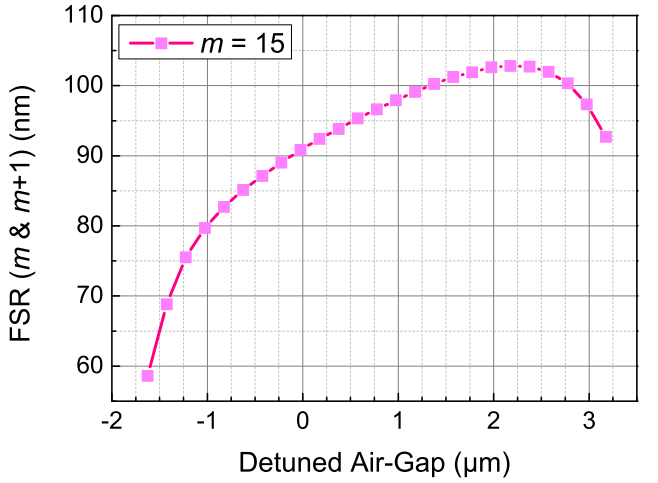

Figure 3.14: FSR between mode 15 and 16 depending on detuned air-gap. 0 µm corresponds to a cavity length $L_{\text{air}} = 15\lambda_c/2$ at the DBR center-wavelength λ_c.

it can be said that for the tuning performed in this thesis, FSR always increases with larger cavity length, if no mode-hop occurs.

4 MEMS-DBR Tunable Filters

In this chapter, the processing and results of SiO_x-SiC_z MEMS-DBR-based optical filters are presented. In the beginning, processing steps are listed, and tests on sacrificial layer masks are performed. Next, setup and alignment information are presented, followed by optical filtering properties and tunability. It is shown that a reduction in cavity-length is unavoidable to use the benefits of a SiO_x-SiC_z-based DBR. Thus, the chapter concludes with methods to achieve such a change with its corresponding characterizations.

4.1 Standard-Sized MEMS-DBR

The first section presents the suitability of the SiO_x-SiC_z material choice to build a MEMS-DBR tunable optical filter. Photolithography masks are not changed in the beginning to keep the number of adjusted variables in comparison to the available MEMS-DBR knowledge to a minimum. Once the proof of principle affirms, in the next section, optimizations are performed.

4.1.1 Processing

Processing of a MEMS-DBR filter with the means of surface-micro-machining requires several photolithography steps to structure metal and dielectric layers. Wet etching defines and removes metal structures where either lift-off is not beneficial or where they are only required temporarily - like sacrificial layer. Moreover, two DBR depositions and several metal evaporations are performed. First, photolithography masks are presented, and secondly, processing steps are summarized.

Figure 4.1 displays three masks. The first defines the sacrificial layer. The second shows the top electrode with a central aperture for light to enter the resonator. It is important to have two separate parts for contacting (top and bottom) so

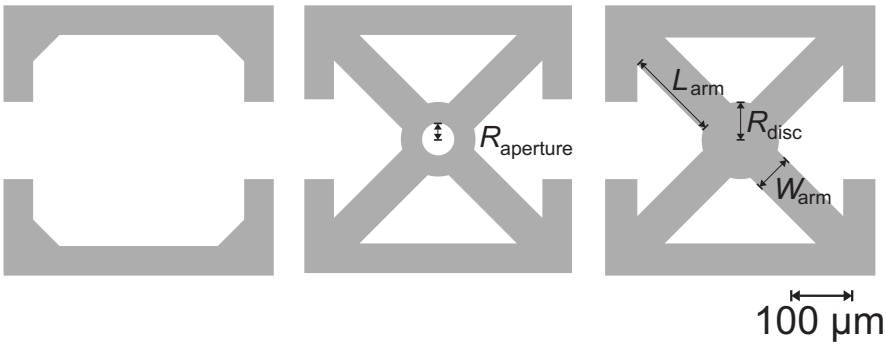

Figure 4.1: Photolithography masks for standard-sized MEMS-DBR tunable filters. **Left**: Sacrificial layer. **Center**: Top electrode. **Right**: MEMS etch mask.

I_{MEMS} will flow through the central disc around the aperture for electro-thermal actuation. The third mask defines the MEMS size by the structuring Ni dry-etching mask. Here, sizes for length L_{arm} and width W_{arm} for the beams, and R_{disc} and $R_{aperture}$ for the radius of MEMS disc and aperture, respectively, are noted. The targeted sizes are summarized in table 4.1. Each mask consists of a two-dimensional array with a pitch of 500 µm.

Table 4.1: Measures for standard-sized MEMS-DBR etching mask from fig. 4.1.

L_{arm}	W_{arm}	R_{disc}	$R_{aperture}$	pitch
144 µm	60 µm	60 µm	25 µm	500 µm

The following four figs. 4.2 to 4.5 present the main steps with a microscopy top view of the sample (center) and two schematic cross sections, across (left) and diagonal (right) to identify layer sequences at each position. Additionally, more detailed information on processing, including each cleaning step in between can be found in **??**.

A DBR is deposited on a both-side-polished (100) crystalline Si wafer (thickness $\approx$ 300 µm) broken into approximately 1 cm $\times$ 1 cm pieces in fig. 4.2 a). For the highest reflectivity, the first layer is low refractive index material SiO_x with an optical thickness of $\lambda/4$. In the second row b) a Ni sacrificial layer is evaporated using an e-beam system. An oscillating quartz crystal monitors the thickness during deposition. The targeted thickness is about 400 nm. At this point, lift-off is avoided to prevent fencing at the edges of a PR. Tests show a height of sidewalls of more than double layer thickness. Especially at the connection between the movable MEMS beam and the fixed DBR, fencing might cause

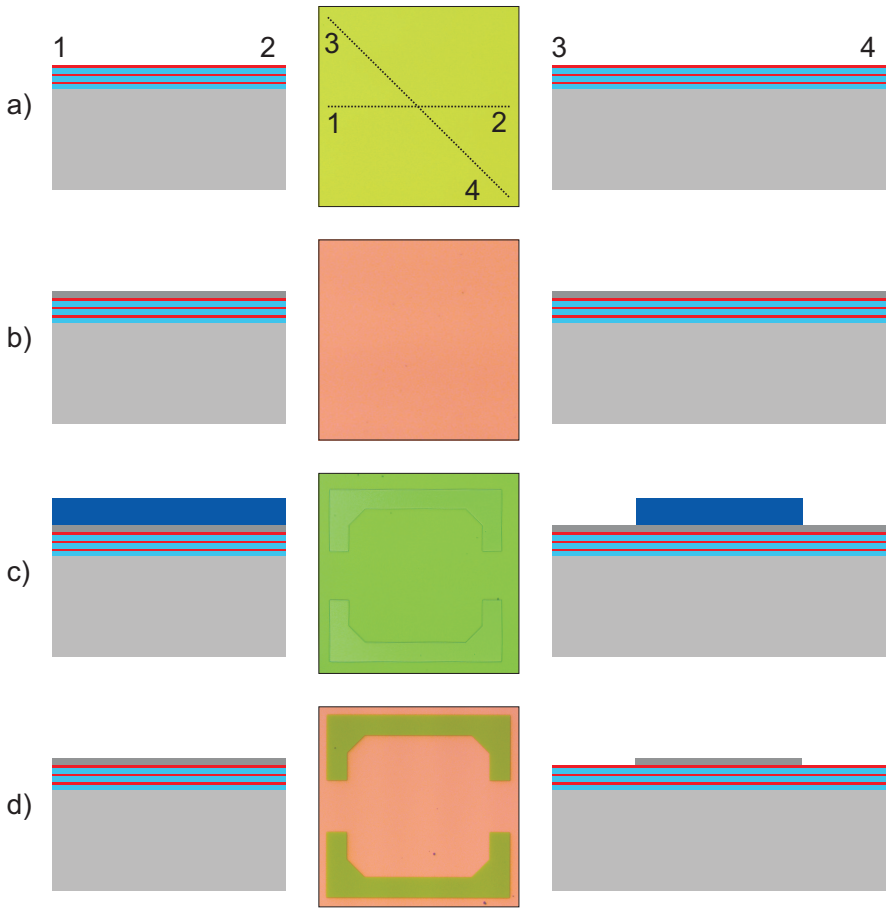

Figure 4.2: Bottom-DBR deposition and structuring of Ni sacrificial layer. **Left**: Cross-section across processed sample. **Center**: Microscope picture of the sample. **Right**: Diagonal cross-section of the processed sample. **a)** Bottom-DBR deposition on a both-side-polished Si-wafer. **b)** Ni sacrificial layer evaporation. **c)** Structured PR. **d)** Wet-etched Ni layer, PR removed.

breaking. Photolithography is performed with a positive resist (AZ1518) and a final thickness of 1.5 µm structures the sacrificial layer, shown in blue in row c). Now for the first time, a shape in the center picture is visible. At this point, the shape of the PR is observed under green light illumination to exclude any further UV exposure if additional development is needed. In the last group d) of fig. 4.2, the exposed Ni is etched for 90 s with a diluted HNO_3 (65 %, 1:30) solution at 50 °C while stirring of liquid was active. Finally, acetone cleans the surface and removes the PR.

In fig. 4.3 e), top-DBR is deposited on the sacrificial layer. Because in the final

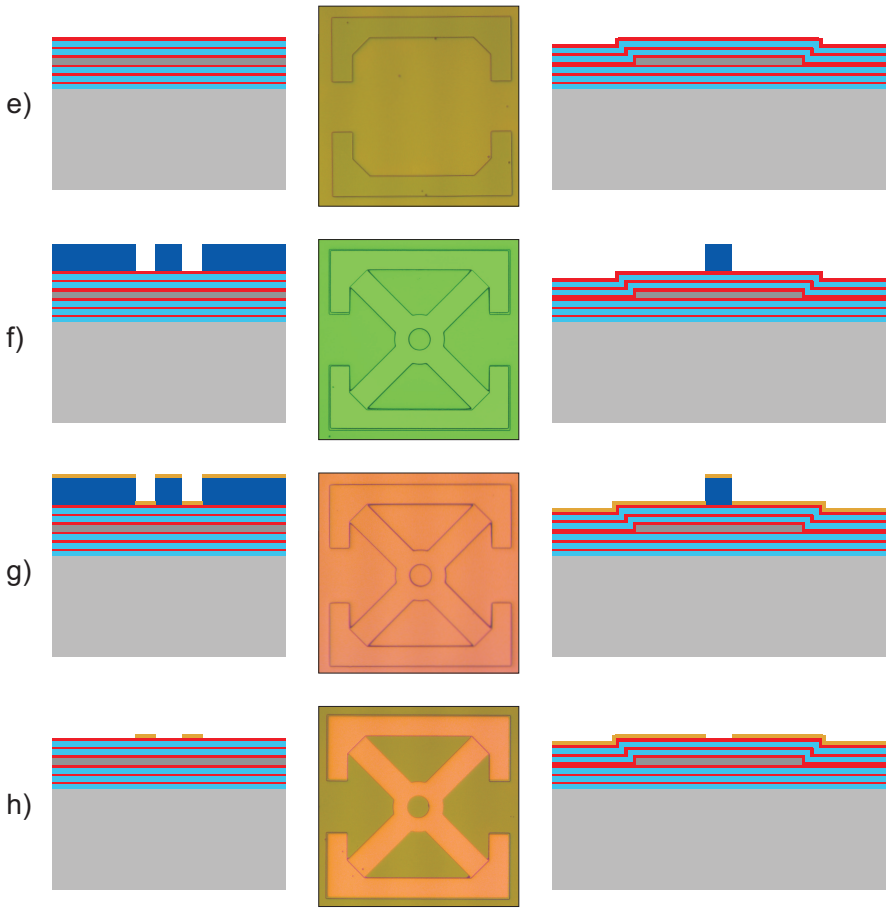

Figure 4.3: Top-DBR deposition and top Ti/Au-electrode lift-off structuring. **e)** Top-DBR deposition. **f)** Photolithography for lift-off. **g)** Ti/Au evaporation. **h)** Lift-off with acetone.

state, both sides of top MEMS-DBR are in contact with air, the DBR needs to begin and end with high refractive index material SiC_z. For the sake of clarity, only 2-3 layer pairs are used for each DBR in the schematic drawings. On the right side, the last SiC_z layer of bottom-DBR and the first SiC_z layer of top-DBR are in contact. These positions correspond to the top left and bottom right corners of the structure and represent the fixed MEMS-DBR part. In row f), photolithography is performed with an irPR (AZ5214E). This PR is used at this point because the top-electrode mask needs to be aligned to the sacrificial layer. As the sizes of the electrodes are slightly smaller than the sacrificial layer, it is required to see the edges of the previous structures. Moreover, removing the PR during the lift-off process itself is the most reliable and fastest with this choice.

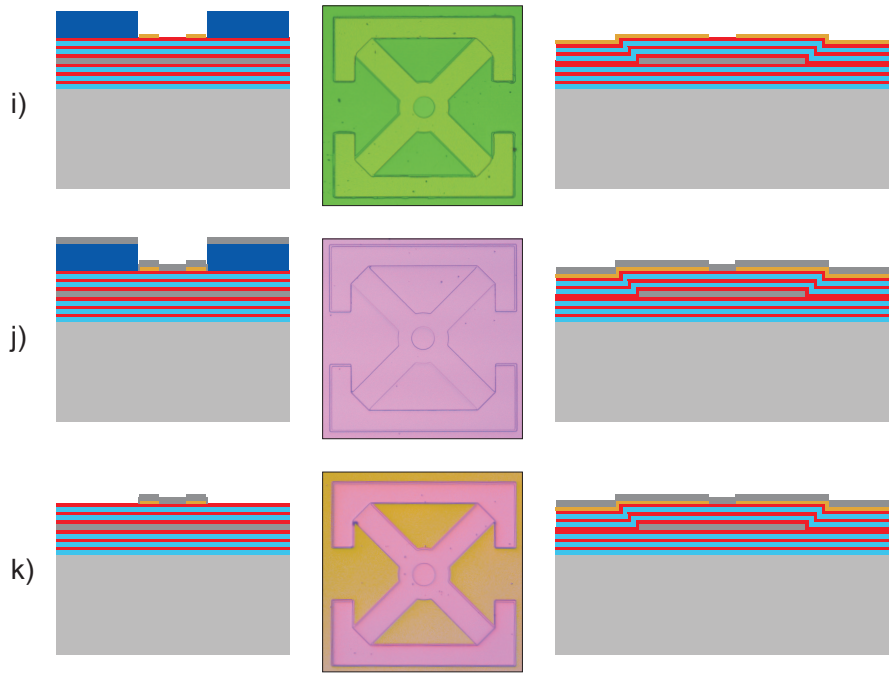

Figure 4.4: Ni etch mask lift-off for MEMS-structuring. **i)**: Photolithography for lift-off. **j)** Ni etch-mask evaporation. **k)** Lift-off with acetone.

For an image reversal PR, UV exposed areas remain after developing. Thus metallization of the mask is reproduced on the sample for lift-off. Row g) shows the Ti/Au evaporation. Both exposed sample areas and the PR are metalized. Ti is evaporated with e-beam, Au is heated with an electrical current until it evaporates. Both steps are done back to back in the same vacuum chamber. In the last group h), acetone performs the lift-off. After waiting for 20 s to 30 s, a syringe with a spraying cap adds a pressurized acetone flow.

In fig. 4.4 i), a second photolithography step is performed for lift-off. Afterwards, a 100 nm Ni layer is e-beam evaporated in row j) which is used as a DBR dry-etching mask. Fencing is not an issue here because, on the one hand, it does not occur at this thickness and on the other hand, this is the last layer, and nothing is deposited on top which might be affected. In row k), lift-off is performed in the same manner as in fig. 4.3 h).

In the final set of processing steps fig. 4.5, the MEMS-DBR filter processing finishes. Row l) shows the dry-etching according to recipe in section 3.1.3 split in 10 min steps while the profile of a certain device is measured to determine the current etch speed, which varies from 100 nm/min to 150 nm/min. After each

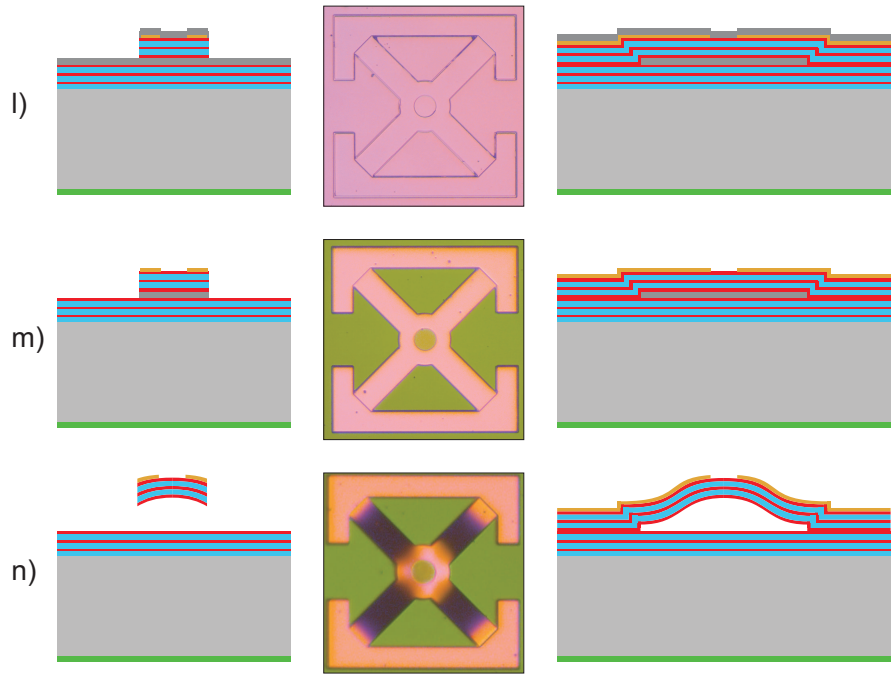

Figure 4.5: DBR dry-etching and MEMS under-etching (wet) with released MEMS-DBR. **l)** Dry-etching of exposed DBR until Ni sacrificial layer is visible. ARC deposition on the backside. **m)** Removing visible Ni, MEMS etch mask and exposed sacrificial layer. **n)** Under-etching of MEMS releases MEMS-DBR. Critical-point-drying to remove the liquid in the cavity.

etching, the sample is rinsed with water for 1 min to remove the accumulated dust on the surface before measuring step heights. This process is repeated 2 or 3 times until the etch-rate drops noticeably. At this point, the exposed sacrificial layer Ni shows the same color as the Ni etch-mask on top, see fig. 4.5 l). During this process, the sample needs to be glued with wax to a glass plate for protection of the backside from the radicals. Additionally, the sample is flipped at this point to deposit a SiN_y ARC on the backside. This moment is chosen because the samples are glued on and off glass holder several times during processing or fastened on a metal holder for evaporation steps. If the ARC was deposited either before or after the bottom-DBR deposition during step a), the ARC stays exposed to all these treatments and is ultimately damaged. A crystalline Si surface is much more resilient to these kinds of manual or chemical exposures. At this point, the most important part of the front side - the aperture - is still covered by a Ni etch mask and is protected when fixing the sample upside down on a wafer for the ARC PECVD deposition. Next, both the etch

mask and the exposed sacrificial layer are etched with the solution already used in step d). Afterwards, the sacrificial layer below top-DBR is removed. This is done with the same solution as before but without rotation at this point. The etching is much faster without rotation. As described in appendix A, Ni-etching is a two-step process. The exposed area of the Ni sacrificial layer is tiny due to its thickness of 400 nm and a constant movement of the etchant reduces the contact time drastically. In the case of large-area etchings shown before, rotation is beneficial for etching speed. Depending on the resulting MEMS bending, under-etching takes about 40 min to 80 min to be visible. Samples are then kept for another 40 min to 80 min in the solution without stirring to ensure complete removal of Ni from both sides of the resonator - bottom-DBR and inside of top-DBR.

After the etching of Ni, depending on MEMS bending, samples can be dried with two methods, both not presented in fig. 4.5. If the bending extended MEMS-DBR by at least 10 µm, they are kept in isopropanol for 10 min to replace the water below MEMS. Afterwards, they are dried on a hot plate set to 60 °C. If the bending is not as large, capillary forces pull the MEMS towards the wafer during drying in air, and both DBRs would stick together. Once this happens, it is impossible to release the MEMS a second time, and the samples are useless. Critical-point-drying solves this issue. Here, first water is replaced by isopropanol as well, but then isopropanol is replaced by liquid CO_2 in a sealed chamber. Increasing the temperature above 35 °C raises the pressure above 80 bar to move around the critical point of CO_2 in a phase-diagram. Above it, liquid and gas have the same density, and the phase-change disappears. Afterwards, pressure can be released and only gaseous CO_2 is present within the cavity without any capillary forces. The MEMS-DBR is released and ready for transmission experiments.

4.1.2 Alternative Sacrificial Layer - Photoresist

The previous section presented the processing steps with a Ni sacrificial layer involving lengthy etching steps (80 min to 160 min). Now, Ni is replaced by PR to reduce processing time and steps. First, the requirements for a sacrificial layer are discussed, followed by a closer look at Ni and PR as sacrificial layers.

Important properties for a sacrificial layer are

- selectively solvable (can be removed without influence on other layers),

- and smooth surface (surface-roughness below 5 nm).

Solubility is important to release the MEMS-structure. The solvent should be selective towards sacrificial layer material and should not attack the other layers like dielectric DBRs, Cr/Au or Ti/Au electrodes, or Si substrate in case of filter. When processing VCSELs later (section 5.2), additionally, semiconductor material InP and high-dielectric constant material BCB are exposed, which require further attention. Here two materials Ni and PR are investigated as both fulfil these requirements.

Nickel

Previous works investigated Ni well [21, 52]. Both depositions described in section 2.5 are tested while e-beam evaporation proves to be more reliable as it can be entirely removed from the sample which is crucial both in case of the sacrificial layer and etch mask. Roughness (around 3 nm for dielectrics) and shape of the underlying layer are reproduced. A step of either filter bottom-electrode or the n-type semiconductor laser-eye are repeated. This step can be up to 500 nm for a half-VCSEL. It never influenced resonator stability, though, as the beam waist at the MEMS-DBR is much smaller than the aperture diameter. The removal of Ni sacrificial can be done with a diluted HNO_3 solution at 50 °C which takes about 2-4 h, depending on layer thickness. The thickness of a Ni sacrificial layer is adjustable by deposition time, so there are no limits as to how thin or thick it can be grown. Note that it should not be too thin (less than 300 nm) as the etching-time is increased drastically due to a much smaller exposed surface. Either a lift-off or an etching photolithography-step can be used to structure Ni (compare section 2.5). When using lift-off, the occurrence of fencing depends on the layer thickness. When Ni is used as an etch mask ($\approx$ 100 nm) to structure MEMS shape, this is not important. However, when a thicker layer ($\approx$ 400 nm) is required for the sacrificial layer, fencing reaches a height of up to 1 µm. This is not acceptable because the top-DBR grows on top. Having a 1 µm wall at the edges of the sacrificial layer might increase the probability of the MEMS to break drastically. Conclusively, etching photolithography was used to structure the sacrificial layer, although it involves an additional processing step.

Photoresist

Using PR as a sacrificial layer is a novel approach for MEMS-DBR in this work to reduce the complexity of the processing. The surface roughness of a PR is not an issue as it is in a liquid phase when being shaped and if anything, reduces the surface roughness of the underlying layers. This behavior is also visible when any steps occur. They are smoothed out due to the viscosity of the PR. It also might be beneficial to the long-term stability of the MEMS-structure since there are no harsh steps in the beams where they usually break when introducing external forces (e.g. a needle). An organic PR can be easily removed through acetone which is generally used to clean samples from PR after etching steps. The removal of a PR sacrificial layer finished within a few minutes ($< 2\,\text{min}$). Additionally, an O_2 plasma can be used to dry-etch the PR, which is even more impressive as no liquids are involved, and critical-point-drying steps are avoided. The possible thickness of a PR sacrificial layer is constrained to the available PR viscosity, which defines the layer thickness after spin-coating. To a certain degree, the thickness can be adjusted with rotation-speed during spin-coating but is still confined to a range of $\pm 20\,\%$ around the nominal value given by the manufacturer. A PR sacrificial layer only needs one photolithography step. As there are steps after sacrificial layer structuring, like Cr/Au evaporation and DBR deposition that involve temperatures above room temperature and UV radiation, the PR needs to be able to sustain these conditions. It both needs to survive these steps (no cracks should form), and it needs to be removable again (no excessive hardening). A -PR (maN1407) fulfils both conditions. It does not crack (+PR like AZ1505 cracks during Cr/Au evaporation), and it can be removed in the end by acetone. Unfortunately, an O_2-plasma does not remove the PR below the MEMS, which cannot get rid of the wet-chemical etching to remove the sacrificial layer. Table 4.2 summarizes the described properties for both Ni and PR sacrificial layers.

Sample Overview and Processing Peculiarities

For this investigation, two samples (N and P) are processed in parallel while the only difference is the sacrificial layer (N with Nickel and P with PR). DBR depositions are done for both samples simultaneously to keep these layers as constant as possible. In both cases, the target thickness of the sacrificial layer is 400 nm. For Ni this is realized through a sputtering time of 13 min, resulting in a thickness of $d_{\text{sac}} = 432\,\text{nm}$. Sample P is spin-coated at 6000 rpm with -PR (maN1407) resulting in a thickness of $d_{\text{sac}} = 412\,\text{nm}$.

Table 4.2: Properties of two sacrificial layers - Ni and negative PR.

material	roughness	thickness	removal	complexity
Nickel	+ reproduces layer below	+ flexible through sputtering time	- lengthy etching	- additional etching
Photoresist	+ smooths layer below	0 constrained by available sources	+ fast and easy	+ only photo lithography

MEMS-DBR for sample N releases after 45 min in HNO_3 (50 °C) while it takes another hour to remove the Ni sacrificial layer in the cavity completely. As soon as the bending is visible, the sample does not undergo critical-point-drying. Instead it is put in isopropanol for 1 h and then dried on a hot-plate (60 °C) for several minutes. The MEMS-DBR does not stick to fixed DBR surface, thus stays released.

The MEMS-DBR for sample P is released after 2 min in acetone at room temperature. Afterwards they are put in isopropanol for 1 h and dried on a hot-plate (60 °C) just like sample N. The resulting cross-sections of the released MEMS-DBR are shown in the fig. 4.6. With this data, both air-gap L_{air} and radius of curvature ρ can be obtained (see also table 4.3).

Table 4.3: Air-gap and radius of curvature for Ni (N) and PR (P) sacrificial layers with thickness d_{sac}.

sample	d_{sac}	L_{air}	ρ
N	432 nm	9.9 µm	1.54 mm
P	412 nm	8.8 µm	1.10 mm

Table 4.3 shows a difference in L_{air} of about 10 % which results in a change in ρ, although the thickness of the sacrificial layers is nearly identical. To explain this behavior, one must look at the processes during the DBR deposition. The layer grows by adsorption and chemical reaction at a specific temperature on the surface of the sample. Here lies the difference. While radicals meet Ni on sample N, the immediate surface on which the dielectrics grow for sample P is PR. So different materials with varying properties are present. As described in section 2.5, different lattice constants cause defects in the layer grown. So

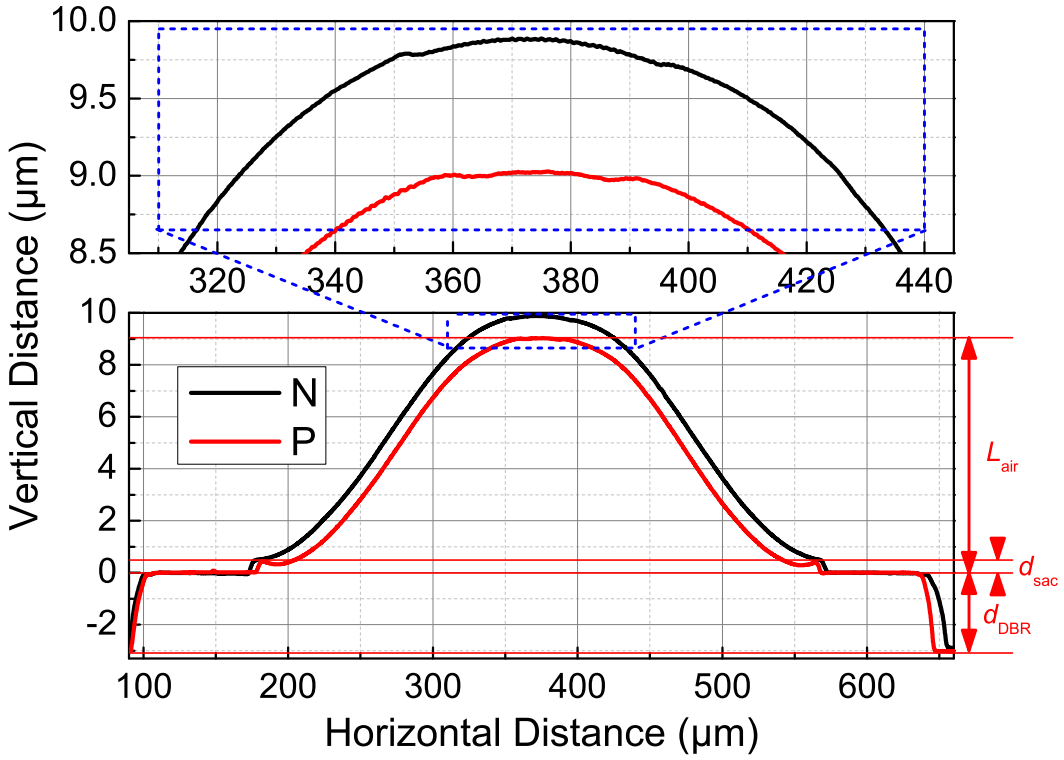

Figure 4.6: Top: Zoomed span of blue dashed box to determine radius of curvature ρ within the two steps identifying the aperture of Cr/Au top-electrode. Here $\rho_N = 1.5\,\text{mm}$ and $\rho_P = 1.1\,\text{mm}$.
Bottom: MEMS-DBR cross-section of sample with Ni sacrificial layer (N) and PR sacrificial layer (P) taken with a profiler. On the right side, air-gap L_{air}, thickness of sacrificial layer d_{sac} and thickness of bottom-DBR d_{DBR} are shown. Here $L_{air,N} = 9.9\,\mu\text{m}$ and $L_{air,P} = 8.8\,\mu\text{m}$.

here, different defects are obtained, pinholes and interstitial atoms within the dielectrics, which result in different effective stresses within the layers, although both samples are in the PECVD chamber simultaneously. Different stresses create different bendings of the released MEMS-DBR. Although both Ni and PR are amorphous, which have no lattice constants, different surfaces are assumed to have a similar effect. Thus layer stress within MEMS-DBR grown on Nickel is larger than within MEMS-DBR grown on PR. It is also possible that the dielectric Youngs's Modulus E_{SiC_z} and E_{SiO_x} are slightly different in both depositions. Please also note a difference in the profile step created by the sacrificial layer, seen at 200 µm and 550 µm. Sample N shows a flat step. Sample P first shows

a downward bending before it rises towards the center. This effect might be caused by differences in sidewall coverage during DBR deposition. Maybe the dielectric material has adhesion problems at the PR sidewalls, and they are thinner in the end. Thinner walls might cause such a shape because they are less sturdy and the MEMS-weight pushes the arms downwards.

Further Requirements

As seen in the in-depth analysis of Ni and PR, it is generally more comfortable and less complex to use PR. This holds when processing MEMS-DBR tunable filters on a Si-substrate. However, occasionally adhesion problems of a PR sacrificial layer on SiO_x-SiC_z bottom-DBR occur. Structures moved on the sample surface after development. The exact reason could not be pinpointed, but possibly different environmental influences like temperature and humidity change the behavior of the PR and cannot be predicted. This uncertainty is always present when working with PR. So from this standpoint, although a PR sacrificial layer does show some advantages towards metal, it is much less reliable. Looking at photodiodes and VCSELs, it is evident that a metal sacrificial layer is the only way to go ahead.

First, the PD processing requirements are described. More details on processing are shown in section 5.1 but the general problem is already listed here. A MEMS-DBR tunable PD is a MEMS-DBR tunable filter grown on top of a photodiode with wide spectral responsivity. The difference between processing on a Si-substrate and a PD are the electrical contacts of the PD itself. The back contact is on the backside of the wafer and does not pose a problem. The front contact is on the front where light enters the semiconductor. Processing the filter as depicted in section 4.1.1, the front contacts are covered by the bottom-DBR and cannot be accessed. To access them, the bottom-DBR must be etched as well by adjusting the sacrificial layer mask and adding a metal contact protection layer below the bottom-DBR. Now, when etching through top-DBR a PR sacrificial layer will be removed as well, so no problem here. However, since the DBR etching is only halfway done, the edges of PR sacrificial layer are exposed to dielectric etching plasma for another 30 min during which time two things can happen. The first possibility is that the sacrificial layer dissolves and the MEMS-DBR releases since the DBR etching recipe contains more than oxygen, which by itself is not enough to remove a PR sacrificial layer, as shown previously. If the MEMS bends upwards at this point, dry-etching radicals can enter the cavity attacking the highly reflective surface within the resonator, damaging it. The

second possibility is the opposite. Etching residuals can deposit on the tiny PR sacrificial layer cross-section which seals the layer off from later application of acetone to release the MEMS. Ultimately the MEMS-DBR cannot be released. For MEMS-DBR tunable filters grown on a Si-substrate, this does not pose an immediate problem as sacrificial layer exposure to dry-etching radicals is kept at a minimum by thoroughly observing etch-rate and -depth to stop on time. For this, it is required to know the actual top-DBR thickness, which generally does not represent the targeted thickness but is a few per cent thinner. It is best to include a dummy sample for these kinds of testing, processed in parallel.

Processing a MEMS-DBR VCSEL poses a more immediate problem. Half-VCSELs, as received, cannot come in contact with acetone because it damages the electrical contact between the mesa and Au pads. So generally samples cannot be cleaned with acetone, but for example with NMP (N-Methyl-2-pyrrolidone) which is as potent as acetone and can even be used at elevated temperatures in contrast to acetone to increase etch rate. NMP, unfortunately, is deemed biologically questionable [50] and should be used as little as possible. So, releasing a MEMS might prove difficult without NMP. Moreover, it is fatal if dry-etching continues too long and the VCSEL contacts (both on the front side of the sample) are damaged. Certainly, other etchants might be suitable in further studies, but since half-VCSEL sample numbers are limited, such testing is abandoned. To summarize, table 4.2 is extended by PD and VCSEL restrictions. With this, 0 represents neither negative nor positive behavior but raises the necessity for heightened attention during processing.

Table 4.4: Final properties of two sacrificial layers - Ni and negative PR.

	roughness	thickness	complexity	removal	Filter	PD	VCSEL
Ni	+	+	-	-	+	+	+
PR	+	0	+	+	0	0	0

4.1.3 Setup and Alignment to Characterize Tunable Filters

A broadband fiber-coupled light source is suitable to characterize a tunable filter. In this case, a semiconductor optical amplifier (SOA) with a spontaneous emission range of 1450 nm to 1700 nm is employed. Figure 4.8 shows its spectrum in black with a maximum at 1550 nm. The optical spectrum analyzer (OSA) sensitivity limits the lower wavelength end, while the OSA range cuts off the

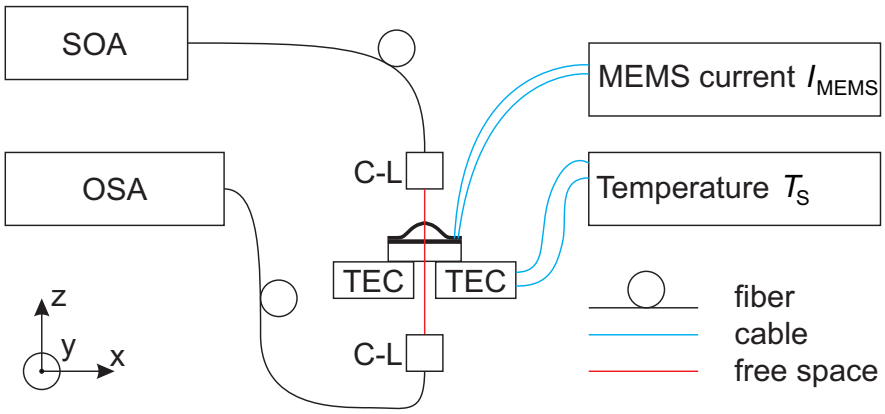

Figure 4.7: Transmission setup for filter characterization containing a temperature and MEMS-current controller, a broadband light source (SOA) and a detector (OSA). Light is coupled between single-mode fiber and filter with collimator-lens systems (C-L). Temperature is stabilized with a TEC.

other end. A model of the setup is shown in fig. 4.7. The wafer with structured filters lies on a Peltier module (TEC) to control and stabilize the substrate temperature T_S. A hole in the sample table gives access to the backside. The MEMS top-electrode is contacted with two needles on opposite sides to ensure a current flow I_{MEMS} through the MEMS-arms and -disc. Above and below the filter mounted collimator-lens systems couple light from a single-mode fiber into the MEMS-aperture ($R_{aperture} = 25\,\mu m$) and couple the filtered light from the backside into a second single-mode fiber. In the end, an optical spectrum analyzer (OSA) characterizes the filtered spectrum.

Alignment of the collimator-lens system towards the filter both in x-y-z as well as in angular direction is essential for a good side mode suppression ratio (SMSR) of the filtered spectrum. Within the cavity, many standing modes are possible simultaneously which differ in wavelength, as seen in eq. (2.29). The best SMSR occurs if the lens axis is perpendicular to the MEMS-DBR surface. Since the MEMS-DBR is bent, this requirement can only be met in the center. Thus misalignment in x-y directions can excite unwanted modes, or several modes simultaneously (several p,$l \neq 0$,0) because the incident wave-front is not perpendicular to the mirror surface. The same behavior happens if the device is tilted towards the lens systems.

To prepare the setup, both lenses should be aligned towards each other without the device under test. First, a rough mechanical estimation is done, and subsequently, the coupling efficiency is maximized from one lens to the other.

For this, the same SOA source is used, and the received power is measured in the second fiber. Here, both the position and angle of the upper lens are tuned to maximize the received power. This way, losses decrease to $\approx 3\,\mathrm{dB}$. Losses cannot be eliminated as coupling efficiencies between single-mode fiber and collimator-lens system, and vice versa are always below 100 %. With this setup, the reference measurements for a non-filtered spectrum are recorded. Ideally, focal points of both lenses now coincide at the same z-position, and the axes are parallel.

Next, the substrate containing the filter devices is set in the free space light beam. To characterize the desired unit, either a Hg-vapor lamp or a red laser - both fiber-coupled - is used as a source. It is important not to change the lens distance at this point to focus the visible light spot as the lens focal length is wavelength-dependent. After the visible light hits the desired MEMS aperture, the SOA source can be attached again. To find the filtered signal, it is advised to maximize MEMS-DBR reflection. It is highest when the beam incides perpendicularly on the MEMS-DBR. Hitting the Au MEMS-electrode instead of the DBR can show high reflection as well, but lower than the DBR itself. It is necessary to increase the distance between the upper lens and the device as the upper focal point now needs to hit the MEMS-DBR surface, which is above the focal point of the lower lens. Now, the filtered signal is visible. To improve the overall alignment, a back and forth between maximizing reflection and minimizing transmitted side-mode suppression ratio (SMSR) is required. It is crucial at this point not to alter the x-y and angle settings between both lenses to keep their axes aligned. Only the device position, angles and z-position of the upper lens should be optimized.

Before looking at the filtered results in the following chapter, it is necessary to mention, that a perfect alignment where only the fundamental mode is visible in the transmission is virtually impossible as many effects occur at the same time. The most important are the x-y-z and angle alignments, as mentioned above. But additionally, the beam-width needs to be perfect. The combination of collimator and lens defines the beam-width (> 0) at the focal point. This width needs to be matched to the FPR mode-width, depending on MEMS-DBR curvature and cavity-length. Inserting values of a plane-concave resonator ($g_1 = 1$, $g_2 = 1 - L_{\mathrm{air}}/\rho_2$) into eq. (2.27), a beam-width w_2 at the MEMS-DBR of

$$w_2 = \sqrt{\frac{\lambda L_{\mathrm{air}}}{\pi}\sqrt{\frac{1}{1-(L_{\mathrm{air}}/\rho_2)^2}}} \tag{4.1}$$

is obtained. Only certain combinations and thus beam-widths are available, so it is best to choose the closest one. Even if the perfect combination were available, the values are not constant. Most important is the wavelength. Focal lengths for lenses only apply for a value of 1550 nm. For widely tunable devices the wavelength is not constant. Moreover, ρ_2 is not constant due to the tuning mechanism. Increasing I_{MEMS} extends the MEMS-DBR, which reduces ρ_2 slightly. At the same time, the distance between MEMS-DBR and lens shortens. As investigated in section 3.4, a MEMS-DBR displacement of several µm is expected. The influence of L_{air} on w_2 is much larger than the influence of ρ.

Then again, assuming coupling was perfect, a different collimator-lens system was used for each wavelength, and the entire setup realigned for each I_{MEMS}, there is still the factor of processing. As described in section 4.1.1, processing requires several photolithography steps. Both the electrode mask and the MEMS etch mask need to be aligned to the sacrificial layer. Moreover, the sacrificial layer needs to be aligned to the photodiode or VCSEL aperture. In each alignment, errors can occur. In the best case, alignment-errors are below 1 µm, but generally not zero. They reduce cavity stability because the center of concave MEMS-DBR and fixed DBR are not parallel anymore. In the worst case, a tilt of MEMS-DBR destroys stability entirely.

For all measurements, a collimator-lens system creating a beam-width of 13.5 µm is used because it fits best to all cavities investigated in this work.

4.1.4 Transmission Characterization

This section analyzes the transmission spectrum of a SiO_x-SiC_z-based FPR. The setup is shown in fig. 4.7. The light source is a broadband semiconductor optical amplifier (SOA), while an optical spectrum analyzer (OSA) records the transmission. Figure 4.8 presents both reference SOA and filtered spectrum.

Figure 4.8 shows three main peaks at 1468.1 nm, 1573.0 nm and 1693.0 nm, respectively. These represent consecutive longitudinal modes of order $m+1$, m and $m-1$. As shown in fig. 2.1, the distance between consecutive modes is not constant. With higher orders they become more closely spaced in the wavelength regime. Equation (2.13) determines m. L_{air} is the same, since all

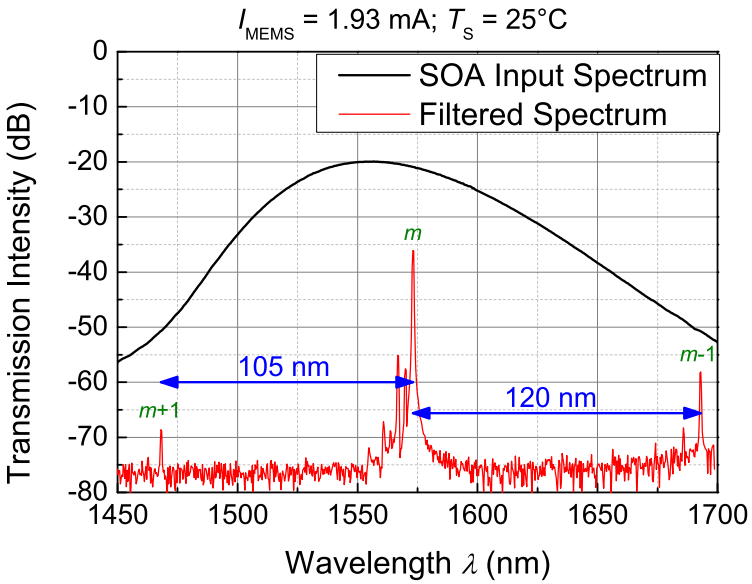

Figure 4.8: SOA input spectrum and SiO_x-SiC_z MEMS-DBR filter transmission spectrum.

peaks are visible simultaneously.

$$L_{m+1} = L_m = L_{m-1} \tag{4.2}$$

$$\Rightarrow \quad \frac{(m+1)\lambda_{m+1}}{2} = \frac{m\lambda_m}{2} = \frac{(m-1)\lambda_{m-1}}{2} \tag{4.3}$$

Solving for m with either next or previous mode, results in

$$\frac{(m+1)\lambda_{m+1}}{2} = \frac{m\lambda_m}{2} \qquad \frac{m\lambda_m}{2} = \frac{(m-1)\lambda_{m-1}}{2} \tag{4.4}$$

$$m = \frac{\lambda_{m+1}}{\lambda_m - \lambda_{m+1}} \qquad m = \frac{\lambda_{m-1}}{\lambda_{m-1} - \lambda_m} \tag{4.5}$$

$$= 13.98 \qquad = 14.10 \tag{4.6}$$

Thus, the central mode order corresponds to $m = 14$, because $m \in \mathbb{N}_{>0}$. The discrepancy between both values is assumed to stem from measurement error resulting from non-instantaneous detection of the spectra. An OSA is sweeping from low to high wavelengths which needs a certain amount of time. During data acquisition of such a large wavelength range, the MEMS might have drifted which induced a slight wavelength-shift. Moreover, the FSR in the

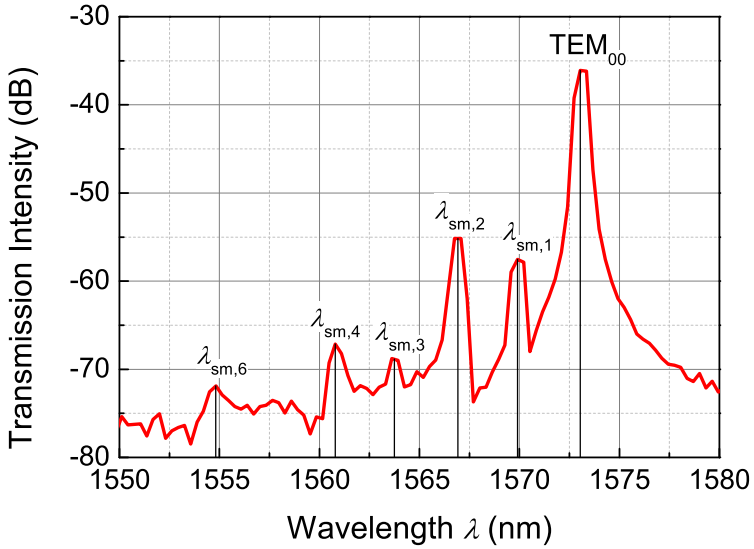

Figure 4.9: Enlarged central peak from fig. 4.8 with identified mode orders.

frequency regime, where modes are equidistant, provides values of 13.62 THz and 13.51 THz, respectively.

Consequently, the mode order can be determined approximately by rounding to the next integer after applying the following equation:

$$m \approx \frac{\lambda_{m+1}}{FSR_{m+1}}, \tag{4.7}$$

where FSR_{m+1} is the distance between the peak of interest and its lower-wavelength neighbor. $m = 14$ means, there are 14 anti-nodes within the cavity along its axis. Now, the cavity-length can be roughly estimated with the wavelength of the central mode because it is close to the designed DBR center-wavelength 1550 nm with

$$L_m = m\frac{\lambda_m}{2} \tag{4.8}$$

$$\Rightarrow \quad L_{14} = 11\,011\,\text{nm}, \tag{4.9}$$

which is slightly larger than the measured physical cavity-length of $L_{\text{air,measured}} = 10.27\,\mu\text{m}$. The reason for this is, as before, non-linear tuning efficiency.

Table 4.5: Wavelengths of side-modes with possible TEM identification for $(2p + l)$ solutions.

$\lambda_{\mathrm{sm,i}}$ (nm)	$(2p + l)$	Order possibilites TEM_{pl}
1573.0	0	TEM_{00}
1569.9	1	TEM_{01}
1566.8	2	TEM_{02}, TEM_{10}
1563.8	3	TEM_{03}, TEM_{11}
1560.8	4	TEM_{04}, TEM_{12}, TEM_{20}
1554.8	6	TEM_{06}, TEM_{14}, TEM_{22}, TEM_{30}

Next, side-modes should be identified. As presented in eq. (2.29), they always have a blue-shift towards the fundamental mode TEM_{00}.

$$\lambda_{m,pl} = \frac{2L}{m + \frac{2p+l}{\pi} \arccos \sqrt{g_1 g_2}}. \tag{4.10}$$

Here, m defines the number of standing wave nodes along the resonator axis, as before, while p and l represent the number of radial and azimuthal nodes, respectively. Considering resonator stability with $L = 10.27\,\mu\mathrm{m}$, $\rho_{\mathrm{fixed}} \to \infty$ and $\rho_{\mathrm{MEMS}} = 1.2\,\mathrm{mm}$,

$$g_1 = g_{\mathrm{fixed}} = 1 - \frac{L}{\rho_{\mathrm{fixed}}} \to 1 - \frac{L}{\infty} \to 1 \tag{4.11}$$

$$g_2 = g_{\mathrm{MEMS}} = 1 - \frac{L}{\rho_{\mathrm{MEMS}}} = 1 - \frac{10.27\,\mu\mathrm{m}}{1.2\,\mathrm{mm}} \approx 0.991. \tag{4.12}$$

Thus, the factor

$$\frac{\arccos \sqrt{g_1 g_2}}{\pi} \approx 3.02 \cdot 10^{-2} \tag{4.13}$$

results in the following equation

$$\lambda_{14,pl} = \frac{2L_{14}}{14 + (2p + l) \cdot 3.02 \cdot 10^{-2}}. \tag{4.14}$$

Figure 4.9 delivers wavelengths $\lambda_{\mathrm{sm,1\text{-}5}}$ for side-modes 1 to 5. Corresponding modes can be identified with eq. (4.14) by inserting integer values for p and l. From the third side-mode, ambiguity starts to play a role, because a value of

$2p + l = 2$ can be found with two combinations, either ($p = 1$ and $l = 0$) or ($p = 0$ and $l = 2$). Table 4.5 summarizes all possible combinations. Note that they are equidistant with a spacing of approximately 3 nm. This means that there should be another transmission peak around 1557.8 nm but it is probably not visible due to alignment of the filter in the measurement setup.

4.1.5 Tuning with MEMS Electrode Current

This section investigates the tuning capabilities of a MEMS-DBR filter. The setup from fig. 4.7 is used here as well. However, instead of looking at only one MEMS current, it varies within a certain range. Most filters processed in this work use electro-thermal tuning. I_{MEMS} flows through the metal electrode on top of the DBR. Electrical resistance R_{MEMS} generates heat which extends the MEMS-DBR and increases cavity-length L_{air}. Depending on the Au-electrode thickness, the electrical resistance varies. A thicker layer offers a larger cross-section and thus reduces electrical resistance R_{MEMS}. The chosen thickness of 60 nm creates a value of $R_{\mathrm{MEMS}} = 10\,\Omega$. A larger resistance generates more heat which extends the MEMS-DBR further. But it is more prone to burn at lower currents (see also fig. 4.20). Moreover, if the thickness is too thin, it is not possible to tune through the entire FSR before permanent damage of the electrode occurs.

Figure 4.10 presents the tuned transmission spectra. With higher I_{MEMS} a red-shift of the transmission peak follows. A FSR of 110 nm is larger compared to fig. 4.8 between modes 14 and 15. At first glance, this contradicts the expectation as the cavity-length extends due to the higher I_{MEMS}. A larger cavity-length decreases the FSR in general. Nonetheless, taking a look at eq. (2.16), the wavelength itself has a stronger influence - squared instead of the inverse. Thus, with increasing of L_{air}, resonant wavelength λ_{14} also increases but has a stronger influence on the FSR. FSR is larger in fig. 4.10 than in fig. 4.8 while observing the same two modes. Figure 4.14 demonstrates that the FSR is not constant at all. To be correct when mentioning the FSR, both the cavity-length and longitudinal mode need to be defined. So for the sake of simplicity, the free spectral ranges mentioned in this work, are defined as the distance between two consecutive modes while the higher-order is located at the lower wavelength end of the targeted tuning range. Thus, if anything, the tuning range of that mode is slightly larger than the FSR. When looking at a VCSEL, this rule does not apply. During stimulated emission, generally, only one mode prevails and suppresses the others depending on gain and mirror reflectivities. In that case, the next higher-order mode might have a stronger amplification. Due to the reduced

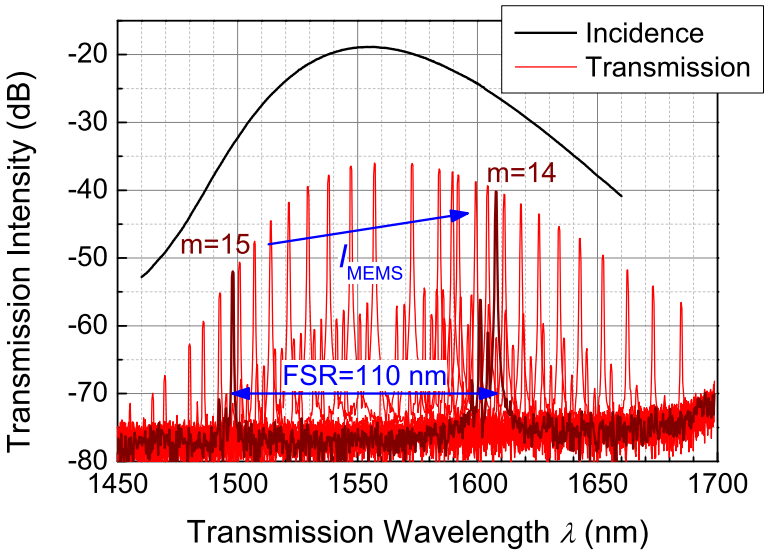

Figure 4.10: SiO_x-SiC_z-DBR filter, tuned with $I_M = 26.6\,mA$ to $80\,mA$, results in a red-shift of transmitted spectrum. Incident broadband SOA spectrum is presented in black. The entire FSR of 110 nm in mode $m = 15$ can be used. Due to the broadband source, up to three consecutive modes can be seen simultaneously, compare fig. 4.8.

FSR for higher orders, tuning range actually might be smaller than the FSR. SMSR is 21 dB until 1570 nm and drops to about 15 dB for larger wavelengths because the second side-mode grows stronger than the first. Possibly a tilted MEMS-DBR causes this behavior. The tilt worsens if the MEMS-DBR expands unevenly due to asymmetries caused by photolithography misalignment. Note that a comparable SiO_x-SiN_y MEMS-DBR filter, presented in table 4.6, shows a SMSR of 10 dB to 14 dB.

An increase of I_{MEMS} induces a red-shift. This process is continuous. There are no fixed positions of the MEMS or I_{MEMS}. In fig. 4.10 discrete current values help to enhance visualization. The black line shows the reference spectrum of the SOA taken with the same setup without a filter in the free-space part of the beam-path. Section 4.1.3 explains further measurement details. Intensity differences between incidence and transmission come from coupling-, cavity- and material-losses. The free-space-collimator-lens (CL) causes coupling losses, which are already included in the reference measurement. Filter coupling-losses include coupling efficiency from CL-system into the MEMS aperture and from

the plane backside into the second CL-system. In both cases, proper alignment is essential, as described in section 4.1.3. Moreover, processing issues induce cavity-losses, either by misalignment of photolithography masks or insufficient etching of either sacrificial layer or DBR etch mask. Figure 2.1 predicts that even small losses within the cavity reduce the transmission immensely for high reflectivities. Furthermore, the light within the cavity passes these losses during each round trip. Both etched layers comprise of a thin Ni film, $\approx 400\,\mathrm{nm}$ and $100\,\mathrm{nm}$. A diluted HNO_3 solution removes both layers. Ni deposition can be performed by both e-beam and Ar-beam sputtering. For Ar-beam sputtering, it is impossible to remove the layer entirely. Generally, a residual film with a thickness in the nm-range remains. One possibility for this is a contamination of the Ni target or the vacuum chamber itself. The contamination cannot be removed by HNO_3. E-beam sputtering is applied here. With this, this effect might also be present because there are three visible e-beam spots on the target. Possibly there is a larger number of weaker beams that cannot be seen with the human eye. Those might hit areas around the Ni-target. The target-crucible itself is made out of tungsten which has a much higher evaporation temperature than Ni and can, thus, be excluded. However, there might be residues on top of those crucibles which are released during evaporation.

Lastly, SiC_z does have absorption in NIR, detected by reflection measurements of single layers in section 3.1. This probably creates the largest loss for light passing through the filter. In total, the light passes twelve SiC_z layers on a single trip. However, the high reflectivity of a DBR is based on multiple internal reflections. So the number of passages through each layer is much higher than 1. The total filter losses are $\approx 17\,\mathrm{dB}$.

Lambert-Beer's law allows for a simplified calculation of transmission losses through two SiO_x-SiC_z-DBRs on a single trip. Hereby, an ellipsometry measurement in fig. 3.1 determines the extinction coefficient of $k = 0.014$. Subsequently, the absorption coefficient α_{SiC_z} is [66]

$$\alpha_{SiC_z} = k\frac{\omega}{c_0} = k\frac{2\pi}{\lambda} = 567\,\mathrm{cm}^{-1}, \tag{4.15}$$

for $\lambda = 1550\,\mathrm{nm}$. This value is comparable with results published in [11]. Fixed DBR and MEMS-DBR consist of thirteen layers of SiC_z in total, giving a thickness of $d_{SiC_z} = 2056\,\mathrm{nm}$ and an absorption of

$$E_t = E_i\, e^{-\alpha_{SiC_z} d_{SiC_z}} = 0.89 \cdot E_i \tag{4.16}$$

where E_t and E_i are the transmitted and incident fields, respectively. A single transit corresponds to a power loss of 1 dB, while multiple passages, due to reflections at each interface inside the DBRs, contribute an even more considerable amount.

4.1.6 Tuning with Substrate Temperature

Wavelength tuning depends on the change of the cavity-length. Section 4.1.5 shows the MEMS-DBR temperature-change through I_{MEMS}. However, this effect can be achieved through adjusting substrate temperature T_S as well. In that case, the entire device heats up. The Si bulk material governs the substrate heat expansion (thermal expansion coefficient $\alpha_{Si} = 2.6\,K^{-1}$). The MEMS expands in an upward direction due to its bending.

Figure 4.11 shows the transmission wavelength dependent on T_S for a SiO_x-SiC_z MEMS-DBR filter in red. A reference temperature of 15 °C corresponds to the temperature-shift of zero. The current limit of the TEC defines the highest temperature of 65 °C. A differential temperature coefficient of $\Delta\lambda_{SiC_z} = 1.02\,nm/K$ can be extracted. For each Kelvin in temperature-change, the wavelength

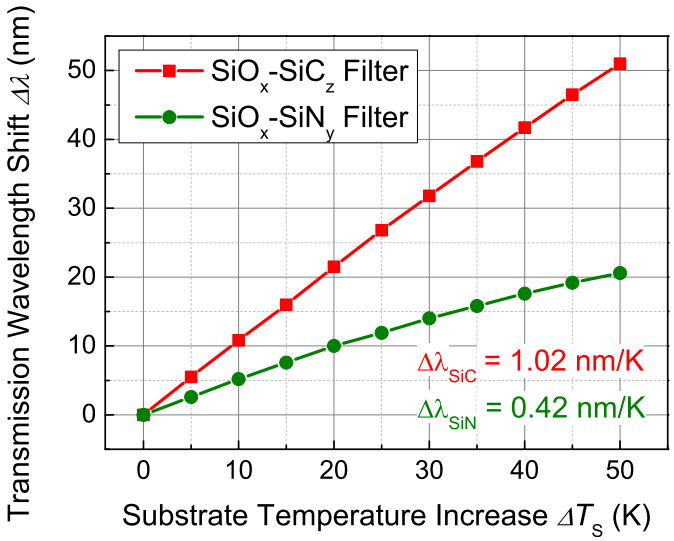

Figure 4.11: Wavelength red-shift due to substrate temperature increase from $T_S = 15$ °C for a SiO_x-SiC_z and SiO_x-SiN_y MEMS-DBR filter with comparable air-gaps, see table 4.6.

Table 4.6: Two filters are processed with the goal to create similar cavity-lengths. The table lists the properties of SiO_x-SiN_y and SiO_x-SiC_z MEMS-DBRs.

	SiO_x-SiN_y	SiO_x-SiC_z
M	11.5	6.5
σ_{SiO_x}	$-130\,\mathrm{MPa}$	$-110\,\mathrm{MPa}$
σ_{SiN_y}	$-240\,\mathrm{MPa}$	-
σ_{SiC_z}	-	$-150\,\mathrm{MPa}$
L_{air}	9.8 µm	10.3 µm

shifts one nanometer. This emphasizes the importance of a stable temperature-controlling and ideally a proper packaging for the device to shield it from environmental influences. Two filters are processed to create similar cavity-lengths and reflectivities to compare the material-dependent temperature behavior of SiC_z- and SiN_y-based MEMS-DBR filter. Table 4.6 summarizes the requirements. The resulting air-gaps of 9.9 µm and 8.8 µm are close enough to compare filtering properties of both material systems.

According to fig. 4.11, temperature-influence on a SiN_y-based MEMS-DBR is smaller by about a factor of 2. While the red dots show a linear dependence, the olive dots show a slight non-linearity after $\Delta T_S = 20\,\mathrm{K}$. In the range of 0 K to 20 K the slope is 0.5 nm/K. Reasons for this can be found in the thermal expansion coefficients ($\alpha_{SiC} = 4.3 \cdot 10^{-6}\,\mathrm{K}^{-1}$, $\alpha_{SiO} = 0.5 \cdot 10^{-6}\,\mathrm{K}^{-1}$ and $\alpha_{SiN} = 2.3 \cdot 10^{-6}\,\mathrm{K}^{-1}$). Since $\alpha_{SiC_z} > \alpha_{SiN_y}$ and α_{SiO_x} is the same for both, SiC_z-based MEMS-DBR is bound to expand further when experiencing the same temperature change.

4.1.7 Transmission Linewidth

This section investigates the transmission linewidth of both SiO_x-SiN_y and SiO_x-SiC_z MEMS-DBR FPRs. According to eq. (2.18), high mirror reflectivities, low cavity losses, and short cavities cause a narrow transmission linewidth. Equation (4.17) shows a linear proportionality between the linewidth and the FSR. Thus there is always a trade-off between wide tunability and narrow filtering. In the end, the application defines the requirements of either extensive

tuning or very narrow filtering. The processing is adjusted accordingly.

$$\delta\lambda = \left|\ln\left(\sqrt{R_1 R_2}V\right)\right| \frac{FSR}{\pi} \tag{4.17}$$

fig. 4.12 shows the 3-dB linewidth across the tuning range. Here values are normalized to

$$\frac{\delta\lambda}{\lambda} = \left|\ln\left(\sqrt{R_1 R_2}V\right)\right| \frac{\lambda}{2\pi L}. \tag{4.18}$$

Figure 4.12 shows the transmission linewidths for a SiO_x-SiC_z and SiO_x-SiN_y MEMS-DBR filter in red and olive, respectively. The SiN_y-based filter has a narrower linewidth than SiC_z-based, although the same maximum reflectivity is expected according to fig. 3.6. table 4.6 lists the details for each DBR. The number of layer pairs is chosen to have a similar maximum DBR reflectivity. But apparently, the simulations are too ideal, and the actual SiO_x-SiC_z-DBR reflectivity is reduced, see also fig. B.1. The SiN_y-DBR transmission linewidth shows a U-shape with a $\delta\lambda$-minimum at the designed center-wavelength of 1550 nm. It broadens towards the edges of the tuning range. For the SiC_z-DBR filter transmission linewidth, there are two minima at 1550 nm and 1600 nm. It can be explained by a thickness shift of either top- or bottom-DBR. Possibly during deposition of either DBR, the deposition rate was higher than assumed both for SiO_x and SiC_z. Thicker layers cause a red-shift of the center-wavelength. Conclusively, maximum reflectivities of bottom- and top-DBR are not at the same position. Moreover, the slopes of SiC_z in fig. 4.12 are smaller, representing a broader reflectivity stopband. It is not much broader than SiN_y graph due to the wavelength-shift of one DBR. Both DBRs require a high reflectivity for a narrow transmission linewidth. If one of them is lossy in a certain range, light leaves the resonator, and the high reflectivity of the other mirror cannot contribute.

In fig. 4.13 SiO_x-SiN_y MEMS-DBR filter has a much higher finesse due to its narrow linewidth. However, looking at the behavior off-center, there is a much steeper drop for SiO_x-SiN_y MEMS-DBR FPR. SiO_x-SiC_z MEMS-DBR filter has a lower but more constant finesse. A graphic demonstration of the cavity Q-factor would show the same behavior and is, thus, omitted at this point.

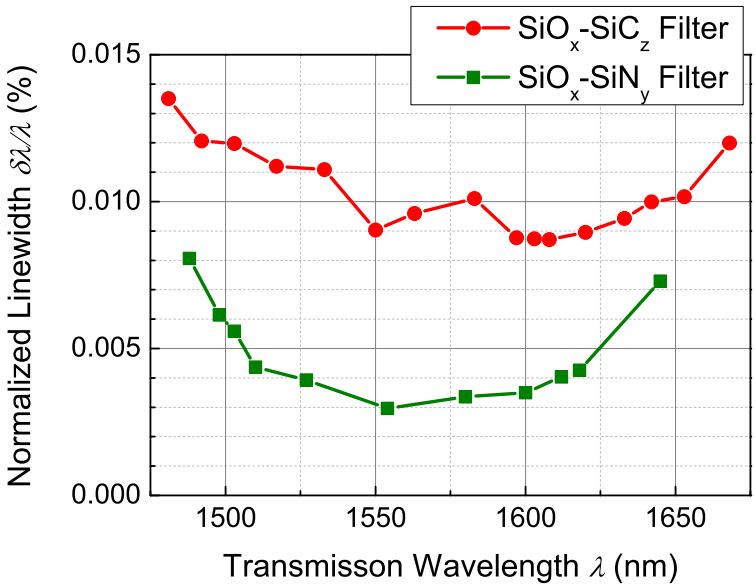

Figure 4.12: Normalized transmission linewidth $\delta\lambda$ over wavelength for tunable SiO_x-SiC_z and SiO_x-SiN_y MEMS-DBR filters.

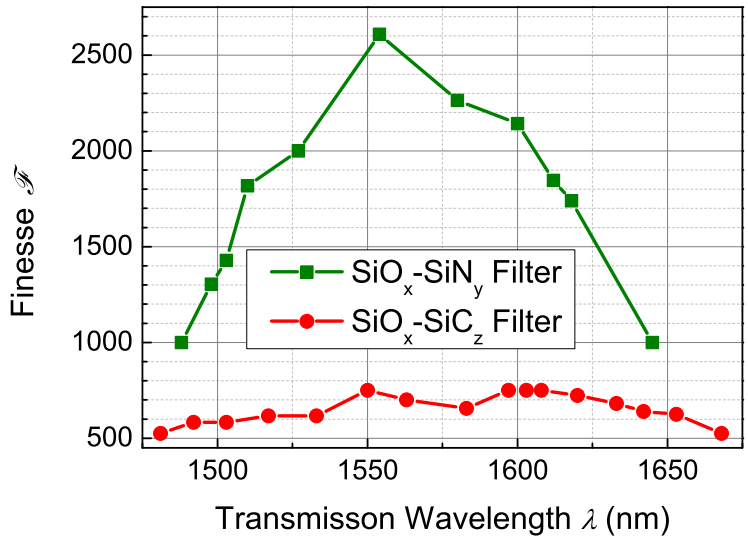

Figure 4.13: Finesse $\mathcal{F}$ for SiO_x-SiN_y and SiO_x-SiC_z MEMS-DBR filters assuming $FSR_{SiN_y} = 120\,\text{nm}$ and $FSR_{SiC_z} = 105\,\text{nm}$.

4.1.8 Requirements for Larger Tuning Ranges

Previous sections show that the advantages of a SiO_x-SiC_z DBR in comparison to a SiO_x-SiN_y DBR are not of significance, yet. The tuning range is not larger although SiO_x-SiC_z DBR offers a much broader reflectivity stopband (compare fig. 3.7). Simulations show the tuning limitations because of FSR for both SiO_x-SiN_y DBR and SiO_x-SiC_z DBR. The FSR can be determined with two methods. The first method is based on previously employed assumptions of a linear tuning efficiency. Hereby, a single interface mirror at the depth L_{eff} [30] describes the reflection at a DBR with an effective penetration depth L_{eff} at which intensity drops to $1/e$.

$$L_{eff} = \frac{\lambda_0}{4\Delta n} \cdot \tanh\left(2\Delta n \frac{L_{DBR}}{\lambda_0}\right) \approx \frac{\lambda_0}{4\Delta n}. \tag{4.19}$$

Thus, cavity-length $L_{linear} = L_{air} + 2L_{eff}$ consists of the air-gap and two material specific penetration depths according to eq. (4.19) because of two DBR mirrors. To calculate the FSR, eq. (2.16) ($FSR = \lambda^2/(2L)$) with a center-wavelength of $\lambda = 1550\,\text{nm}$ is used (lines).

The second, new, method is based on non-linear tuning efficiency, described in section 3.4. It uses the transfer matrix method to calculate the transmission of a MEMS-DBR filter with two plane DBRs and an air-gap of L_{air} (points).

As expected, the FSR decreases with larger values of L_{air}. A shorter cavity is beneficial for a large tuning range. The difference between both curves in method one stems from L_{eff}, where $L_{eff,SiC_z} < L_{eff,SiN_y}$. Moreover, L_{eff} is responsible for both lines cutting y-axis at 700 nm and 1581 nm, respectively. If both mirrors are pushed very close together ($L_{air} \to 0$) cavity-length will never reach zero due to L_{eff}. For each material system, a lower limit of $2L_{eff}$ for the cavity-length exists. The difference between the simplified view (lines) and more accurate TMM is negligible for larger values of L_{air} while being important for small cavity-lengths. For a SiO_x-SiC_z MEMS-DBR, the difference between both methods is minimal. In this case, the penetration depth into the DBR estimates the displacement of the resonant wavelength node inside the FPR DBR. For small cavity-lengths, the error when applying effective penetration depth is stronger and should not be used.

In the lower part of the graph, two patterned areas are visible. They show the ranges where mirror reflectivities are at least 99.5 %. This is the material-based limit for the tuning range of 120 nm and 330 nm, for SiO_x-SiN_y and SiO_x-SiC_z DBRs with 6.5 and 11.5 layer pairs, respectively. Using this insight and

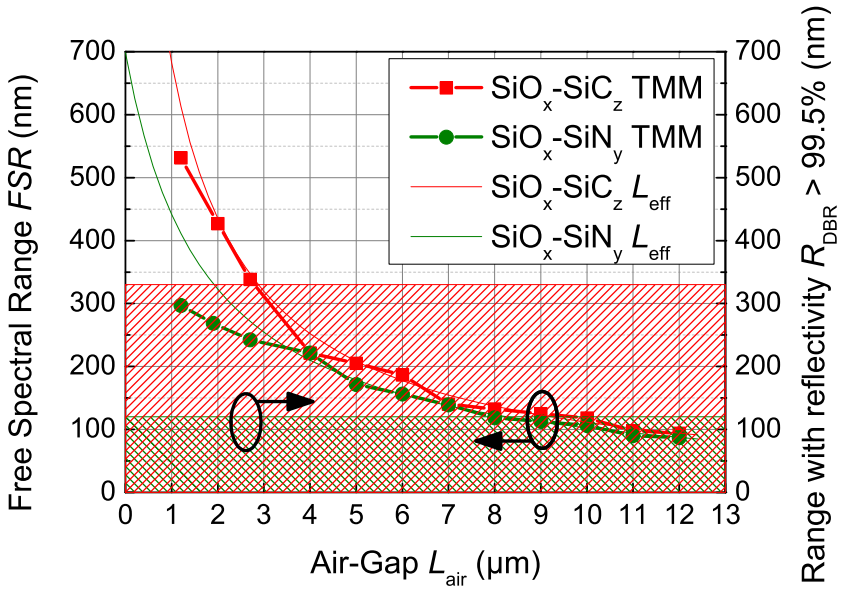

Figure 4.14: Points: TMM calculated FSR for varying air-gap. FSR surrounding center-wavelength 1550 nm was chosen for each point. Steps represent mode hops. **Lines**: Calculated FSR considering L_{eff} depending on air-gap for SiO_x-SiC_z and SiO_x-SiN_y DBR filters. The difference between both lines is determined by different L_{eff}. **Patterned areas**: Range where $R_{\text{DBR}} > 99.5\,\%$.

comparing it to SiO_x-SiC_z DBR and SiO_x-SiN_y DBR tuning ranges it is evident that SiO_x-SiN_y MEMS-DBR is limited by material reflectivity stopband while SiO_x-SiC_z MEMS-DBR is limited by the large air-gap of $\approx 10\,\mu m$. Conclusively, to extend the tuning range of the SiO_x-SiC_z MEMS-DBR filter, a reduction of L_{air} is unavoidable.

4.2 Modeling

In this section, a Comsol Multiphysics[1] model is created to simulate SiO_x-SiC_z MEMS-DBR bending. This tool reduces the amount of experimental testing by predicting MEMS-DBR bending depending on layer stress, material properties and geometries.

[1] Version 4.1.0.88

4.2.1 Create a Model Describing Experimental Findings

A model for SiO_x-SiC_z-MEMS-DBR incorporates three physics models, solid mechanics to describe MEMS bending, electric currents to model electro-thermal heating and heat transfer to include electric and ambient heating. Especially material parameters for SiC_z are essential as literature offers a wide range of specific constants. The most important parameter for the DBR bending is the Young's Modulus E_{SiC_z}. [18] reports a range for E_{SiC_z} of 88 GPa to 247 GPa depending on the ratio z between Si and C atoms. While [65] even measures a very low range of 20 GPa to 36 GPa for $z < 0.5$ when depositing SiC_z at 320 °C. [78] reports that E_{SiC_z} is subject to drastic changes when going from crystalline to amorphous structure. In the present case, the deposition takes place at only 80 °C, which is very low for a PECVD deposition. Consequently, the deposited layers are highly amorphous. ν_{SiC_z} is around 0.25. For SiO_x many references state a value of $E_{SiO_x} = 70$ GPa. This parameter remains constant.

Under the assumption of a constant layer-stress during a DBR deposition, a sweep of E_{SiC_z} in the simulation compares the modelled and measured initial air-gaps after a MEMES release. Depending on the shape, layer-stress of the top Au-electrode influences the MEMS-bending as well. Evaporations of both Cr/Au and Ti/Au create tensile values of $\sigma_{Cr/Au} = 330$ MPa and $\sigma_{Ti/Au} = 30$ MPa, respectively. Although layer stress differs one order of magnitude, the influence on the MEMS-bending is very small because the electrodes are much thinner than the DBR (70 nm and 3 µm). More important is the layer shape. It is essential to include an opening in the center - representing the aperture - otherwise, metal layer stress influence increases a lot. fig. 4.15 left displays the top-view of the created shape. Figure 4.15 shows an extruded shape with an extremely fine mesh on the right - only the finest available automatic mesh results in a released MEMS. For the sake of simplicity, the model only includes a Si substrate and the MEMS-DBR with an electrode on top. Bottom fixed-DBR does not change the result significantly because it is much thinner than the substrate but increases calculation time. It is neglected as well in this model. Layer-stress in bottom-DBR should not influence MEMS-DBR bending much because they are already relaxed at the time when the top-DBR is deposited. Another big difference between a processed sample and the model is the thickness of the sacrificial layer. While it inherently creates a step from the fixed DBR to MEMS-DBR areas, this is omitted in the model to decrease complexity when creating three-dimensional objects. Substrate thickness, tested in two steps, 300 µm (actual thickness) and 50 µm (less computation time) only showed a diminutive influence as well. Thus, substrate thickness remains at 50 µm.

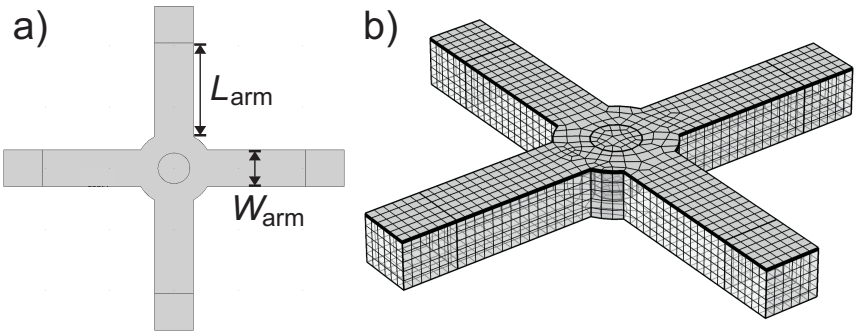

Figure 4.15: Left: Top-view of shapes created for Comsol modelling. Four squares represent the fixed top-DBR, the cross-shape describes the MEMS and the circle in the center is the metallization aperture. **Right**: Extremely fine meshed three-dimensional structures.

Moreover, the structure encompasses only one device, while on an actual sample hundreds of devices are aligned in a two-dimensional array. This influence is described by introducing a roller boundary at the ends of the substrate arms because at this position two MEMS-DBRs push or pull in opposite directions cancelling the effect of a layer-stress. External temperature applies to the bottom of the substrate as T_S while the top and the MEMS-DBR experience ambient temperature of 20 °C. A current through the MEMS-arms increases the temperature at the top electrode due to joule-heating. The heat then is transferred to the MEMS-DBR, ultimately extending the air-gap. Parameters for Young's Modulus, temperature, MEMS-current and sizes facilitate changing of material properties and MEMS-sizes. Initial MEMS bending is calculated by using a flat MEMS-DBR (see fig. 4.15 right) and defining a contact-area between bottom-most DBR-layer and substrate surface. The layer stress in the plane DBR deforms the MEMS and creates a bending, see fig. 4.17.

Values from 20 GPa to 100 GPa simulate the resulting air-gap $L_{air,simulated}$ to determine E_{SiC_z}. The MEMS-DBR comprises 6.5 layer pairs of SiC_z and SiO_x with a thickness of 194 nm and 276 nm (see section 4.1.1), and layer stresses of −150 MPa and −110 MPa, respectively. Moreover, a Cr/Au has a thickness of 70 nm without discriminating between Cr and Au in the model. The result is presented in fig. 4.16. Measuring MEMS bending with a surface profiler (needle force 3 mg) results in an $L_{air,Dektak} = 10.52\,\mu m$. Measuring the same sample contact-less with a confocal microscope shows an increase of 0.1 µm or approximately 1 % which can, generally, be neglected due to processing variations between each device even on the same substrate. Both measurements

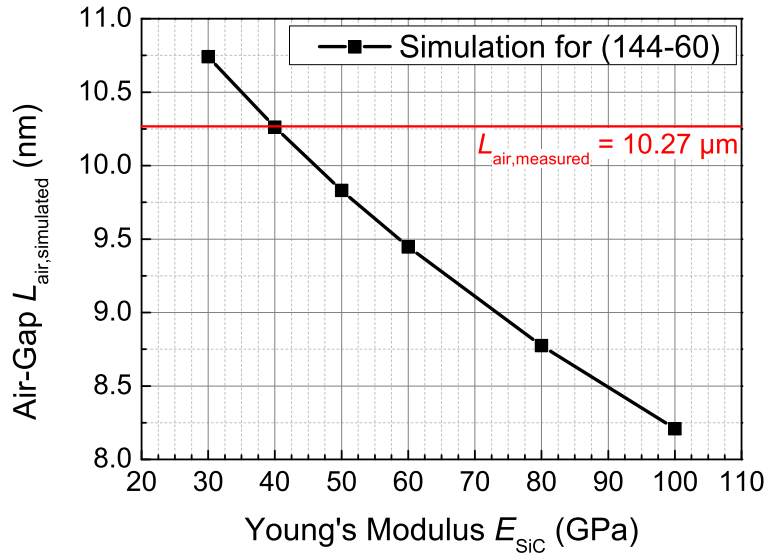

Figure 4.16: Simulated air-gaps depending on Young's Modulus E_{SiC_z} for a MEMS-DBR with $L = 145\,\mu m$ and $W = 60\,\mu m$. Measured air-gap of $L_{air,measured} = 10.27\,\mu m$ is acquired for $E_{SiC} = 40\,GPa$.

include a sacrificial layer thickness of 350 nm which has to be subtracted to match the simulated value. To determine E_{SiC_z} accurately with Comsol, a measured air-gap of $L_{air,measured} = 10.27\,\mu m$ needs to be found, representing air-gap measurement utilizing a confocal microscope subtracted by the sacrificial layer thickness.

Figure 4.16 shows a reduction of the air-gap with larger values for E_{SiC_z}. Thus, $R_{SiC_z} = 40\,GPa$ creates an air-gap of 10.27 µm. Figure 4.17 presents the deformation for $E_{SiC_z} = 40\,GPa$.

Beyond simulating MEMS-deformation, it is possible to add an eigenfrequency solver to the model which returns MEMS mechanical resonances. Modulating the MEMS at these frequencies would result in catastrophic failure of the structure, ultimately breaking it. Thus, the first eigenfrequency (1^{st} EF) limits the wavelength tuning-speed of the structure. Figure 4.18 shows the first six EF and its oscillating shapes. Note that the first two EFs are very close to each other showing similar oscillation shapes. This small offset stems from the asymmetry of meshing, see fig. 4.15 right, and cannot be avoided. Asymmetries do always occur in a processed sample due to misalignment of photolithography

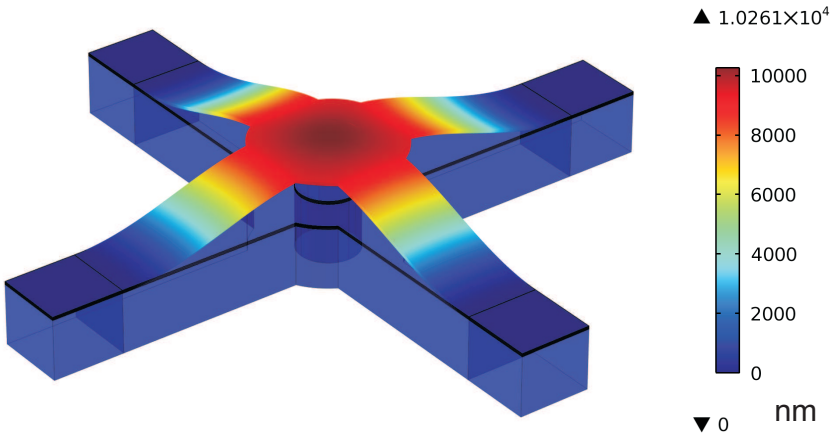

Figure 4.17: Simulated total displacement for $L = 145\,\mu m$, $W = 60\,\mu m$ and $E_{SiC_z} = 40\,GPa$. Here, the thickness of the sacrificial layer is omitted. MEMS bending here is exaggerated by a factor of 4 to emphasize the resulting shape.

masks, so this effect represents the real sample well. Depending on which EF is regarded, positions and number of oscillation anti-nodes vary. If the solution shows imaginary solutions for the EFs, more than 6 EFs should be calculated because the first 6 describe translations of the entire structure and should be omitted.

Conclusively, Comsol simulations do show a realistic result but have deviations from the real sample. Among others, these include a sacrificial layer, misalignment during photolithography, thickness variation of DBR layers during deposition, and simplified shape of fixed DBR areas. Conclusively, simulations are beneficial to see a general direction when changing specific parameters like layer-stress and MEMS-size.

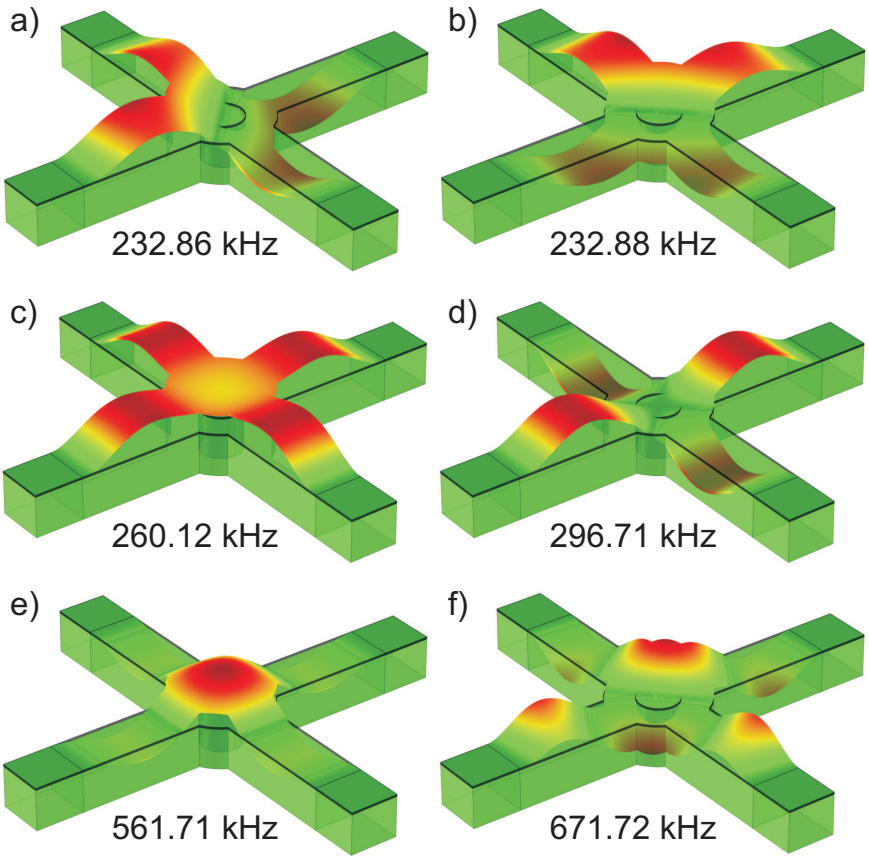

Figure 4.18: First 6 EF of a 144-60 MEMS-DBR structure with corresponding eigenmodes. Red is high deformation and green is no deformation. 1st EF limits the MEMS-DBR tuning speed.

4.2.2 Reduction of Cavity Length

This section investigates the reduction of the cavity-length to increase the tuning-range of a SiO_x-SiC_z DBR filter. An initial air-gap of 2 µm to 5 µm is supposed to create an FSR of 300 nm according to fig. 4.14. Several concepts look promising. The layer stress of the single layers is mainly responsible for the MEMS-DBR bending and the air-gap. So the straightforward solution is to reduce compressive layer-stress of SiC_z and SiO_x layers. Unfortunately in case of SiO_x layer-stress is very stable at approximately -120 MPa within usable deposition parameter ranges. For SiC_z layer-stress can be adjusted, but only towards higher values, see figs. 3.3 to 3.5. Previous depositions already applied the lowest possible value of -150 MPa. Comsol simulations identified two different methods

to reduce cavity-length. The first increases the number of layer-pairs, while the second solution reduces MEMS beam-width and -length. Furthermore, two strategies following changes during deposition and treatment afterwards are discussed independently of Comsol investigations.

Number of layer-pairs

The initial model uses a DBR with 6.5 layer-pairs. Two additional simulations with 7.5 and 8.5 layer pairs result in a reduction of the initial air-gap and a small increase in EF. The results are summarized in table 4.7. Although influence is visible, its effectiveness is minimal.

Table 4.7: Resulting air-gaps and 1st EF for different numbers of layer-pairs for a SiC_z-SiO_x DBR.

M	$L_{air,simulated}$ (µm)	1st EF (kHz)
6.5	10.27	233
7.5	9.92	254
8.5	9.74	275

Reduction of Geometry Sizes

The second findings from Comsol simulations are a reduction of air-gap by reducing length L_{arm} and width W_{arm} of the MEMS-arms. The target air-gaps lie in the range of 2 µm to 5 µm to investigate the region where reflectivity stopband of the DBRs and the cavity-length-dependent FSR coincide, see fig. 4.14. This way maximum tuning range of roughly 300 nm can be used. Reduction of beam length and width by at least a factor of 2 is required. Thus a set of 3 lengths and widths are identified to create small-sized MEMS. Aperture diameter remains unchanged at $R_{aperture} = 25\,\mu m$ to have the same opening for fiber-coupling. Disc diameter $R_{disc,small} = 40\,\mu m$ is reduced to fit the disc between the fixed MEMS parts. The resulting air-gaps are presented in table 4.8. Figure 4.19 presents the simulated structures for all combinations. Additionally the result from fig. 4.17 is shown again to emphasize the reduction of MEMS-size.

Table 4.8: Simulated initial air-gaps without sacrificial layer for each size-combination of small-sized MEMS-DBR.

L_{arm} (µm) \ W_{arm} (µm)	20 (µm)	25 (µm)	30 (µm)
30	0.85	1.18	1.44
45	2.54	2.74	2.93
60	3.77	3.94	4.07

Table 4.9: Calculated 1st EF for each size-combination of small-sized MEMS-DBR.

L_{arm} (µm) \ W_{arm} (µm)	20 (kHz)	25 (kHz)	30 (kHz)
30	334	403	482
45	445	514	577
60	472	521	562

I_{MEMS} flows from 2 fixed DBR parts (top and right square from fig. 4.15 left) to the other 2 fixed DBR parts (left and bottom square from fig. 4.15 right). Electrical resistance increases heat along the electrode. Most heat is generated at the narrowest position located at the ring around the aperture. To demonstrate this, a MEMS-DBR electrode is burnt with $I_{MEMS} = 100\,mA$. The outcome shows burn marks at the aperture ring where current flows from top to bottom contact, see fig. 4.20 a). Simulating the structure for the same current shows the highest temperature at the same position, see fig. 4.20 b). For size combination (45-20) air-gap rose from 2.54 µm to 3.15 µm due to MEMS heating.

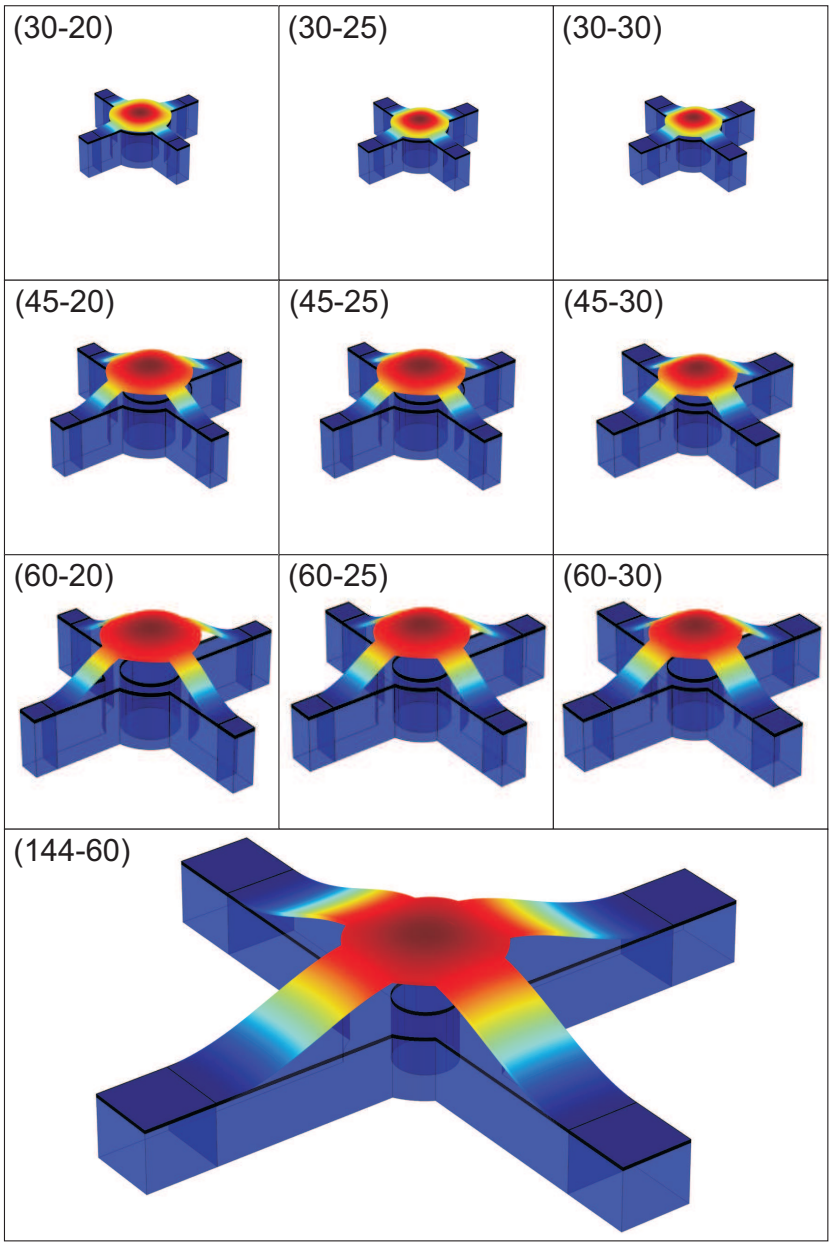

Figure 4.19: Nine combinations for MEMS-DBR size reductions in length and width. MEMS arm widths and lengths are given in parentheses (L-W). A displacement scaling factor of 10 for each deformation is chosen to emphasize all MEMS displacements. For size comparison, the model from fig. 4.17 with a displacement scaling factor of 5 is presented in the bottom.

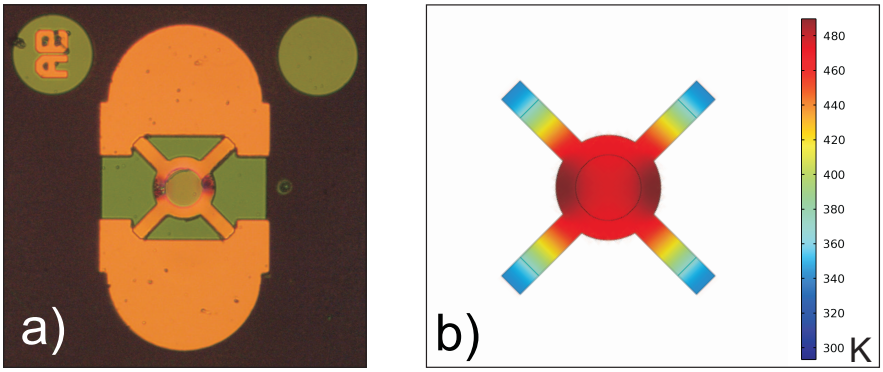

Figure 4.20: A MEMS current of $I_{\mathrm{MEMS}} = 100\,\mathrm{mA}$ is applied to a) a finished sample, burning the electrode. b) a Comsol simulation to present position of highest temperature rise of $\Delta T \approx 200\,\mathrm{K}$. The displayed legend encompasses 293 K to 490 K. Ambient and substrate temperature are set to 293 K. Both positions match.

Multi-Layer Deposition

[79] reports on replacing a layer deposition with thickness d by n thinner layer depositions which results in much lower layer stress. Two test depositions are performed for a total deposition time of 15 min to reproduce this behavior. The first layer is deposited in one go, while for the second, five 3 min steps with pumping and purging steps in between are performed. The resulting layer-stress did not change quantifiably.

Temperature Treatment of Released MEMS-DBR

All dielectrics in this work are deposited with a PECVD at 80 °C which is low in comparison to CVD processes going above 800 °C. The resulting layer structure is not crystalline but amorphous. This means, next to silicon and carbon or oxygen atoms, hydrogen is present created as a waste product from SiH_4. To release those impostors and offer the remaining bonds a chance to relax elevated temperatures are required [1]. To test the temperature effect on a MEMS-DBR, only devices containing a SiO_x-SiC_z MEMS-DBR on a SiC_z layer, deposited on a Si substrate are processed without bottom-DBR or metallization. The wafer is broken in four pieces to test four temperatures. Air-gap before the treatment is 10.4 µm. Each sample is tempered with an RTA (rapid temperature annealing) at elevated temperatures T_{T} from 150 °C to 450 °C in a nitrogen

Table 4.10: Change in SiO_x-SiC_z MEMS-DBR air-gap induced by 5 min tempering at T_T.

T_T (°C)	L_{air} (µm)
0	10.4
150	11.9
250	14.9
350	broken
450	detached

atmosphere. Temperature is sustained for 5 min. The heating ramp is set to 20 s while cooling back to room-temperature takes about 10 min. The resulting air-gaps are summarized in table 4.10.

The effect of tempering a released MEMS-DBR creates an even larger air-gap by increasing layer stress of both SiO_x and SiC_z layers. With an increase from 10 µm to almost 15 µm at 250 °C the change is quite large. For higher temperatures the MEMS-DBR brakes. At 350 °C, the connection between movable MEMS and fixed DBR is destroyed. For 450 °C, the whole MEMS-DBR structure detaches in some areas from the substrate.

4.3 Optimizations

In this section results for SiO_x-SiC_z MEMS-DBR produced with small-sized masks are presented. Processing is not shown in detail, for some insight in size on a device, processing of a tunable VCSEL in section 5.2 can be viewed. Although the steps differ from a filter, the masks are the same. Newly developed mask design for MEMS-etching is presented in fig. 4.21.

4.3.1 Adjusted Mask Design

New masks are created according to adjustments in a Comsol model presented in section 4.2.2. At the same time, the factor of 2 represents an investigation, whether the number of devices on one wafer in mass-production down the line, can be increased as well. The footprint of the mask size is 420 µm × 420 µm with

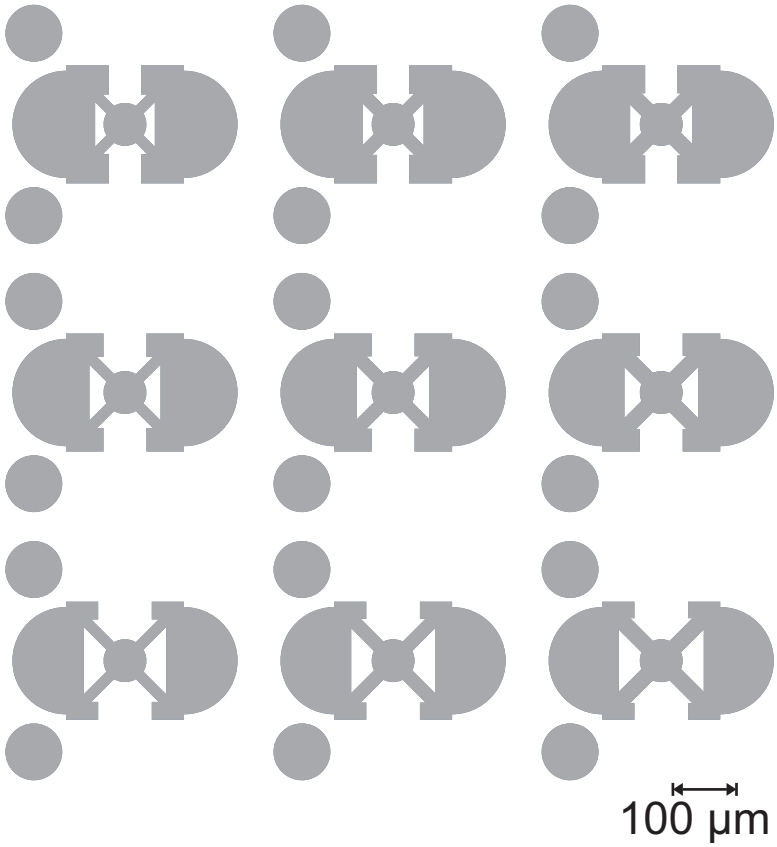

Figure 4.21: MEMS-etch mask for small sizes. Lengths and widths correspond to arrangement in table 4.11 where MEMS arm width increases rightwards and length downwards. Half discs at the left and right side of each devices offers larger contacting pads. Two circles at each device are required to cover numbering created with top electrode Au. Masks for further processing steps can be found in appendix C.

a pitch of 500 µm. The new design targets a pitch of 250 µm which reduces device footprint to 220 µm × 220 µm. The pitch is kept at 500 µm to be compatible with the half-VCSEL layout. The additional space between devices acquired this way is used to increase the MEMS top-electrode area for easier contacting with the probing needles. Moreover, an indexing grid identifies each device. Length and width are varied in 3 steps each, resulting in 9 different combinations. The disc radius decreases to $R_{\text{disc}} = 40\,\mu\text{m}$ to prevent it from touching the fixed DBR areas. The aperture size remains unchanged at $R_{\text{aperture}} = 25\,\mu\text{m}$.

The resulting initial air-gaps are measured with a surface profiler (needle

Table 4.11: Measured initial air-gaps of SiO_x-SiC_z MEMS-DBR filters for small sizes.

L_{arm} (µm) \ W_{arm} (µm)	20 (nm)	25 (nm)	30 (nm)
30	1100	1620	1910
45	3140	3320	3480
60	4320	4440	4640

force 3 mg) and are summarized in table 4.11. Comparing these with Comsol-predicted values from table 4.8 by adding sacrificial layer thickness of 400 nm, shows reasonable matching. It means further refinement in material parameters of the simulation is necessary or adding a bottom-DBR after all. The biggest difference between model and reality is the step in MEMS-DBR caused by the sacrificial layer thickness. If this is taken into account in the simulation as well, a better prediction might be possible. However, using the developed Comsol model for a close estimation of the resulting air-gap is definitively useful and possible.

In table 4.12 radii of curvature ρ for each size combination are presented. ρ behave in the opposite way of L_{air}. Smaller air-gaps are flatter. Thus, the curvature is larger, corresponding to larger values of ρ. Remembering stability condition eq. (2.22) and eq. (2.21), all of them are stable resonators because all MEMS-DBR mirrors are concavely bent and $L_{air} < \rho$. With eq. (2.27) the radii of TEM_{00} modes for each size can be determined. All w_i lie in the range of 5 µm to 6.2 µm which is not much smaller than the value for (144-60) sized MEMS at 7.8 µm ($L_{airgap} = 10\,\mu m$ and $\rho = 1.52\,mm$). These values hold with small deviations for both beam-widths at the flat fixed DBR and bent MEMS-DBR. Thus, for all filters, the same collimator-lens system with a diameter of the focus point of 13.5 µm is used. Other combinations of available collimators and lenses create a much larger or smaller beam waist.

Tuning with MEMS Current

Each size combination is tested individually with the tuning results presented in fig. 4.22. Each one is tunable over its entire FSR. Because the air-gaps are very low, see table 4.11, for most devices, FSR is larger than SOA source spectral width and thus cannot be determined directly. Each device recalls the spectral

Table 4.12: Measured radii of curvature in the eyes of SiO_x-SiC_z MEMS-DBR filters for small sizes.

L_{arm} (µm) \ W_{arm} (µm)	20 (mm)	25 (mm)	30 (mm)
30	5.52	1.57	1.05
45	1.13	0.95	0.83
60	1.08	0.90	0.82

shape of the SOA source (see fig. 4.10) in its transmission. A more detailed look at a single spectrum is given in fig. 4.23.

Single Spectra around 1550 nm

Each small-sized SiO_x-SiC_z MEMS-DBR resonator is tuned with I_{MEMS} to 1550 nm to compare the transmission capabilities. The transmission spectra are presented in fig. 4.23. Each device is aligned individually. In general, the SMSR of all devices is much worse compared to fig. 4.8, for example. For filter (30-20) and (60-25) in graphs a) and h) it was not possible to align in a way to have the highest intensity in the fundamental mode TEM_{00}. For this reason, a negative SMSR is used for those two devices as the side-mode is stronger than the fundamental mode. Devices with arm length 45 µm (graphs d)-f)) show the best SMSR of approximately 13 dB, summarized in table 4.13. These spectra emphasize again the importance of accurate alignment of photolithography masks to increase the SMSR of the transmission. Because a misalignment can cause the MEMS-DBR to be tilted, reducing resonator stability. The alignment-error for small-sized MEMS-DBR masks towards the sacrificial layer should be below 1 µm.

Table 4.13: SMSR taken from graphs in fig. 4.23.

L_{arm} (µm) \ W_{arm} (µm)	20 (dB)	25 (dB)	30 (dB)
30	-4	5.7	2.54
45	13.25	12.83	12.72
60	10.03	-1.83	6.66

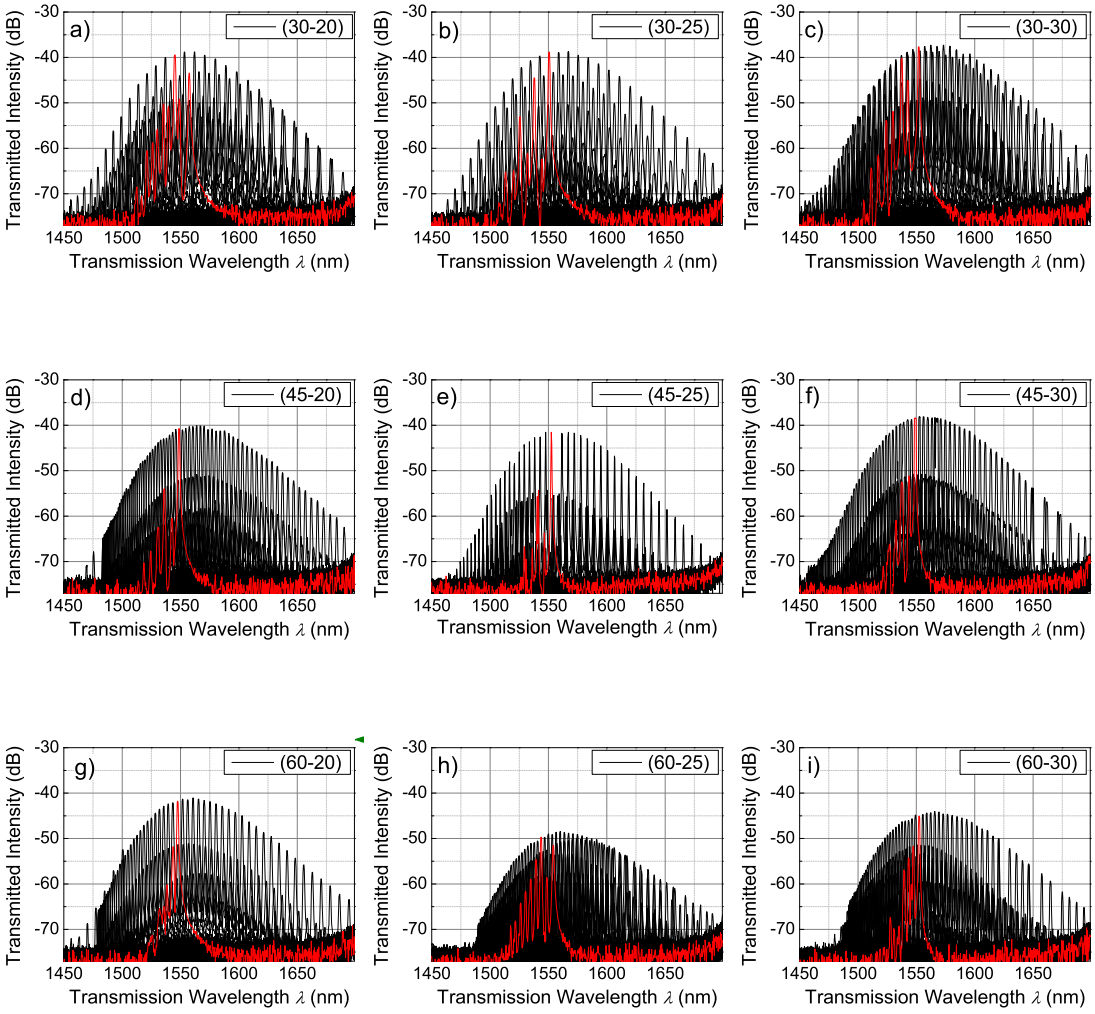

Figure 4.22: Transmission spectra of wavelength-tuned small-sized SiO_x-SiC_z MEMS-DBR filters for sizes ($L_{arm} - W_{arm}$). Higher I_{MEMS} causes a red-shift.

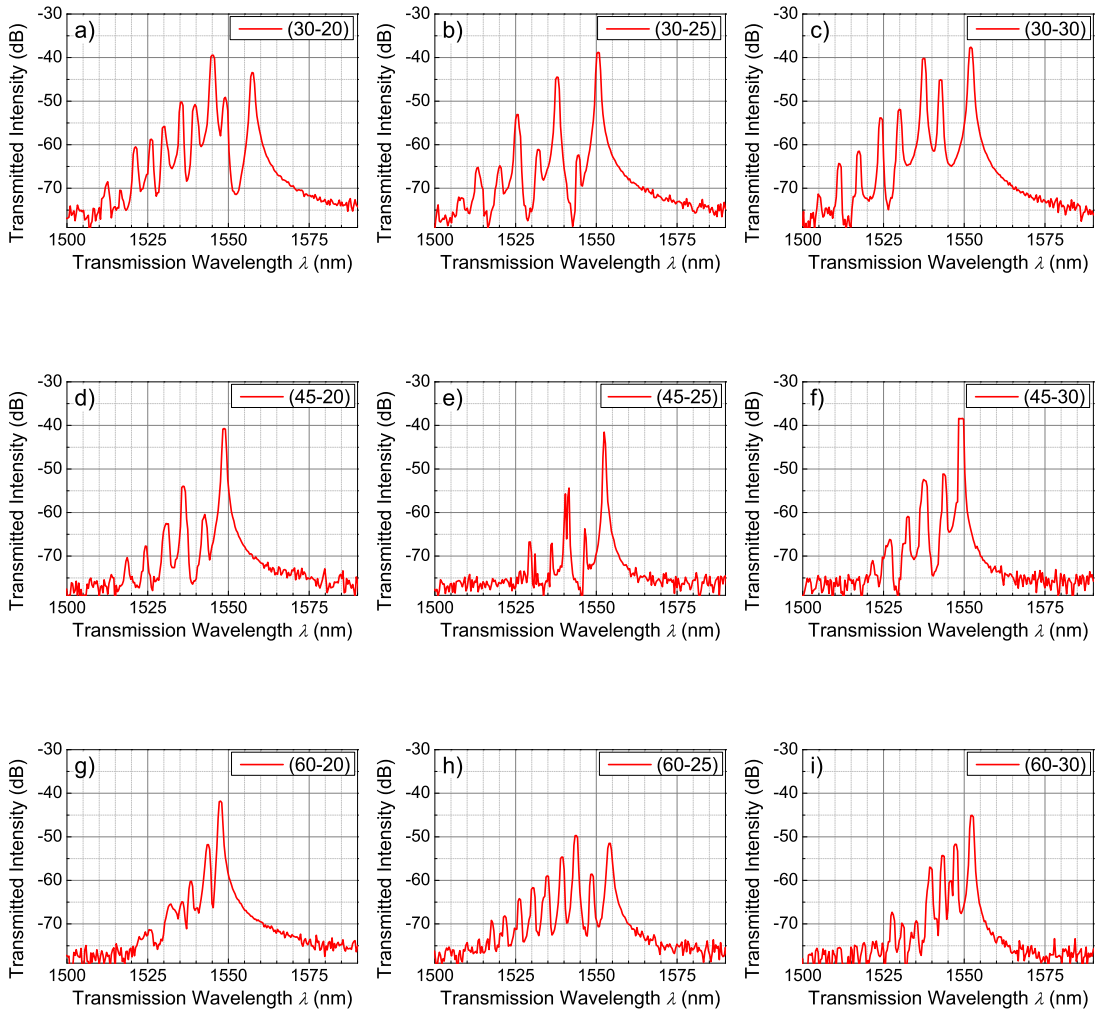

Figure 4.23: Single transmission spectra for small-sized SiO_x-SiC_z MEMS-DBR filters for sizes ($L_{arm} - W_{arm}$) tuned to 1550 nm.

Substrate Temperature Dependence

Substrate temperature-dependent wavelength-shifts are investigated for SiO_x-SiC_z and SiO_x-SiN_y in section 4.1.6. Here, corresponding measurements for small-sized filters are presented. To reduce the effect of tuning efficiency non-linearities, discussed in section 3.4, the linear range around center-wavelength 1550 nm is employed for each device. With a DBR reflectivity stopband above 300 nm this is even sufficient for a filter with the smallest MEMS-arms (30-20). Resulting measurements are summarized in fig. 4.24. Groups for MEMS-DBR arm lengths and widths can be seen in fig. 4.24 with both longer and wider arms decreasing the dependence on T_S. The shorter arms have a steeper slope, dividing the devices into three groups. Within each group, the same order appears, showing a steeper slope with narrower arms. Less MEMS-DBR material extends more for the same temperature change. In table 4.14 all slopes are summarized underlining the discussion.

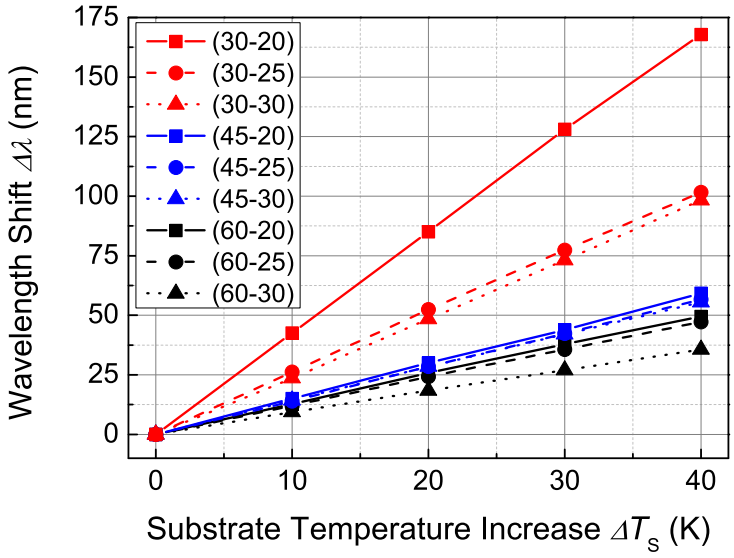

Figure 4.24: Resonant wavelength shift on substrate temperature for small filter sizes (MEMS-DBR arm widths and lengths).

Table 4.14: Resonant wavelength shift depending on T_S for small-sized filters.

L_{arm} (µm) \ W_{arm} (µm)	20 (nm/K)	25 (nm/K)	30 (nm/K)
30	4.18	2.54	2.48
45	1.48	1.46	1.42
60	1.24	1.18	0.92

4.3.2 Increased Number of Layer-Pairs

After increasing tuning range by the reduction of L_{air}, the next step is to decrease transmission linewidth of a SiO_x-SiC_z MEMS-DBR filter. To do so, an increase in DBR layer pairs is necessary, see fig. 3.6 and eq. (4.17). In this section filters are fabricated according to figs. 4.2 to 4.5 with 8 (8.5) SiO_x-SiC_z layer pairs for bottom-DBR (top-DBR). The results are compared with SiO_x-SiC_z and SiO_x-SiN_y MEMS-DBR filters investigated in section 4.1. The resulting air-gap of $L_{air,8} = 9\,\mu m$ is about 1 µm below the air-gap of a SiO_x-SiC_z MEMS-DBR filter with $M = 6$. The resulting tuning is shown in fig. 4.25 left. Please note that here modes 13 and 14 can be seen, while previously modes 14 and 15 were identified in fig. 4.10, because cavity-length is reduced here. Furthermore, fig. 4.25 right shows a wavelength-shift induced by an increase of T_S. Two additional pairs result in a 44 % increase of temperature dependence.

Figure 4.26 proves that the linewidth was drastically reduced due to an increase of mirror reflectivity. It is below SiO_x-SiN_y DBR linewidth, and the broad reflectivity bandwidth of SiO_x-SiC_z DBR is even more obvious here. Over a range of more than 150 nm, the linewidth is below 0.02 % (or 0.03 nm), corresponding to $\mathcal{F} > 3800$. It cannot be determined how much further the linewidth stays this narrow towards lower wavelengths because the used broadband source ends around 1450 nm. Thus, a narrower linewidth is bought by larger temperature dependence.

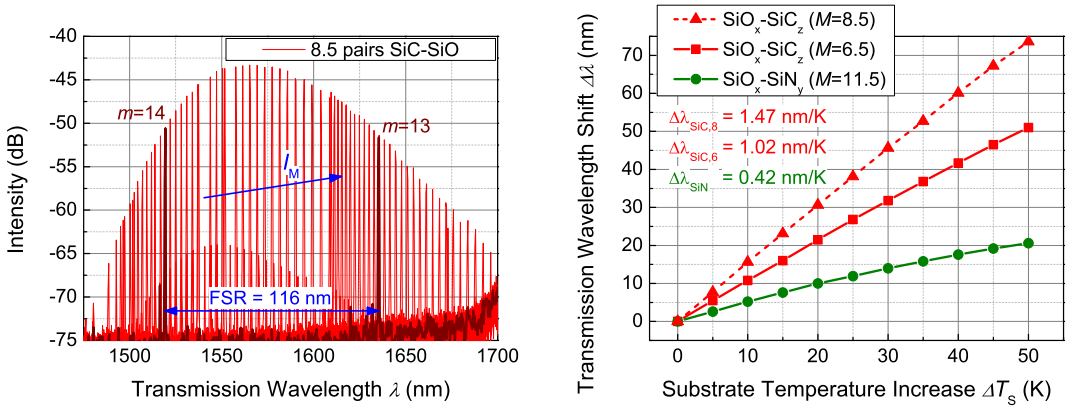

Figure 4.25: **Left:** SiO_x-SiC_z-DBR filter tuned with $I_M = 60\,mA$ to $130\,mA$ at a constant $T_S = 35\,°C$ results in a red-shift of the transmitted spectrum. The entire FSR of 116 nm in mode $m = 14$ can be used (determined with eq. (4.7)). **Right:** Wavelength shift depending on substrate temperature compared with filters investigated in section 4.1.

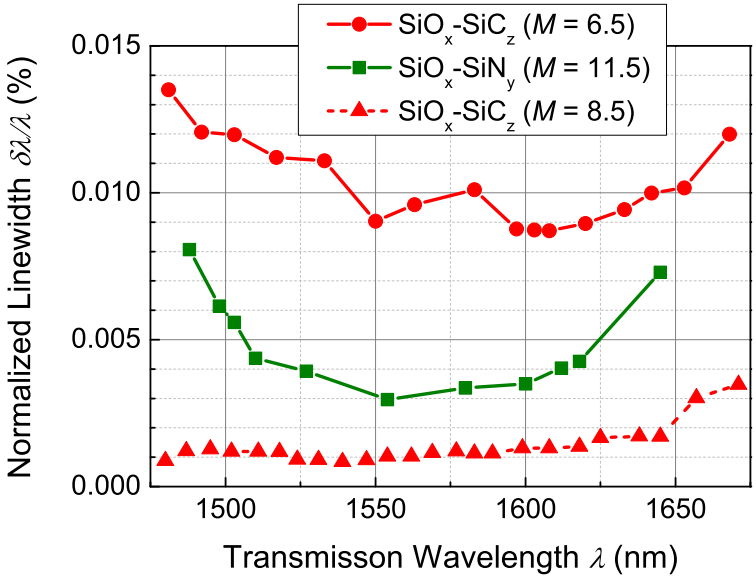

Figure 4.26: Normalized transmission linewidth $\delta\lambda/\lambda$ over wavelength for tunable SiO_x-SiN_y and 2 different SiO_x-SiC_z MEMS-DBR filters.

4.4 Electrostatic Tuning

This section presents the electro-static displacement of the MEMS-DBR to adjust cavity-length. In contrast to electro-thermal actuation, a second conducting electrode is required to create an electric field with attracting force. Therefore, the processing prolongs by an additional metallization and structuring step on the bottom-DBR below the sacrificial layer. The sacrificial layer mask maximizes the overlapping areas of the top and bottom electrodes. An aperture in the center prevents reflection at the electrode inside the resonator. The lower electrode processing step is presented in fig. 4.27 A). Moreover, the released electro-statically tunable MEMS-DBR filter with small-sized MEMS is shown in row B). Now, the bottom electrode is visible between MEMS-arms. The contacting needles can be applied at any point.

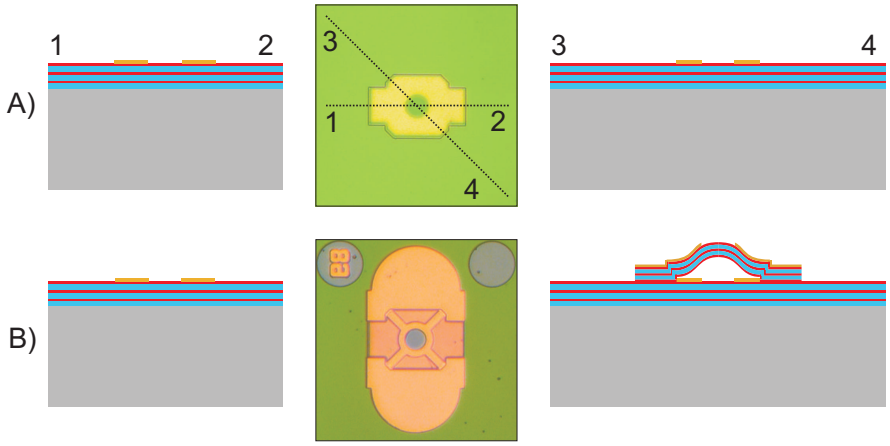

Figure 4.27: Additional steps for an electro-statically tunable MEMS-DBR filter. **A)** lower electrode on bottom-DBR with an aperture in the center. **B)** released electro-statically tunable MEMS-DBR filter.

Two devices with initial air-gaps of 3.5 µm and 4.6 µm demonstrate the electro-static MEMS-DBR actuation. U_{MEMS} is applied between bottom- and top-electrode with two contacting needles. As described in section 2.4, the applied voltage sign does not matter. In both cases, the attracting force moves the MEMS-DBR closer to the substrate, reducing the cavity-length. This effect can be seen in fig. 4.28. For both positive and negative voltages, a blue-shift occurs in contrast to the red-shift observed with increasing I_{MEMS} for electro-thermal displacement. The colors represent two different initial air-gaps due to different MEMS sizes (3.5 µm for (45-30) and 4.6 µm for (60-30)). As expected, an increase

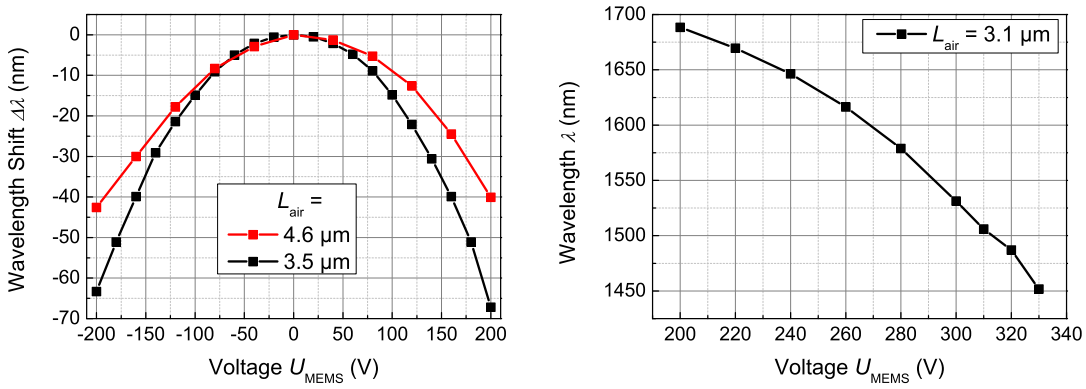

Figure 4.28: Left: Electro-static displacement of SiO_x-SiC_z MEMS-DBR filter and corresponding wavelength shift for two different initial cavity-lengths. Voltage sign does not matter, because resulting force always attracts the MEMS-DBR. **Right:** Electro-static wavelength tuning through the entire FSR of 274 nm for a SiO_x-SiC_z MEMS-DBR filter with $L_{air} = 3.1\,\mu m$. Substrate temperature is $T_S = 15\,°C$.

in wavelength-shift at the same voltage results from a smaller electrode distance (black). Figure 4.28, right, presents a third filter to see the requirement for tuning through the entire FSR. Here, the voltage begins at 200 V to shift the resonator mode into the SOA spectrum. An additional 130 V moves the mode another 270 nm across its FSR, see fig. 4.28, right.

The next development step would be to reduce the required voltage by reducing the distance between the electrodes and reducing the movable MEMS-DBR mass by removing material not needed for mirror reflectivity, like the thickness of the MEMS-arms.

5 MEMS-DBR Tunable Modules

This chapter applies the MEMS-DBR technology to both PD and half-VCSEL substrates to create tunable detectors and sources, respectively.

5.1 Tunable Detectors

In this section, the previously described MEMS-DBR tunable optical filter is not grown on a silicon substrate anymore but a PIN-PD instead. With this setup, the MEMS-DBR resonator first filters the signal. Afterwards, the PD transforms it into a photocurrent. The cross-section of the PD is presented in fig. 2.10, left. On top of the semiconductor already an SiN_y ARC is deposited. This is important for the bottom-DBR. The first DBR-layer needs to be a high refractive index material.

A MEMS-DBR tunable PD is a MEMS-DBR tunable filter grown on a PD substrate. But the presence of PD contacts on the substrate surface requires some adjustments to the filter processing steps presented in figs. 4.2 to 4.5. The changes are listed in fig. 5.1. Row i) shows a PD substrate, here the Au contacts on the front-side have an aperture in the center for the filtered light to enter the semiconductor. The contact layers add additional profile steps in the following layers. However, at a thickness of approximately 100 nm (aperture ring) and 300 nm (beams connecting the ring and the large pads), it does not disturb the DBR too much. Moreover, in the center, the substrate and subsequently, the DBR surface is flat. The purple color of the semiconductor surface is a SiN_y ARC. The gray substrate is described in more detail in fig. 2.10. Row ii) shows a structured Ni protection layer. It is required because the previously mentioned Au contact pads need to be accessed to bias the photodiode and to measure the photocurrent. Accordingly, both top and bottom-DBR are removed by dry-etching. A Ni protection-layer below the bottom-DBR prevents the DBR dry-etching gases from damaging the contact pads. The shape stems from an inverted MEMS-etch mask from fig. 4.4 k). Row iii) shows an adjusted Ni

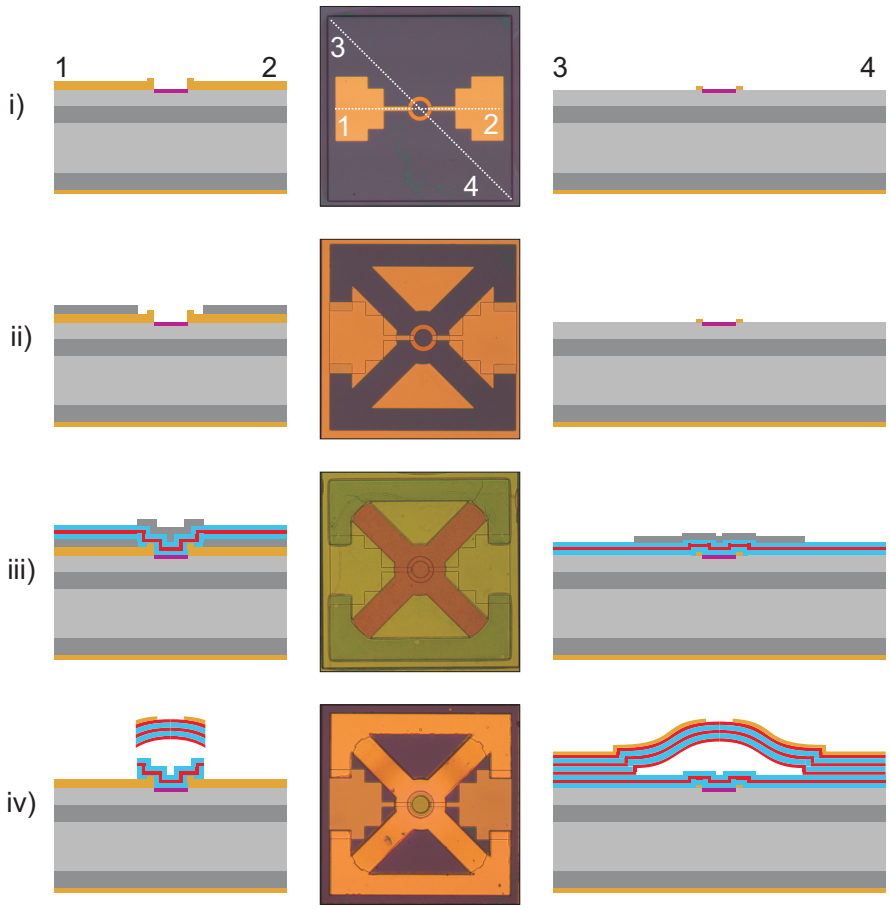

Figure 5.1: Processing steps for MEMS-DBR tunable photodiodes extending filter processing in figs. 4.2 to 4.5. **i)** Photodiode substrate with Au contacts on front and backside. **ii)** Ni protection layer for PD Au contacts to stop b-DBR dry-etching. **iii)** Adjusted sacrificial layer to enable etching of b-DBR. **iv)** Finished sample with released MEMS-DBR.

sacrificial layer that does not stop dry-etching of the bottom-DBR. The last row iv) presents the finished released MEMS-DBR. Au-contact pads are open after removing the Ni MEMS etch-mask, the Ni sacrificial layer and the Ni Au-contact protection layer simultaneously.

5.1.1 SiO_x-SiN_y MEMS-DBR Tunable Photodiode

First, the old material combination of SiN_y and SiO_x is used to test the feasibility of a tunable photodiode. Here both bottom- and top-mirrors consist of 11.5 layer pairs (23 layers). table 5.1 lists the properties of the DBR layers. Note that in comparison to SiC_z-SiO_x-DBR, there are two different types of SiN_y layers which show opposite signs of stress. These SiN_y layers with tensile stress (positive) introduce a stress gradient to counteract the bending of the compressive stress (negative) layers to reduce the initial air-gap. It is assumed that it is necessary to achieve the desired shape of the bent DBR mirror [57]. Nevertheless, as shown in the results of SiC_z-SiO_x-MEMS-DBR, this step is not necessary as the preferred shape can also be achieved with compressive-only layers. Moreover, as seen in chapter section 3.1, tensile stress in SiC_z-layers is not possible within the tested deposition parameter ranges.

Table 5.1: Properties of layers used for SiN_y-SiO_x-MEMS-DBR on photodiodes.

layer	$n_{1550\,nm}$	σ (MPa)	thickness (nm)
SiN_y 1	1.85	+100	197
SiN_y 2	1.92	-150	182
SiO_x	1.45	-120	276

Because transmission cannot be detected here, an altered setup is required here to align the lens system to the MEMS, in contrast to fig. 4.7. Instead, the reflection spectrum is regarded during alignment. Because an FPR is transmittive for a small wavelength range, this part of the spectrum is missing in reflected direction. Thus in fig. 5.2 dips in the SOA spectrum are visible instead of transmission peaks. Air-gap here is 7.5 µm which results in an FSR of 189.6 nm.

Next, responsivity measurements with and without a filter are shown for 5 DFB lasers at five different wavelengths set to 0 dBm each, resulting in fig. 5.3. Each laser is attached to the lens one by one. Both curves have a maximum in the center and small drops towards larger and smaller wavelengths. The difference between black and green points are the insertion losses into the SiO_x-SiN_y MEMS-DBR filter. They stem from both alignment imperfections during processing and misalignment of the collimator-lens system for coupling light from a single-mode fiber into the MEMS-DBR aperture. Moreover, reflection at the PD surface is present. The filter is transparent at the resonant wavelength. It means the incoming light sees the PD with an ARC.

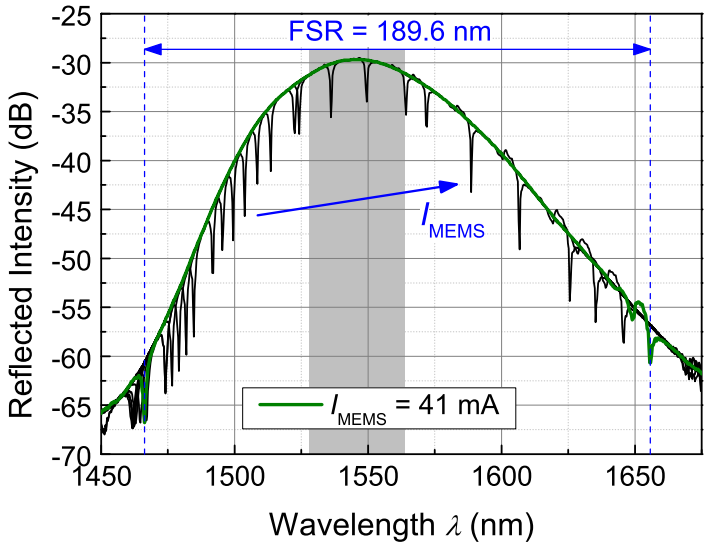

Figure 5.2: Reflection spectra of a SiO_x-SiN_y MEMS-DBR filter grown on a photodiode. Here, substrate temperature is $T_S = 20\,°C$. Gray area identifies the range of the DFB lasers tested in figs. 5.3 and 5.5. In green one spectrum is highlighted to measure FSR.

Next, five distributed feedback (DFB) lasers multiplex simultaneously into a single fiber, see fig. 5.4. Here two laser wavelengths represent neighboring channels of a DWDM grid, spaced at 100 GHz or approximately 0.8 nm, to see whether this setup could be used on the receiver side of a data communication system. Wavelength multiplexing is done with a 100 GHz AWG which couples up to forty channels into one output single-mode fiber. The resulting photocurrent I_{ph} is shown in fig. 5.5 depending on I_{MEMS}. The photodiode is reverse biased at $-1\,V$.

All five lasers can be identified. A larger MEMS current causes a red-shift of resonant wavelength. Both neighboring channels at 1543.7 nm and 1544.5 nm can be distinguished, see fig. 5.5 left. But there is still quite a large overlap resulting in much higher I_{ph} than at the other three lasers although all of them were set to the same output power of 0 dBm at the collimator input. In fig. 5.5 right I_{Ph} is shown again for four different DFB lasers. First I_{MEMS} is increased from 15 mA to 30 mA, then decreased again from 30 mA to 15 mA. Please note that the laser responses in the photocurrent do not coincide at the same I_{MEMS}. This raises the need for a feedback loop, determining which wavelength is

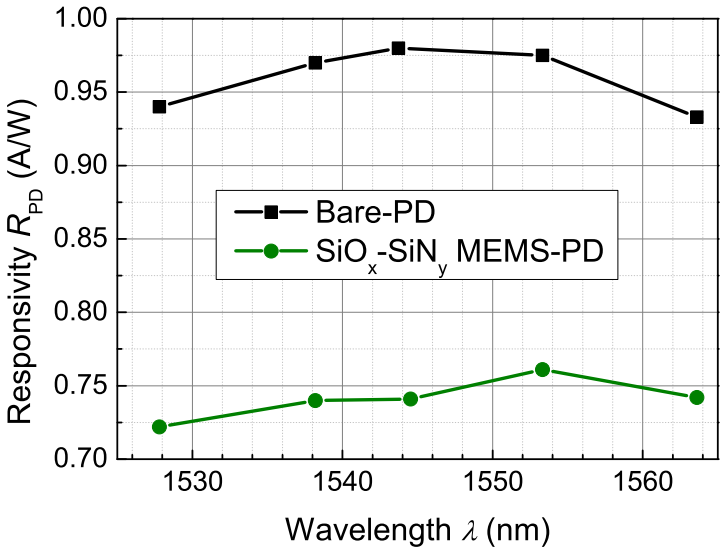

Figure 5.3: Responsivity R_{PD} of a photodiode for 5 DFB lasers with different wavelengths. Substrate temperature is $T_{\mathrm{S}} = 20\,^{\circ}\mathrm{C}$.

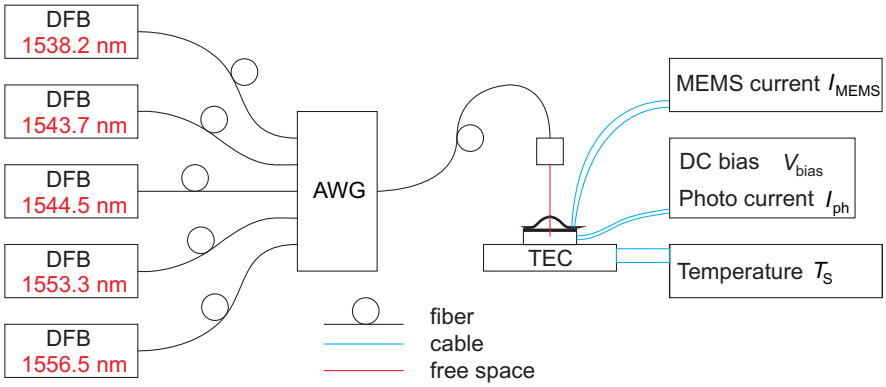

Figure 5.4: Setup with multiple DFB lasers coupled into one fiber. Light is collimated through a collimator-lens system and guided through the opening of top-DBR MEMS aperture into a tunable photodiode. Sample is temperature stabilized at 20 °C. PD is reverse biased and I_{ph} is recorded while MEMS is actuated by I_{MEMS}.

transmitted because MEMS actuation shows a hysteresis behavior. Results from this chapter are published in [6].

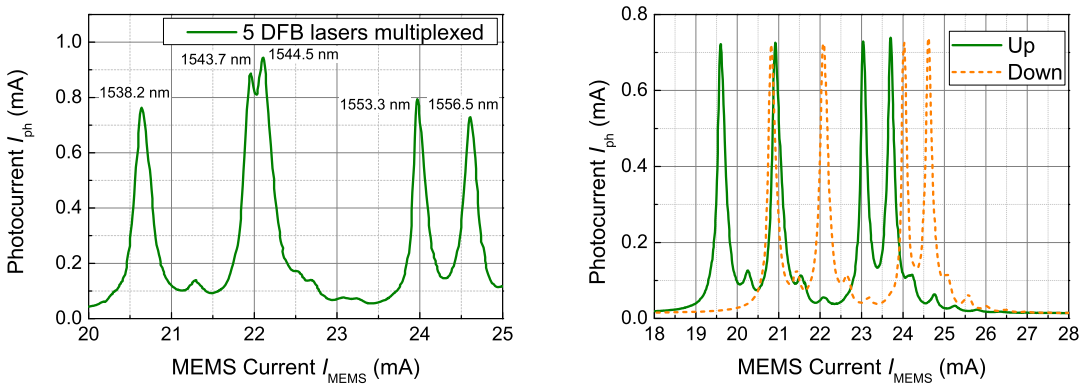

Figure 5.5: Photocurrent of a SiO_x-SiN_y MEMS-DBR PD biased at -1 V depending on I_{MEMS}. **Left:** Five DFB lasers at different wavelengths directed at a SiO_x-SiN_y MEMS-DBR PD to investigate selectivity. **Right:** Four DFB lasers (0 dBm each) at different wavelengths with corresponding photocurrents for increasing and decreasing MEMS current.

5.1.2 SiO_x-SiC_z MEMS-DBR Tunable Photodiode

To see whether selectivity can be improved, a SiO_x-SiC_z MEMS-DBR filter is grown on the same kind of PD substrate as in the previous section 5.1.1. For selectivity, the linewidth is very important, thus here 8.5 layer pairs are used for the MEMS-DBR, being processed in parallel to samples from section 4.3.2. A linewidth below 0.03 nm can be expected here. Nonetheless, filtering is not very narrow, and it is tough to identify dips in the reflection spectrum, see fig. 5.6. An inset with a zoomed-in area magnifies the dips. Dips of 0.2 dB occur, while fig. 5.2 shows dips of up to 7 dB. The reason for this must come from SiC_z absorption identified in fig. 3.1. With losses in the DBR layer, transmitted intensity detected by the photodiode is reduced. Moreover, alignment problems of the collimator-lens system towards MEMS-DBR aperture and processing-related issues always accompany the samples but should not differ much between SiN_y- and SiC_z-based samples.

Figure 5.7 left presents the spectra of four multiplexed DFB lasers set to 0 dBm each, reflected from a SiO_x-SiC_z MEMS-DBR PD. Laser two and three represent a neighboring channel separation of 100 GHz or approximately 0.8 nm in a DWDM data transmission system. Figure 5.7 right shows I_{ph} for increasing (green) and decreasing (orange) I_{MEMS}. Similarly to the behavior in fig. 5.7, right, the positions of up and down direction do not coincide but are much

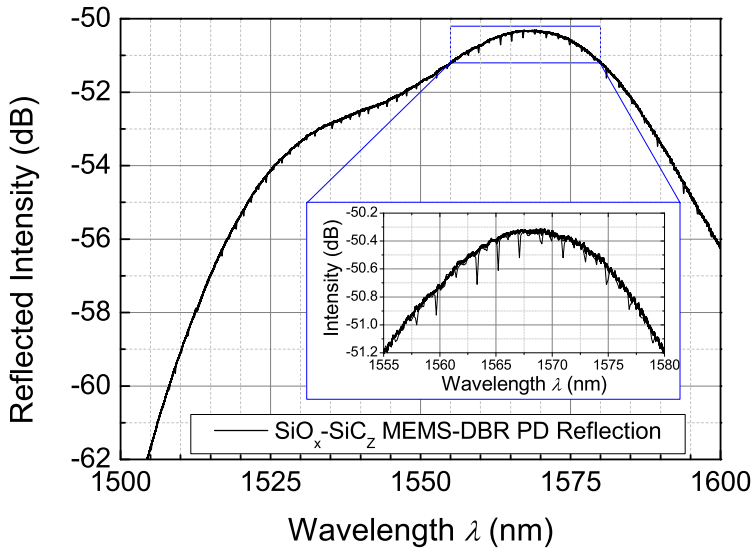

Figure 5.6: Reflection sepctra of a SiO_x-SiC_z MEMS-DBR filter grown on a photodiode. The inset emphasizes the very small reflection dips. Only a small amount of light reaches the photodiode itself.

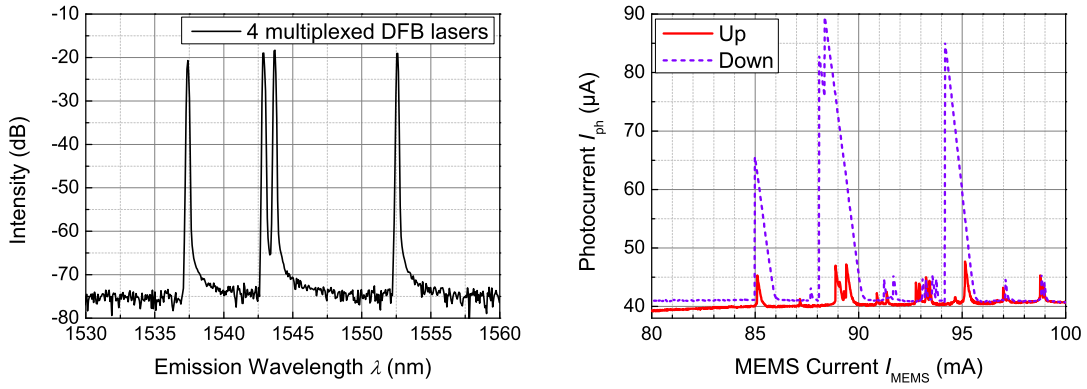

Figure 5.7: **Left:** Four DFB lasers (0 dBm each) multiplexed into one single mode fiber as source for a SiO_x-SiC_z MEMS-DBR PD. **Right:** Photocurrents of a SiO_x-SiC_z MEMS-DBR PD biased at -4 V depending on I_{MEMS} for increasing and decreasing MEMS current.

closer than for SiO_x-SiN_y MEMS-DBR PD. The current ranges between 80 mA to 100 mA with 0.01 mA steps to resolve laser two and three. It highlights the

need for very accurate current controlling at these large MEMS currents (Here Ti/Au top electrode thickness is about 130 nm). Moreover, I_{ph} is very low when compared to fig. 5.7 right. It fits the shallow reflection dips from fig. 5.6. Only very little power is transmitted through the filter into the PD. One additional reason for this might be the very narrow linewidth of the filter. It means a very accurate setting of cavity-length is necessary to coincide with the laser wavelength. Although the setting of the current source suggests an accuracy of 0.01 mA, maybe internally it is lower or prone to noise. Due to environmental influences like temperature fluctuations, MEMS-DBR is always moving beyond the required accuracy to find the laser signal. The discrepancy between up and down suggest a more stable source when reducing current than in the case of a current increase, hence a much lower I_{ph} for olive data points.

An implementation for MEMS-stabilization was developed previously for SiO_x-SiN_y MEMS-DBR VCSEL [26]. Here a small part of output power is coupled into an etalon which could detect whether the incoming wavelength shows a red- or blue-shifting and reacts with an adjustment in I_{MEMS} accordingly. Moreover, a command is implemented to tune the emission wavelength in 0.8 nm steps.

Thus, in the case of SiO_x-SiC_z-MEMS-DBR PD, a broader linewidth might be desirable to reduce the effect of MEMS-fluctuations to have a larger error margin for the MEMS-current setting to detect a laser. Moreover, a thinner top electrode would reduce the absolute value of I_{MEMS} where the current source might be more stable.

5.2 SiO_x-SiC_z MEMS-DBR Tunable VCSEL

In this section, the SiO_x-SiC_z MEMS-DBR technology is applied to a half-VCSEL substrate containing a flat backside mirror and a broadband active region. On top of the surface, a MEMS-DBR is grown. Processing steps are adjusted because the structured half-VCSEL layers are prone to be damaged by wet chemical steps previously applied for tunable SiO_x-SiC_z MEMS-DBR filters and photodiodes. Afterwards, wavelength tuning, voltage-current behavior and temperature dependence are investigated. Figure 2.11 shows the half-VCSEL cross-section. Processing steps that deviate from MEMS-DBR filter fabrication are presented in section 4.1.1.

Figure 5.8 I) presents a half-VCSEL in the center with backside VCSEL p-contact at number 1 and the frontside n-contact connected to the center aperture at number 2. In the aperture the InP semiconductor is visible. The dark dots on the sample are results from processing issues during half-VCSEL fabrication. Although they do have heights of several 100 nm, they do not disturb the optical path because the laser eye in the center is not affected. A tunable MEMS-DBR VCSEL is a three-mirror-system, bottom-DBR, semiconductor-air-gap interface and top-DBR. On the left and right side, there are two cross-sections marked in the center picture. A SiN_y ARC ($n_{SiN_y} \approx 1.82$) reduces the reflection losses within the cavity. It is deposited on the InP aperture and structured using lift-off in row II). Now the aperture is purple. The thickness is designed for a center-wavelength of 1550 nm. In the last row III), a Ni sacrificial layer can be seen. It is structured by wet-chemical etching, employing HNO_3. At this point, this does not pose a threat to the mesa because in the aperture Ni remains, and the solution does not come in contact with the center. Here, the small-sized structure demonstrates the new masks introduced in fig. 4.21.

Figure 5.9 IV) skips several steps in the overview and presents the sample with deposited top-DBR and lift-off structured top electrode. Here, the approximate size of the MEMS-DBR arms can be seen. The top electrode aperture has the same diameter as previously used for the standard-sized masks. In the second row V) again, several steps are skipped. The MEMS-DBR Ni etch mask is deposited and defined by lift-off. Subsequently, DBR dry-etching is performed, and the sacrificial layer is now exposed. Here, the sacrificial layer size requires special care. As seen in fig. 5.8 III), the Au contact pads are not covered. Dry-etching has to be timed well to minimize exposure time. HNO_3 removes the exposed Ni sacrificial layer and MEMS etch-mask but it needs to be stopped before under-etching starts. During SiO_x-SiC_z MEMS-DBR filter

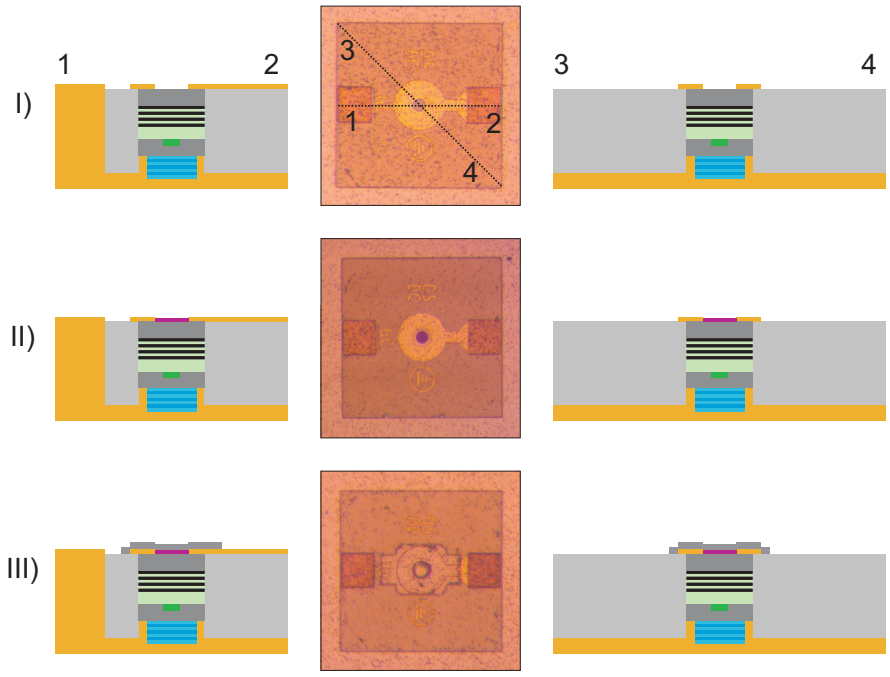

Figure 5.8: Processing steps for MEMS-DBR tunable VCSEL extending filter processing in figs. 4.2 to 4.5. **I)** Half-VCSEL substrate with Au contacts for back (p-type, left) and front sides (n-type, right). **II)** SiN_y ARC layer structured by lift-off. **III)** Small-sized Ni sacrificial layer.

and photodiode processing a Ni sacrificial layer is removed wet-chemically by a diluted HNO_3 solution. Here, this step poses a problem, because HNO_3 also attacks the InP semiconductor below, causing an open-circuit behavior. HNO_3 is replaced by TFG which has a similar etch rate at 50 °C but offers increased selectivity towards metal and semiconductor layers. Unfortunately, TFG does attack the Au layer as well. For this reason, the top electrode is covered with PR during under-etching. The effects can still be seen at the contact pads, which turn to a darker shade in fig. 5.9 VI). Because the contact pads have a thickness of 2 µm, removing several tens of nm does not pose a severe threat. The released and critical-point dried MEMS-DBR VCSEL is presented with small-sized MEMS in row VI). Furthermore, SiO_x-SiC_z MEMS-DBR VCSEL is structured with the standard-sized masks from fig. 4.1, but processing steps are not presented here.

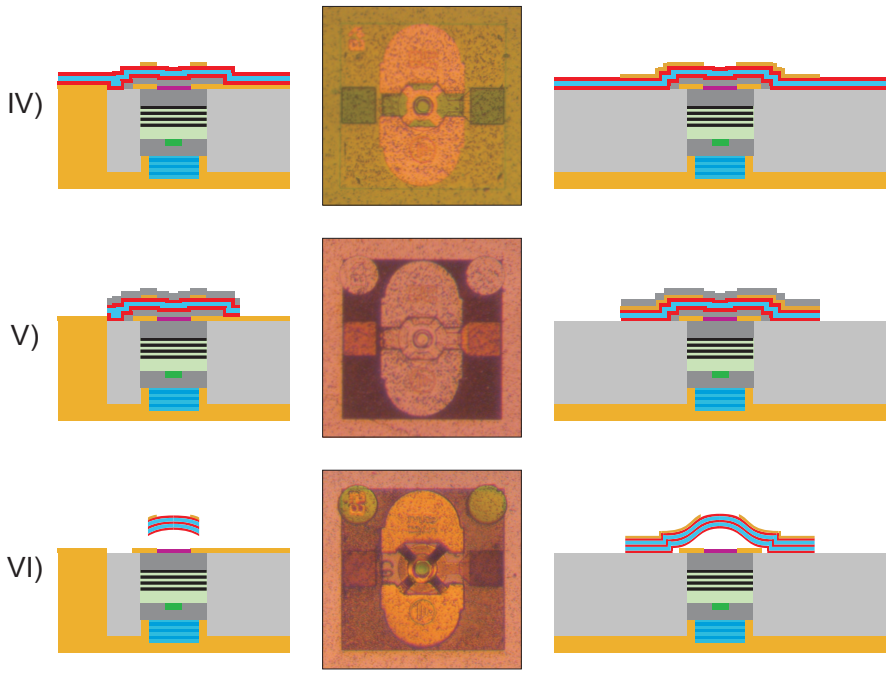

Figure 5.9: Processing steps for a MEMS-DBR tunable photodiodes extending filter processing in figs. 4.2 to 4.5. **IV)** Deposited DBR and lift-off-structured top Au-electrode. **V)** Ni MEMS etch-mask structured and DBR dry-etched. Au laser contact pads are now exposed. **IV)** Finished sample with released MEMS-DBR.

5.2.1 Standard-Sized MEMS-DBR

The first evaluation is done with standard-sized masks from fig. 4.1 to test technological compatibility without too many changes in comparison to known behavior well investigated in [53, 59]. Figure 5.10 shows an emission spectrum of a SiO_x-SiC_z MEMS-DBR VCSEL. At 1504 nm, the highest output power is measured. The maximum gain of the active region is around 1560 nm. Because the highest output power is at 1504 nm it is assumed that the DBR center-wavelength is not at the designed wavelength of 1550 nm but has a large blue-shift. Measuring the DBR thickness with a surface profiler supports this assumption. Because overcoming the laser threshold requires high reflectivities above 99.5 % only here lasing is possible. The SMSR of 60 dBm is very high. Next to the main peak, the next higher-order mode at 1457.7 nm can be seen. It gives an FSR of 47.7 nm. The MEMS-DBR tunable VCSEL cavity consists of a semiconductor half-VCSEL with a physical thickness of L_{sc} =2.1 µm to 4.65 µm [52, 59] and the tunable air-gap. The total optical cavity-length L_c can be written

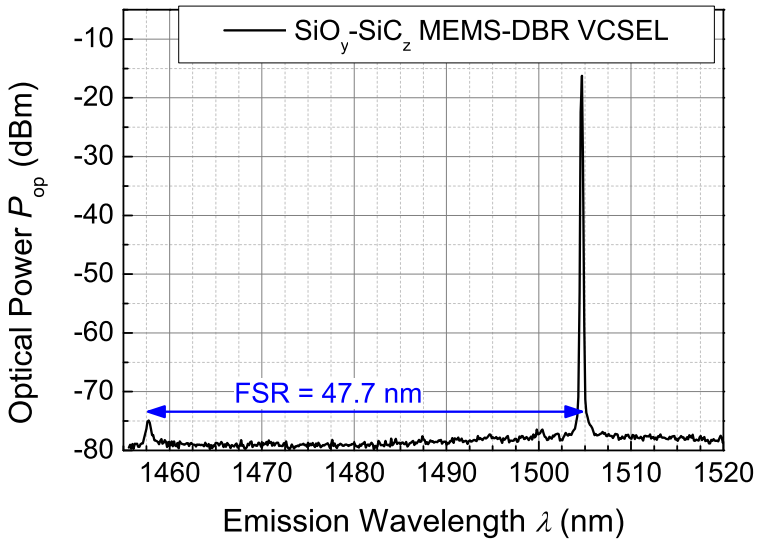

Figure 5.10: Emission spectrum of a standard-sized SiO_x-SiC_z MEMS-DBR VCSEL with $L_{air} = 13\,\mu m$.

as

$$L_c = n_{sc} \cdot L_{sc} + n_{air} \cdot L_{air}, \tag{5.1}$$

where the refractive index of the semiconductor (SC) is a combination of InP ($n_{InP} = 3.16$) and InGaAs ($n_{InGaAs} = 3.4$) and estimated here as $n_{SC} = 3.3$ [16, 63]. Now it is possible to approximate L_{SC} with eq. (2.16). The resulting physical semiconductor thickness is roughly

$$L_c = \frac{\lambda^2}{2 \cdot FSR} = \frac{1457.7\,nm^2}{2 \cdot 46.3\,nm} \tag{5.2}$$

$$L_{sc} = \frac{L_c - L_{air}}{n_{sc}} \approx 3\,\mu m. \tag{5.3}$$

In fig. 5.11 the same device is studied for several substrate temperatures T_S. The top electrode is damaged due to issues during processing and cannot actuate the MEMS-DBR electro-thermally. Nevertheless, as seen in fig. 4.11, cavity-length can be adjusted with T_S as well. Starting at room temperature (RT) of about 25 °C, increasing and decreasing temperature change the emission wavelength. Please note that the wavelength shift $\Delta\lambda$ is negative. An increase of

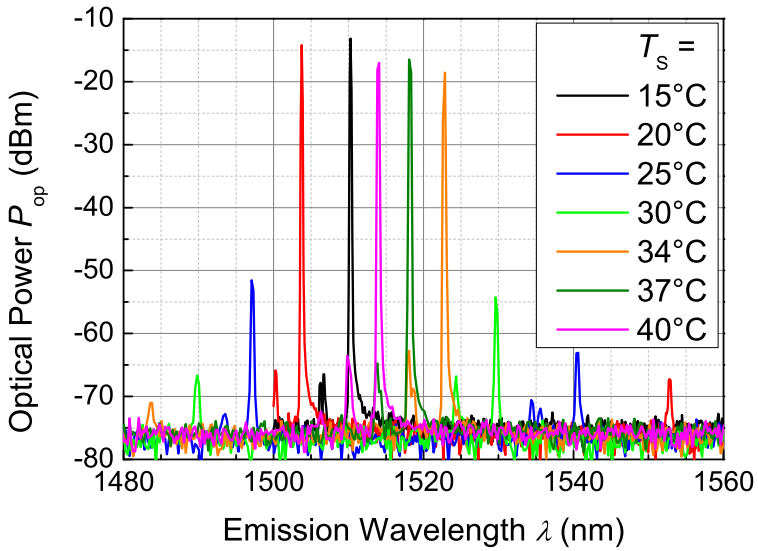

Figure 5.11: Emission wavelength tuning with substrate temperature T_S for a standard-sized SiO_x-SiC_z MEMS-DBR VCSEL with $L_{air} = 13\,\mu m$.

T_S reduces cavity-length. The explanation for this behavior follows. The half-VCSEL used in this work is designed for high-speed modulation of up to 7 GHz [59]. Consequently, the semiconductor around the mesa is replaced by BCB (benzocyclobutene) to minimize parasitic capacities. BCB offers a much larger temperature coefficient than the semiconductor or dielectric layers in a SiO_x-SiC_z MEMS-DBR. Consequently, the substrate expands more than the MEMS due to a temperature increase and L_{air} is reduced. For temperatures 20 °C and 15 °C L_{air} increases accordingly and a red-shift in emission wavelength occurs. The tuning range is limited to 20 nm around 1512 nm because of two device properties. Towards smaller wavelengths, the gain profile of the active medium limits the stimulated emission. Its center is around 1560 nm and reduces to either side. On the other side, the limiting factor is the cavity-length and DBR reflectivity-shift, which only allow for 40 nm to 50 nm of FSR. As stated before, the DBR center-wavelength is not at the designed wavelength of 1550 nm but is blue-shifted. Although the SiO_x-SiC_z DBR stopband is very wide, a VCSEL cavity needs very high reflectivities for lasing operation. Here a DBR with only 6.5 layer pairs is deposited, which additionally shows a blue-shift. In combination, the tuning range is very limited here. Moreover SiC_z absorption has an influence on the DBR reflectivity, presented in figs. B.1 and B.2. In both

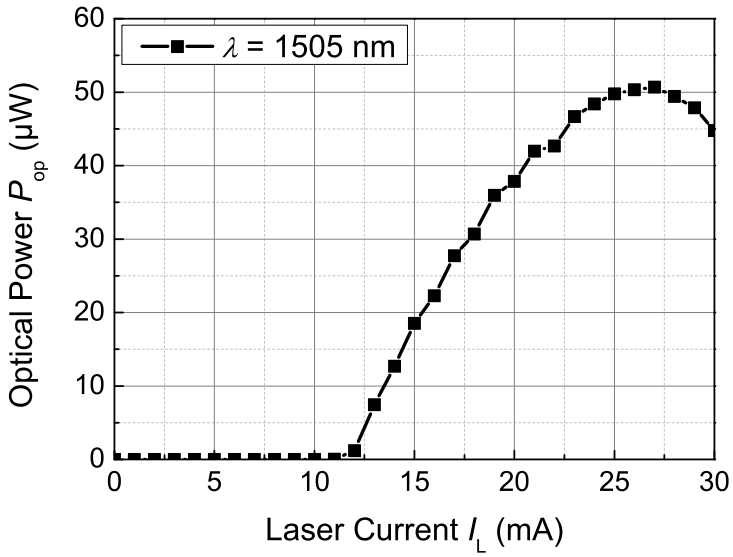

Figure 5.12: Emission power depending on laser current of a standard-sized SiO_x-SiC_z MEMS-DBR VCSEL with $L_{air} = 13\,\mu m$.

figures a reduction in maximum reflectivity can be observed in comparison to a SiO_x-SiN_y DBR. TMM simulations also show a blue-shift in the position of the maximum reflectivity, see fig. B.1. Accordingly, the output power is considerably lower than for a SiO_x-SiN_y MEMS-DBR VCSEL ($-10\,dBm$ to $0.4\,dBm$ at $1520\,nm$) [52].

In the final graph for a standard-sized SiO_x-SiC_z MEMS-DBR VCSEL, optical power P_{op} over laser current I_L is presented. Here $T_S = 16.5\,°C$, to investigate the highest output power found at $1505\,nm$. Threshold current of approximately $11\,mA$ can be seen in fig. 5.12. This value fits the findings of SiO_x-SiN_y MEMS-DBR VCSEL published before [59] and corresponds to lower material gain at this wavelength in comparison to the designed center of $1560\,nm$. An increase in output power can be seen with higher I_L until a maximum of $50\,\mu W$ or $-13\,dBm$ at $27\,mA$ is reached. For higher I_L thermal rollover with a power drop is recognizable. Although P_{op} is very low, lasing occurs. Characteristics speaking for this effect are the threshold behavior in fig. 5.12 and narrow linewidth from fig. 5.10.

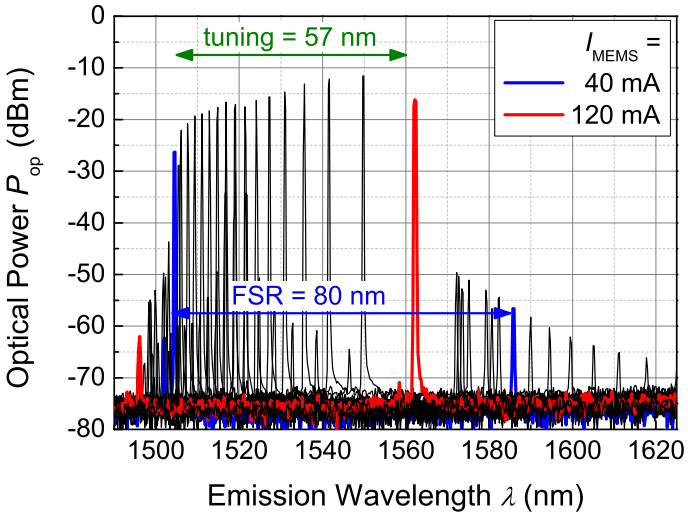

Figure 5.13: Emission wavelength for small-sized SiO_x-SiC_z MEMS-DBR VCSEL with $L_{air} = 5.2\,\mu m$

5.2.2 Small-Sized MEMS-DBR

According to cavity reduction with small-sized MEMS-DBR filters, here, the same photolithography masks are applied. Small-sized SiO_x-SiC_z MEMS-DBR do offer a much larger tuning range due to a smaller L_{air} of 5.2 µm presented in fig. 5.13. Here, the MEMS-electrode can be used for tuning, and the presented spectra are obtained with $I_{MEMS} = 40\,mA$ to 120 mA. The tuning range is 57 nm. The highest output power of $-11.5\,dBm$ or 71 µW is located at an emission wavelength of 1550 nm. Here again, a blue-shift of DBR center-wavelength is apparent - the DBR is deposited together with the DBR of the device in section 5.2.1. Lasing beyond 1562 nm to use the entire FSR of 80 nm cannot be obtained because the next higher mode experiences a higher amplification due to a higher DBR reflectivity around 1500 nm. To increase the tuning range even further both reduction in air-gap to increase FSR and a shift of the DBR center-wavelength towards higher value is required. Then it is possible to utilize the entire gain width.

For small-sized SiO_x-SiC_z MEMS-DBR the emission wavelength depending on T_S is presented in fig. 5.14 for two constant lasing currents I_L. As before, a negative slope occurs. I_L creates a constant offset possibly due to a higher pn-junction temperature which influences the temperature-dependent n_{SC}. A

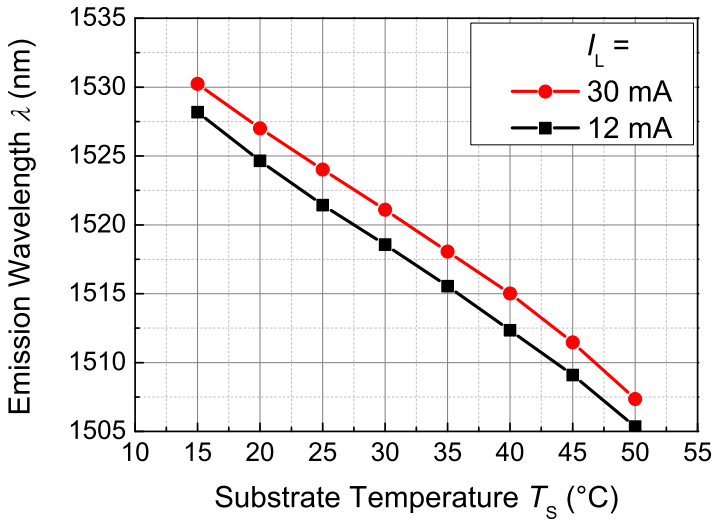

Figure 5.14: Emission wavelength of a small-sized SiO_x-SiC_z MEMS-DBR VCSEL for varying T_S at two different laser currents I_L. The air-gap is $L_{air} = 5.2\,\mu m$

slope of $-0.65\,nm/K$ is smaller than the slope for results in fig. 5.11 of $-1.4\,nm$ due to the reduction of MEMS size. However, more importantly, SiO_x-SiC_z MEMS-DBR VCSEL emission wavelength temperature-dependence is more than one order of magnitude smaller than for SiO_x-SiN_y MEMS-DBR VCSEL with comparable L_{air}. They show a slope of approximately $-9.4\,nm/K$ [59]. Consequently, a SiO_x-SiC_z MEMS-DBR VCSEL is much less prone to environmental temperature fluctuations and should offer higher stability.

6 Summary and Outlook

Summary

In this thesis, the well-known MEMS-DBR surface-micro-machining technology based on SiO_x-SiN_y material with a refractive index difference of 0.45 is extended by the introduction of a third dielectric material - silicon carbide (SiC_z). The combination SiO_x-SiC_z offers a much larger refractive index difference of 1. This property has several advantages in terms of optical properties when used as a DBR mirror for a tunable Fabry-Pérot resonator. Due to its larger refractive index, fewer layer pairs for a DBR with reflectivities beyond 99.5 % are required in comparison to a SiO_x-SiN_y DBR. It opens the opportunity to increase wavelength modulation speed due to the smaller movable mass of a MEMS-DBR. However, even more significant is the DBR reflectivity stopband defining the wavelength range within which very high reflectivity occurs. Where DBR stopband was the limiting factor for SiO_x-SiN_y technology with approximately 250 nm, it doubles for SiO_x-SiC_z DBR (510 nm). For reflectivities above 99.5 %, required for lasing operation, the stopband increases for both by a factor of about 2. Although SiC_z shows small absorption in the near-infrared region investigated here, advantages of much wider tuning range surpass additional losses.

SiC_z can be deposited utilizing low-temperature ($< 100\,^{\circ}C$) PECVD reactor which enables many fields of application. In the presented case only this way, it is possible to combine the MEMS-DBR technology with an active half-VCSEL to create a tunable laser source, because the substrate cannot sustain temperatures above 150 °C. Moreover, structuring of SiO_x-SiC_z DBR could be performed by dry-etching in a fluorine-based plasma with etch rates around 100 nm/min.

In this work, deposition parameters are tested, such as gas ratio, pressure and plasma power with a focus on reduction of layer stress in the resulting SiC_z thin-films. This key parameter is responsible for the bending of the MEMS-DBR, forming a stable plane-concave resonator. The resulting selections of recipes can create compressive layer stress of -150 MPa and above. Beyond the DBR

materials itself, the sacrificial layer is investigated as well. It is necessary to release the MEMS-DBR, which eventually bends away from the substrate and forms the desired concave shape. To reduce processing steps, previously used metal sacrificial layer nickel was supposed to be replaced by a photoresist. While Ni dissolves wet-chemically, creating the need for critical-point drying to keep the MEMS released. A photoresist sacrificial layer was supposed to be removed by dry-etching in an O_2 plasma. Ultimately the photoresist could only be removed by liquid acetone also requiring critical-point drying. Moreover, a metal sacrificial layer is more reliable in its reproducibility. Consequently, the photoresist is discarded as an option for the sacrificial layer.

Investigations on tuning efficiency connecting the required displacement of MEMS-DBR and the resulting shift in resonance wavelength show a factor of about 0.4 with nonlinear behavior towards the edges of the DBR stopband. It is caused by a shift of resonant mode nodes inside the DBR or cavity because the wavelength does not match DBR reflectivity maximum. Nevertheless, within the region investigated here around the designed center-wavelength of 1550 nm, tuning efficiency is nearly linear and does not influence tuning behavior any further.

The first batch of tunable filters produced here utilizes the photolithography masks already available and well known. The processing is successful and tuning of 109 nm around 1550 nm can be achieved both with electro-thermal tuning current and substrate temperature. Each method causes a cavity extension and consequently a red-shift. Wavelength shift is measured in transmission of a broadband semiconductor optical amplifier from 1450 nm to 1700 nm. For this reason, up to three modes were visible simultaneously identified as 14, 15 and 16. This tuning range does not yet outperform previous results with SiO_x-SiN_y MEMS-DBR filters due to large initial air-gap of $>10\,\mu m$. Because layer stress cannot reach below -150 MPa by adjusting deposition parameters, a new method had to be developed.

A simulation model in Comsol Multiphysics is developed to reduce the number of experimental tests required to find a suitable change in processing. It takes advantages of the combination of structural and electro-thermal modules in one simulation tool. To fit simulation results to experimental finding, material parameters for the model had to be determined. Since SiO_x did not offer many ranges according to literature for SiC_z, a large number of sources for various Young's Modulus values are available. With a material-constant sweep, a value of $E_{SiC_z} = 40$ GPa was determined. With the means of transfer matrix model, it is determined that a target air-gap of 1 µm to 5 µm is desired to take

advantage of huge SiO_x-SiC_z DBR stopband. According to Comsol simulations, the cavity length reduces by increasing the number of layer pairs of the DBR or reducing geometry sizes. While the first method only results in a reduction below 1 µm, MEMS geometry sizes have a much greater effect. Standard-sized photolithography masks create MEMS-arm length and width of 145 nm and 60 nm, respectively. A new set of small-sized MEMS arms produces a length of 30 nm to 60 nm. Additionally, three widths of 20 nm to 30 nm investigate further influences on the shape of resulting MEMS. Accordingly, new photolithography masks are designed.

The predicted air-gaps could be found in the measured, fabricated filters with good agreement, consolidating the developed model and producing filters with much smaller cavity length. Additionally, mask redesign was used to reduce device footprint from 420 µm × 420 µm to 220 µm × 220 µm towards a possible introduction into industrial mass-production. The resulting air-gaps had a length of 1 µm to 4.6 µm. It increases the tuning range above 250 nm. It cannot be determined any further due to the limited range of the SOA source. Electro-thermal and substrate temperature tuning is possible here as well. One problem that occurs with these small-sized MEMS is the side-mode suppression ratio (SMSR), which only reaches values of up to 13 dB. Moreover, small-sized structures are much more vulnerable to photolithography misalignment and cause, for example, a tilted MEMS-DBR.

To further increase transmission linewidth, filters consisting of 8.5 layer-paired SiO_x-SiC_z DBR for higher reflectivity are produced. As predicted, the air-gap does reduce a bit, but more importantly, the linewidth narrows remarkably to a FWHM below 30 pm for a tuning range of more than 150 nm.

Another information acquired from Comsol simulations is the mechanical MEMS resonance, which ultimately limits maximum modulation speed for wavelength tuning. Due to the reduction in MEMS size, the first eigenfrequency is increased from 233 kHz to above 550 kHz. These speeds are useful for targeting applications where wavelength-sweeping speed is critical like spectroscopy or OCT.

Concerning fast MEMS actuation, electro-static displacement is investigated by adding a second electrode on the bottom DBR below the movable MEMS. It is necessary because electro-thermal actuation is limited by slow thermal processes which heat the MEMS. Consequently, wavelength modulation is limited to about 200 Hz. A DC actuation through the entire FSR needs a voltage of 350 V. It should be possible to reduce the voltage extensively by further refinement of electrode placement and additional MEMS-size reduction.

After proving that the MEMS-DBR technology works reliably, it is used to combine a tunable filter with an underlying PIN-photodiode by growing and structuring the devices with surface-micro-machining directly on a photodetector substrate for both SiO_x-SiN_y and SiO_x-SiC_z DBRs. Because photodiodes have contact pads on the surface, adjustments in the structuring of the sacrificial layer are necessary. Now, contacting pads are protected during DBR dry-etching. At the same time, it is also possible to etch deep enough to access them. Both tasks work successfully.

Selectivity towards neighboring channels of a 100 GHz-spaced DWDM system is tested with several DFB lasers coupled into a fiber simultaneously directed at the MEMS-DBR aperture with a collimator-lens system. Each laser can be identified with a photodiode responsivity of 0.75 A/W. The transmission through a SiO_x-SiC_z MEMS-DBR filter on a photodiode shows that the resonator itself is working correctly. However, the power transmitted is way below expectations. It can be caused by improper alignment of photolithography masks or coupling of light into the aperture. While SiC_z does have small absorption in the investigated region, the performance of a filter grown on a photodiode substrate should not differ much from a filter grown on a Si-wafer.

The last topic presented in this work is a proof-of-principle for SiO_x-SiC_z MEMS-DBR tunable VCSEL. With this, a half-VCSEL replaces the substrate on which a sacrificial layer and a MEMS-DBR are deposited and structured. The bottom DBR is buried within the half-VCSEL along with a strained quantum-well active region offering wide gain. Maximum output power of -12 dBm can be shown with a tuning range of up to 57 nm. The limiting factor now is a shift of DBR center-wavelength due to a reduction in deposition rate on a half-VCSEL in comparison to a Si-wafer. Consequently, the highest mirror reflectivity and maximum active material gain did not coincide at the same wavelength. Thus only a region from 1505 nm to 1562 nm does lase. Moreover, the SiC_z absorption limits the maximum output power. For standard-sized MEMS, processing issues destroyed the electrode and only substrate temperature tuning is possible. For both MEMS-sizes the temperature dependence is much smaller compared to a SiO_x-SiN_y MEMS-DBR VCSEL by more than one order of magnitude. Ultimately usage of a SiO_x-SiC_z MEMS-DBR results in a tunable VCSEL much less prone to environmental temperature influence, which should improve wavelength stability considerably.

Outlook

In the future, further improvements are possible. For SiO_x-SiC_z MEMS-DBR tunable filters, the next step is to connect high reflectivity mirrors with 8.5 or even more layer pairs with a smaller air-gap. This will result in a widely tunable ($> 250\,\text{nm}$) filter with narrow linewidth ($< 50\,\text{pm}$) across the tuning range. When processing small-sized filters, photolithography alignment accuracy is of utmost importance. A redesign of lithography masks is necessary to align it to previous structures easier, reducing the chance for misalignment. It can be done by introducing alignment markers or deliberately sacrifice a small number of devices to include inverse masks which offer a better view on overlapping structures. While redesigning masks, new MEMS sizes should be investigated with a special focus on increasing mechanical eigenfrequencies for higher modulation possibilities.

Fast wavelength tuning can be achieved with electro-static actuation. MEMS displacement is possible electro-statically, but AC modulation is not yet investigated. Here, the charging of dielectric layers might pose a challenge. However, if the modulation frequency is high enough, alternating charging of each electrode should negate this issue. Furthermore, the reduction of necessary actuation voltages is desired to make the devices compatible with more applications, where voltage supply is limited, for example. To do this, a reduction in electrode distance is necessary. It could be achieved by placing the top-electrode between the first couple of DBR layer pairs to keep it electrically isolated from each other, instead of depositing it on the top. DBR thickness is about 3 µm, so an electrode distance reduction of at least 2 µm should be feasible. A second approach includes reducing the MEMS mass by removing material from MEMS-arms, where no high reflectivity is required. Doing so inherently reduces the air-gap because the MEMS spring constant decreases with fewer layers. Thus, an optimum is to be determined.

For stable operation, it is unavoidable to introduce a packaging of the tunable device. It reduces MEMS vibration caused by temperature fluctuations in the environment. Within the package, a temperature-controlled and stabilized environment is necessary.

Other wavelength regimes should be possible further in the infrared region, for example around 2000 nm for other applications. Shorter wavelengths are not beneficial due to more considerable absorption losses of SiC_z layers. To further understand layer composition, Fourier-transform infrared-spectroscopy (FTIR) can be applied to single-layer depositions or DBR. It opens the possibility to see

which bonds are present within the layer and eventually use this information to adjust layer stress or refractive index directly with other deposition parameter sets.

MEMS-DBR tunable photodetectors work correctly but still have higher potential, especially with SiO_x-SiC_z MEMS-DBR. Here a deficient filter transmission is detected and needs to be investigated further. The transmission should not be much worse for a filter grown on a Si substrate than grown on a photodiode, as shown with SiO_x-SiN_y MEMS-DBR filters. Furthermore, for application of a tunable photodetector generally, it is required to know which wavelength is currently detected. Thus a means to determine this information during operation are desirable, either by improving MEMS displacement stability, which could enable look-up tables to connect wavelength information with a current or voltage value. Alternatively, by implementing an active current controller encompassing an etalon which can determine the direction of wavelength-shift and apply a countermeasure directly. Such a system is already presented for tunable SiO_x-SiN_y MEMS-DBR VCSEL.

A SiO_x-SiC_z MEMS-DBR VCSEL shows the most extensive potential for improvement. Due to a shift of DBR center-wavelength, only a part of active material gain can be used with the presented devices, and tuning range is limited. If the deposition is adjusted to counteract this shift by increasing designed wavelength and additionally add more layer pairs to increase the very high reflectivity stopband, the tuning range of SiO_x-SiN_y MEMS-DBR VCSEL should be exceeded. To increase power further, it is crucial here as well to optimize photolithography alignment accuracy for small-sized MEMS as well.

Symbols and Acronyms

α	Cavity losses
β_{sp}	Spontaneous emission factor
δL	Air-gap change
Δn	Refractive index step
$\Delta\lambda$	Wavelength shift
$\delta\lambda$	Transmission linewidth
$\Delta\nu$	Free spectral range in frequency
Δ	Phase (Ellipsometry)
ε_0	Vacuum permittivity
ε_R	Relative permittivity
ε	Axial strain
η_c	Net collection efficiency
η_d	Differential quantum efficiency
η_{ex}	External quantum efficiency
η_i	Internal quantum efficiency
η_r	Radiative efficiency
η	Quantum efficiency

Γ	Confinement factor
γ	Complex eigenvalue describing the losses after one round trip
λ_c	Center wavelength of DBR
$\lambda_{resonant}$	Resonant wavelength for a FPR with metal mirrors
λ	Wavelength
$\mathcal{F}$	Finesse
$\mathcal{M}$	Transfer matric
μ_R	Relative permeability of the medium
μ	Magnetic permeability of free space
ν_{PR}	Poisson's ratio
ν	Frequency
ω_0	Material dependent resonance frequency
ω	Photon frequency
Ψ	Elliptical polarization (Ellipsometry)
ρ	Radius of curvature
σ	Layer stress
τ	Decay constant
A_{MEMS}	MEMS electrode area
c_0	Speed of light in vacuum
c	Speed of light in material
d	Thickness
E_{SiC_z}	Young's Modulus

E_{a}	Acceptor defect energy
$E_{\mathrm{c,n}}$	conduction band lower edge n-type
$E_{\mathrm{c,p}}$	Conduction band lower edge p-type
E_{c}	Lower conduction band edge
E_{d}	Donor defect energy
E_{F}	Fermi energy
E_{g}	Bandgap
$E_{\mathrm{v,n}}$	valence band upper edge n-type semiconductor
$E_{\mathrm{v,p}}$	Valence band upper edge p-type semiconductor
E_{v}	Upper valence band edge
E	Energy
FSR	Free spectral range
F_{es}	Electro-static force
f	Random factor
g_{i}	g-factor of mirror i
g_{th}	Threshold gain
g	Gain per unit length
H	Magnetic field
I_{L}	Laser current
I_{MEMS}	MEMS-electrode current
I_{ph}	Photo current
I_{th}	Threshold current

I	Current
k	Extinction coefficient
L_0	Geometric length
L_{air}	Air-gap length
L_{arm}	Length of MEMS-arm
L_{CS}	Half-VCSEL SC thickness
L_{c}	Optical cavity length
L_{eff}	Effective length
L_{es}	Electro-static distance
$L_{\text{max T}}$	Length for highest transmission
L	Optical length
M	Number of layer pairs
m	Mode order
N_{above}	Carrier density above threshold
N_{el}	Electron density
N_{ph}	Photon density
N_{p}	Photon density
N_{th}	Threshold carrier density
n	Refractive index
P_{above}	Power above threshold
P_{below}	Power below threshold
P_{heat}	Heating power

P_{ICP}	ICP deposition power
P_{op}	Optical power
P_{RF}	RF deposition power
P	Characteristic layer matrix
p	Pressure
Q	Cavity Q-factor
q	Elementary charge
R_{aperture}	Radius of MEMS-electrode aperture
r_{dep}	Deposition rate
R_{disc}	Radius of MEMS disc
R_{MEMS}	Resistance of top-electrode
R_{PD}	Photodiode responsivity
R_{sp}	Spontaneous emission rate
R_{st}	Stimulated emission rate
R	Reflectivity
r	Fresnel reflection coefficient
TEM_{00}	Fundamental transversal electrical mode
TEM_{pl}	Transversal electrical modes
T_{S}	Substrate temperature
T_{T}	Tempering temperature
T	Transmittance
t	Fresnel transmission coefficient

U_{MEMS}	MEMS actuation voltage
V_{ar}	Active region volume
V_{bias}	PD bias voltage
v_{g}	Group velocity
V_{p}	Cavity volume occupied by photons
V	Cavity loss factor
W_{arm}	Width of MEMS-arm
w_{i}	Beam radius at mirror i
$(NH_4)_2Ce(NO_3)_5$	Cerium nitrate
$(NH_4)_2Ce(NO_3)_6$	Ceric ammonium nitrate
a-Si	Amorphous silicon
AC	Alternating current
Al	Aluminum
Ar	Argon
ARC	Anti reflective coating
Au	Gold
AWG	Arrayed waveguide grating
BCB	Benzocyclobutene
BTJ	Buried tunnel junction
C	Carbon
C_2F_6	Hexafluorethane
$C_2H_4O_2$	Acetic acid

CaF_2	Calcium Fluoride
$CBrF_3$	Bromtrifluoromethane
CCl_4	Carbon tetrachloride
CF_4	Tetrafluoromethane
CH_3OOH_2	Acetate
CH_4	Methane
CHF_3	Fluoroform
Cl_2	Clorine
CO	Carbon monoxid
CO_2	Carbon dioxide
Cr	Chrome
$Cr(NO_3)_3$	Chromium(III) nitrate
CVD	Chemical vapor deposition
DBR	Distributed Bragg reflector
DC	Direct current
DFB	Distributed feedback
DWDM	Dense wavelength division multiplexing
EF	Eigenfrequency
F	Fluor
$FeCL_3$	Iron (III) chloride
FPR	Fabry-Pérot resonator
FSR	Free spectral range

FTIR	Fourier transform infrared spectroscopy
FWHM	Full width at half maximum
Ge	Germanium
H	Hydrogen
H_2O	Water
H_2SO_4	Sulfuric acid
HCl	Hydrochlorid acid
$HClO_4$	Perchloric acid
He	Helium
HF	Hydrofluoric acid
HNO_3	Nitric acid
IC	Integrated Circuit
ICP	Inductively coupled plasma
InGaAs	Indium gallium arsenide
InP	Indium phosphide
KI	Kalium iodide
LED	Light emitting diode
MEMS	Microelectromechanical system
N_2	Nitrogen
N_2H_4	Hydrazine
N_2O	Nitrous oxide
NEMS	Nanoelectromechanical system

NH_3	Ammonia
NH_4F	Ammonium fluoride
Ni	Nickel
$Ni(NO_3)_2$	Nickel nitrate
NIR	Near infrared region
NMP	N-Methyl-2-pyrrolidone
NO	Nitrogen oxide
NOCl	Nitrosyl chloride
O_2	Oxygen
OCT	Optical coherence tomography
OSA	Optical spectrum analyzer
PD	Photodiode
PECVD	Plasma enhanced chemical vapor deposition
pin-PD	Photodiode with intrinsic layer between pn-junction
RF	Radio frequency
RIE	Reactive ion etching
ROC	Radius of curvature
rt	Room temperature
RTA	Rapid thermal anneal
SC	Semiconductor
SF_6	Sulfur hexafluoride
Si	Silicon

Si_3N_4	Silicon nitride
SiC_4	Silicon tetrachloride
SiC_z	Amorphous Silicon carbide
SiF_4	Silicon tetrafluoride
SiH_4	Silane
SiN_y	Amorphous silicon nitride
SiO_2	Silicon dioxide
SiO_x	Amorphous silicon oxide
SMSR	Side mode suppression ratio
SOA	Semiconductor optical amplifier
TEC	Temperature controller, Peltier Module
TFG	Nickel etchant, Transene
Ti	Titanium
$Ti(OC_3H_7)_4$	Titanium tetra-isopropoxide
TiO_2	Titanium dioxide
TL	Tauc-Lorentz
TMM	Transfer matrix model
UV	Ultraviolet
VCSEL	Vertical cavity surface emitting laser
VIS	Visible range
ZnS	Zinc sulfite

Bibliography

[1] J. Bullot and M. P. Schmidt. "Physics of Amorphous Silicon-Carbon Alloys". In: *Physica Status Solidi (B) Basic Research* 143 (1987), pages 345–418. DOI: 10.1002/pssb.2221430202.

[2] BYU. *Nickel Etching*. URL: https://cleanroom.byu.edu/wet_etch (visited on 09/10/2019).

[3] Pathros Cardenas and David Tung. *Plasma Enhanced Chemical Vapor Deposition (PECVD)*. URL: http://classweb.ece.umd.edu/enee416.F2007/GroupActivities/Presentation5.pdf (visited on 09/13/2019).

[4] Julijan Cesar, Franko Küppers, and Thomas Kusserow. "Weit abstimmbare optische Filter um 1550 nm basierend auf SiOx-SiCz MEMS-DBR". In: *Deutsche Gesellschaft für angewandte Optik*. Darmstadt, Germany, 2019. URL: https://www.dgao-proceedings.de/abstract/abstract_only.php?id=2509.

[5] Julijan Cesar, Sujoy Paul, Christian Gierl, and Franko Küppers. "Optimierung der Abscheideparameter für PECVD Prozesse durch Messung der optischen Eigenschaften der Schichten". In: *SENTECH Dünnschicht-Messtechnik Seminar*. Stuttgart, Germany, 2015.

[6] Julijan Cesar, Sujoy Paul, Mohammad Tanvir Haidar, Brian Corbett, A. Chipouline, and Franko Küppers. "Surface Micromachined MEMS-Tunable PIN-Photodiodes around 1550-nm". In: *Conference on Lasers and Electro-Optics*. San Jose, USA, 2017. DOI: 10.1364/CLEO_SI.2017.STu1N.7.

[7] Julijan Cesar, Sujoy Paul, Mohammad Tanvir Haidar, Mohammadreza Malekizandi, Benjamin Kögel, Christian Neumeyr, Markus Ortsiefer, and Franko Küppers. "Thermal Characteristics, Linewidth and Far-field Measurements on High Speed Widely Tunable MEMS-VCSEL". In: *European VCSEL Day*. Darmstadt, Germany, 2016.

[8] Julijan Cesar, Sujoy Paul, Franko Küppers, Benjamin Kögel, Christoph Gréus, Christian Neumeyr, Markus Ortsiefer, Irfan Ibrahim, Henning Schmidt, Jörg Schmidt, and Michael Eiselt. "Weit abstimmbare Sender (MEMS VCSEL) bei 1550 nm für photonische Netze". In: *ITG-Fachtagung Photonische Netze*. Leipzig, Germany, 2016.

[9] Julijan Cesar, Sujoy Paul, Franko Küppers, and Thomas Kusserow. "SiC-SiO-MEMS-DBR-based widely tunable optical filters around 1550 nm with narrow FWHM". In: *Conference on Lasers & Electro-Optics / Europe and the European Quantum Electronics Conference*. Munich, Germany, 2019. DOI: 10.1109/CLEOE-EQEC.2019.8873055.

[10] A. Chipouline, V. S. Lyubopytov, T. von Lerber, M. Lassas, S. Paul, M. F. Schumann, J. Cesar, M. Wegener, and F. Küppers. "Applications of VCSELs in optical transmission lines and vortex generation". In: *ICLO*. St. Petersburg, Russia, 2016. URL: https://tubiblio.ulb.tu-darmstadt.de/85814/.

[11] W. J. Choyke. "Optical Properties of Polytypes of SiC: Intraband Absorption, and Luminescence of Nitrogen-Extinction Complexes". In: *Silicon Carbide-1968*. Edited by H. K. Henisch and R. Roy. Pergamon, 1969, pages 141–152. DOI: 10.1016/B978-0-08-006768-1.50018-8.

[12] L. A. Coldren and S. W. Corzine. *Diode Lasers and Photonic Integrated Circuits*. Edited by Kai Chang. Wiley Series In Microwave and Optical Engineering, 1995. ISBN: 0-471-11875-3.

[13] Garrett D. Cole, E. Staffan Björlin, Qi Chen, Chung Yeung Chan, Shaomin Wu, Chad S. Wang, Noel C. MacDonald, and John E. Bowers. "MEMS-tunable vertical-cavity SOAs". In: *IEEE Journal of Quantum Electronics* 41.3 (2005), pages 390–407. DOI: 10.1109/JQE.2004.841496.

[14] A. Convertino, A. Valentini, P. V. Giugno, and R. Cingolani. "Infrared distributed Bragg reflectors based on amorphous SiC/SiO2 heterostructures". In: *Applied Physics Letters* 70.21 (1997), page 2799. DOI: 10.1063/1.119063.

[15] Frank S. jr. Crawford. *Waves*. Volume 3. 1986. URL: http://archive.org/details/Waves_371.

[16] C. De Bernardi, M. Meliga, S. Morasca, C. Rigo, B. Sordo, and A. Stano. "Refractive indices of InGaAlAs grown by molecular beam epitaxy". In: *Journal of Applied Physics* 68.12 (Dec. 1990), pages 6513–6514. DOI: 10.1063/1.346853.

[17] J. R. DeVore. "Refractive Indices of Rutile and Sphalerite". In: *Journal of the Optical Society of America* 41.6 (1951), pages 416–419. DOI: 10.1364/JOSA.41.000416.

[18] M.A. El Khakani, M. Chaker, A. Jean, S. Boily, J.C. Kieffer, M.E. O'Hern, M.F. Ravet, and F. Rousseaux. "Hardness and Young's modulus of amorphous a-SiC thin films determined by nanoindentation and bulge tests". In: *Journal of Materials Research* 9.01 (1994), pages 96–103. DOI: 10.1557/JMR.1994.0096.

[19] Giovanni Esteves, Scott D. Habermehl, Peggy J. Clews, Chanju Fritch, and Benjamin A. Griffin. "AlN/SiC MEMS for High-Temperature Applications". In: *Journal of Microelectromechanical Systems* 28.5 (2019), pages 859–864. DOI: 10.1109/JMEMS.2019.2923919.

[20] A. G. Fox and Tingye Li. "Resonant Modes in a Maser Interferometer". In: *Bell. Syst. Tech. J.* 40 (1961). DOI: 10.1002/j.1538-7305.1961.tb01625.x.

[21] Christian Gierl. "Mikromechanisch weit abstimmbare Oberflächen-emittierende Laser mit Vertikalresonator". PhD thesis. Technical University of Darmstadt, 2012.

[22] Christian Gierl, Karolina Zogal, Sujoy Paul, and Franko Küppers. "Tunable MEMS-VCSEL with >140-nm tuning range using tuning range using SiO2/SiC-based MEMS-DBR". In: *Vertical-Cavity Surface-Emitting Lasers XVIII*. Volume 9001. International Society for Optics and Photonics, Feb. 2014. DOI: 10.1117/12.2041280.

[23] R. Groth and E. Kauer. "Absorption freier Ladungsträger in α-SiC-Kristallen". In: *Physica Status Solidi (B)* 1.5 (1961), pages 445–450. DOI: 10.1002/pssb.19610010504.

[24] M. T. Haidar, E. Polat, S. Paul, J. Cesar, C. Gierl, A. Chipouline, and F. Küppers. "SOA-Based Tunable Fiber Ring Laser With Intracavity MEMS-Tunable Fabry-Pérot Filter". In: *Conference on Lasers and Electro-Optics*. San Jose, USA: Optical Society of America, 2016. DOI: 10.1364/CLEO_SI.2016.SM2P.7.

[25] M. T. Haidar, S. Preu, J. Cesar, S. Paul, A. S. Hajo, C. Neumeyr, H. Maune, and F. Küppers. "Systematic characterization of a 1550 nm microelectromechanical (MEMS)-tunable vertical-cavity surface-emitting laser (VCSEL) with 7.92 THz tuning range for terahertz photomixing systems". In: *Journal of Applied Physics* 123.2 (2018). ISSN: 0021-8979. DOI: 10.1063/1.5003147.

[26] Mohammad Tanvir Haidar, Sascha Preu, Sujoy Paul, Christian Gierl, Julijan Cesar, Ali Emsia, and Franko Küppers. "Widely tunable telecom MEMS-VCSEL for terahertz photomixing". In: *Optics Letters* 40.19 (2015). Publisher: Optical Society of America, pages 4428–4431. DOI: 10.1364/OL.40.004428.

[27] Hubert Halbritter, Chenna Dhanavantri, Martin Strassner, Amer Tarraf, Michael Aziz, Frank Riemenschneider, Sandro Syguda, B. R. Singh, Isabelle Sagnes, and Peter Meissner. "Tunable and wavelength-selective PIN diodes". In: *Photonics: Design, Technology, and Packaging*. Volume 5277. International Society for Optics and Photonics, 2004, pages 129–137. DOI: 10.1117/12.522044.

[28] G. Hancock, L. Lanyi, J. P. Sucksmith, and B. K. Woodcock. "Atoms, radicals and ions observed in plasmas - Their gas and surface chemistry". In: *Pure and Applied Chemistry* 66.6 (1994), pages 1207–1214. DOI: 10.1351/pac199466061207.

[29] Eugene Hecht. *Optik*. Oldenburg Wissenschaftsverlag GmbH, 2005.

[30] Norman Hodgson and Horst Weber. *Optical Resonators - Fundamentals, Advanced Concepts and Applications*. Springer, 1997. ISBN: 3-540-76137-3.

[31] Rongdun Hong, Jun Huang, Xiaping Chen, Yi Zhou, Dayi Liu, and Zhengyun Wu. "Ellipsometry, FTIR, Raman and X-Ray Spectroscopy Analysis of PECVD a-Si1-xCx:H Film". In: *Spectroscopy Letters* 43 (2010), pages 298–305. DOI: 10.1080/00387010903348276.

[32] Ciprian Iliescu and Bangtao Chen. "Thick and low-stress PECVD amorphous silicon for MEMS applications". In: *Journal of Micromechanics and Microengineering* 18.1 (2007). DOI: 10.1088/0960-1317/18/1/015024.

[33] Ciprian Iliescu and Daniel P Poenar. "PECVD Amorphous Silicon Carbide (α-SiC) Layers for MEMS Applications". In: (2013). tex.ids: Iliescu2012. DOI: 10.5772/51224.

[34] G. E. Jellison. "Data analysis for spectroscopic ellipsometry". In: *Thin Solid Films* 234.1 (1993), pages 416–422. DOI: 10.1016/0040-6090(93)90298-4.

[35] Liudi Jiang and R. Cheung. "A Review of silicon carbide development in MEMS applications". In: *Thin Solid Films* (2009), pages 225–240. DOI: 10.1504/IJCMSSE.2009.027484.

[36] Liudi Jiang, R. Cheung, J. Hedley, M. Hassan, A. J. Harris, J. S. Burdess, M. Mehregany, and C. A. Zorman. "SiC cantilever resonators with electrothermal actuation". In: *Sensors and Actuators A: Physical* 128.2 (2006), pages 376–386. DOI: 10.1016/j.sna.2006.01.045.

[37] Michael Köhler. *Ätzverfahren für die Mikrotechnik*. Deutsch. Weinheim: WILEY-VCH, 1998. ISBN: 3-527-28869-4.

[38] Mitsuharu Konuma. *Film Deposition by Plasma Techniques*. Springer Series on Atomic, Optical, and Plasma Physics. Berlin Heidelberg: Springer-Verlag, 1992. DOI: 10.1007/978-3-642-84511-6.

[39] Yue Kuo. "Reactive Ion Etching of PECVD Amorphous Silicon and Silicon Nitride Thin Films with Fluorocarbon Gases". In: *Journal of The Electrochemical Society* 137.4 (1990), pages 1235–1239. DOI: 10.1149/1.2086638.

[40] Juan I. Larruquert, Antonio P. Pérez-Marín, Sergio García-Cortés, Luis Rodríguez-de Marcos, José A. Aznárez, and José A. Méndez. "Self-consistent optical constants of SiC thin films". In: *Journal of the Optical Society of America* 28.11 (2011), pages 2340–2345. DOI: 10.1364/JOSAA.28.002340.

[41] Juan Larruquert and Ritva Keski-Kuha. "Reflectance Measurements and Optical Constants in the Extreme Ultraviolet for Thin Films of Ion-Beam-Deposited SiC, Mo, Mg_2Si, and InSb and of Evaporated Cr". In: *Applied Optics* 39 (2000), pages 2772–81. DOI: 10.1364/AO.39.002772.

[42] Vladimir S Lyubopytov, Alexey P Porfirev, Stansilav O Gurbatov, Sujoy Paul, Martin F Schumann, Julijan Cesar, Mohammadreza Malekizandi, Mohammad T Haidar, Martin Wegener, Arkadi Chipouline, and Franko Küppers. "Simultaneous wavelength and orbital angular momentum demultiplexing using tunable MEMS-based Fabry-Perot filter". In: *Optics Express* 25.9 (2017), pages 9634–9646. DOI: 10.1364/OE.25.009634.

[43] Vladimir Lyubopytov, Aleksey Porfirev, Stanislav Gurbatov, Sujoy Paul, Martin Schumann, Julijan Cesar, Mohammadreza Malekizandi, Mohammad Tanvir Haidar, Martin Wegener, Arkadi Chipouline, and Franko Küppers. "MEMS-based wavelength and orbital angular momentum demultiplexer for on-chip applications". In: *Conference on Lasers and Electro-Optics/Europe and European Quantum Electronics Conference*. Munich, Germany, 2017. DOI: 10.1109/CLEOE-EQEC.2017.8087118.

[44] Vladimir Lyubopytov, Aleksey Porfirev, Stanislav Gurbatov, Martin Schumann, Martin Wegener, Mohammad Tanvir Haidar, Mohammadreza Malekizandi, Julijan Cesar, Sujoy Paul, Arkadi Chipouline, and Franko Küppers. "Orbital Angular Momentum And Wavelength Demultiplexing Using Tunable MEMS-based Fabry-Pérot Filter Integrated With Spiral Phase Plate". In: *Pacific Rim Conference on Lasers and Electro-Optics*. Singapore, 2017.

[45] M. Mehregany, C. A. Zorman, and N. Rajan and. "Silicon carbide MEMS for harsh environments". In: *Proceedings of the IEEE* 86.8 (1998), pages 1594–1609. DOI: 10.1109/5.704265.

[46] Microchemicals. *Chromium Etching*. URL: https://www.microchemicals.eu/technical_information/chromium_etching.pdf.

[47] Microchemicals. *Gold Etching*. URL: https://www.microchemicals.eu/technical_information/gold_etching.pdf.

[48] Microchemicals. *Wet-chemical etching of metals*. URL: https://www.microch%20emicals.com/technical_information/wet_etching_metals_al_au_cu_cr_ni_ti_ag.pdf.

[49] Microchemicals. *Wet-chemical etching of silicon and SiO2*. URL: https://www.microchemicals.eu/technical_information/silicon_etching.pdf.

[50] NMP. "N-Methylpyrrolidone (NMP)". en. In: (June 2014), page 6. URL: https://www.cdph.ca.gov/Programs/CCDPHP/DEODC/OHB/HESIS/CDPH%20Document%20Library/nmp.pdf.

[51] Markus Ortsiefer, Christoph Gréus, Jürgen Rosskopf, Sujoy Paul, Julijan Cesar, Christian Neumeyr, and Franko Küppers. "Ultra-Wide Mode-Hop-Free Tuning of Long-Wavelength MEMS VCSELs". In: *International WORKshop on Infrared Technologies*. Olching, Germany, 2016.

[52] Sujoy Paul. "Surface Micromachined Widely Tunable VCSEL and OAM-Filter for Optical Data Transmission". PhD Thesis. Technical University of Darmstadt, 2018.

[53] Sujoy Paul, Julijan Cesar, Mohammad Tanvir Haidar, Christian Gierl, Benjamin Koegel, Christian Neumeyr, Markus Ortsiefer, and Franko Küppers. "Ultra wide mode-hop free tuning around 1550-nm telecom wavelength using high-speed MEMS-VCSELs". In: 2015. DOI: 10.1109/MOC.2015.7416499.

[54] Sujoy Paul, Julijan Cesar, and Franko Küppers. "Widely Tunable MEMS VCSEL at 1550-nm". In: *European VCSEL Day*. Cardiff, Wales, 2017.

[55] Sujoy Paul, Julijan Cesar, Mohammadreza Malekizandi, Mohammad Tanvir Haidar, Christian Neumeyr, Markus Ortsiefer, and Franko Küppers. "Towards a SFP+ module for WDM applications using an ultra-widely-tunable high-speed MEMS-VCSEL". In: *SPIE Photonics West*. San Francisco, USA, 2017. DOI: 10.1117/12.2252059.

[56] Sujoy Paul, Christian Gierl, Julijan Cesar, Franko Küppers, Benjamin Kögel, Jürgen Rosskopf, Max Görblich, You Xu, Christian Neumeyr, and Markus Ortsiefer. "7-GHz Small-signal Modulation Response of a Surface Micromachined BCB MEMS VCSEL with > 50-nm Continuous Tuning". In: *Conference on Lasers & Electro-Optics / Europe and the European Quantum Electronics Conference*. Munich, Germany, 2015. ISBN: 978-1-4673-7475-0.

[57] Sujoy Paul, Christian Gierl, Julijan Cesar, Quang Trung Le, Mohammadreza Malekizandi, Benjamin Kögel, Christian Neumeyr, Markus Ortsiefer, and Franko Küppers. "10-Gb/s direct modulation of widely tunable 1550-nm MEMS VCSEL". In: *IEEE Journal on Selected Topics in Quantum Electronics* 21.6 (2015). DOI: 10.1109/JSTQE.2015.2418218.

[58] Sujoy Paul, Christian Gierl, Julijan Cesar, Quang Trung Le, Mohammadreza Malekizandi, Franko Küppers, Benjamin Kögel, Jürgen Rosskopf, Christoph Gréus, Markus Görblich, Yan Xu, Christian Neumeyr, and Markus Ortsiefer. "High Speed Surface Micromachined MEMS Tunable VCSEL for Telecom Wavelengths". In: *Conference on Lasers and Electro-Optics*. 2015. DOI: 10.1364/CLEO_AT.2015.AM3K.1.

[59] Sujoy Paul, Mohammad Tanvir Haidar, Julijan Cesar, Mohammadreza Malekizandi, Kögel Benjamin, Christian Neumeyr, Markus Ortsiefer, and Franko Küppers. "Far-field, linewidth and thermal characteristics of a high-speed 1550-nm MEMS tunable VCSEL". In: *Optics Express* 23.5 (2015), pages 6803–6808. DOI: 10.1364/OE.24.013142.

[60] Sujoy Paul, Niels Heermeier, Mohammadreza Malekizandi, Julijan Cesar, Mohammad Tanvir Haidar, Christoph Gréus, Christian Neumeyr, and Franko Küppers. "10-Gbps Direct On-Off-Keying Modulation across 85-nm Continuous Tuning Range Using Telecom MEMS-VCSEL". In: *Conference on Lasers & Electro-Optics / Europe and the European Quantum Electronics Conference*. Munich, Germany, 2017. DOI: 10.1109/CLEOE-EQEC.2017.8086351.

[61] Sujoy Paul, Vladimir S Lyubopytov, Martin F Schumann, Julijan Cesar, Arkadi Chipouline, Martin Wegener, and Franko Küppers. "Wavelength-selective orbital-angular-momentum beam generation using MEMS tunable Fabry-Perot filter". In: *Optics Letters* (2016), pages 3–6. DOI: 10.1364/OL.41.003249.

[62] Sujoy Paul, Vladimir Lyubopytov, Arkadi Chipouline, Martin Schumann, Julijan Cesar, Mohammadreza Malekizandi, Mohammad Tanvir Haidar, Martin Wegener, and Frank Küppers. "Vortex-MEMS filters for wavelength-

selective orbital-angular-momentum beam generation". In: *SPIE Photonics West*. San Francisco, USA, 2017. DOI: 10.1117/12.2252494.

[63] G. D. Pettit and W. J. Turner. "Refractive Index of InP". In: *Journal of Applied Physics* 36.6 (1965), pages 2081–2081. DOI: 10.1063/1.1714410.

[64] D. T. Pierce and W. E. Spicer. "Electronic Structure of Amorphous Si from Photoemission and Optical Studies". In: *Physical Review B* 5.8 (1972), pages 3017–3029. DOI: 10.1103/PhysRevB.5.3017.

[65] G. Rehder and M.N.P. Carreno. "PECVD a-Sic:H Young's modulus obtained by MEMS resonant frequency". In: *Journal of Non-Crystalline Solids* 354.19-25 (2008), pages 2359–2364. DOI: 10.1016/j.jnoncrysol.2007.10.079.

[66] Alan Rogers. *Essentials of Photonics*. CRC Press, 2009.

[67] Alfred J. van Roosmalen. "Review: dry etching of silicon oxide". In: *Vacuum* 34.3 (1984), pages 429–436. DOI: 10.1016/0042-207X(84)90079-4.

[68] Swagato Sarkar, Vaibhav Gupta, Mohit Kumar, Jonas Schubert, Patrick T. Probst, Joby Joseph, and Tobias A.F. König. "Hybridized Guided-Mode Resonances via Colloidal Plasmonic Self-Assembled Grating". In: *ACS Applied Materials & Interfaces* 11.14 (2019), pages 13752–13760. DOI: 10.1021/acsami.8b20535.

[69] Pasqualina M. Sarro. "Silicon carbide as a new MEMS technology". In: *Sensors and Actuators, A: Physical* 82 (2000), pages 210–218. DOI: 10.1016/S0924-4247(99)00335-0.

[70] MEL Science. *Oxidation states of nickel and reactions with it*. en. URL: https://melscience.com/US-en/articles/oxidation-states-nickel-and-reactions-it/ (visited on 09/10/2019).

[71] Thomas Siefke, Stefanie Kroker, Kristin Pfeiffer, Oliver Puffky, Kay Dietrich, Daniel Franta, Ivan Ohlídal, Adriana Szeghalmi, Ernst-Bernhard Kley, and Andreas Tünnermann. "Materials Pushing the Application Limits of Wire Grid Polarizers further into the Deep Ultraviolet Spectral Range". In: *Advanced Optical Materials* 4.11 (2016), pages 1780–1786. DOI: 10.1002/adom.201600250.

[72] S. Singh, J. R. Potopowicz, L. G. Van Uitert, and S. H. Wemple. "Nonlinear Optical Properties of Hexagonal Silicon Carbide". In: *Applied Physics Letters* 19.3 (1971), pages 53–56. DOI: 10.1063/1.1653819.

[73] F Tayeboun, R. Naoum, and F. Salah-Belkhodja. "Design of tunable filter by Kerr effect used in optical communications". In: *Electronic Journal Technical Acoustics* (2004).

[74] Christoph Wagner, Annika Dochhan, Michael Eiselt, Klaus Grobe, Markus Ortsiefer, Christoph Gréus, Christian Neumeyr, Sujoy Paul, Julijan Cesar, Franko Küppers, Vegas Olmos, Juan Jose, and Idelfonso Tafur Monroy. "26-Gbps DMT Transmission using Full C-band Tunable VCSEL for Converged PONs". In: *IEEE Photonics Technology Letters* (2017). DOI: 10.1109/LPT.2017.2710323.

[75] Christoph Wagner, Jim Zou, Markus Ortsiefer, Christoph Greus, Chritian Neumayr, Klaus Grobe, Michael Eiselt, Sujoy Paul, Julijan Cesar, Franko Küppers, Juan Jose Vegas Olmos, and Idelfonso Tafur Monroy. "Full C-band Tunable MEMS-VCSEL for Next Generation G.metro Mobile Front- and Backhauling". In: *Optical Fiber Communication Conference*. Los Angeles, USA, 2017. DOI: 10.1364/OFC.2017.W2A.27.

[76] Shunchong Wang, Minjie Zhan, Gang Wang, Hongwen Xuan, Wei Zhang, Chunjun Liu, Chunhua Xu, Yu Liu, Zhiyi Wei, and Xiaolong Chen. "4H-SiC: a new nonlinear material for midinfrared lasers". In: *Laser & Photonics Reviews* 7.5 (2013), pages 831–838. DOI: 10.1002/lpor.201300068.

[77] Yanqi Wang. "Model Calculations and Implementation of Filters and Hybrid Green VCSELs based on Optical Thin Film Stacks". PhD thesis. Universität Kassel, 2010.

[78] Kun Xue, Li-Sha Niu, and Hui-Ji Shi. "Mechanical Properties of Amorphous Silicon Carbide". In: *Silicon Carbide* (2011), page 23. DOI: 10.5772/21689.

[79] Jiro Yota. "Effects of Deposition Method of PECVD Silicon Nitride as MIM Capacitor Dielectric for GaAs HBT Technology". In: Montreal, QC, Canada, 2011, pages 229–240. DOI: 10.1149/1.3572286.

Own publications

[4] Julijan Cesar, Franko Küppers, and Thomas Kusserow. "Weit abstimmbare optische Filter um 1550 nm basierend auf SiOx-SiCz MEMS-DBR". In: *Deutsche Gesellschaft für angewandte Optik*. Darmstadt, Germany, 2019. URL: https://www.dgao-proceedings.de/abstract/abstract_only.php?id=2509.

[5] Julijan Cesar, Sujoy Paul, Christian Gierl, and Franko Küppers. "Optimierung der Abscheideparameter für PECVD Prozesse durch Messung der optischen Eigenschaften der Schichten". In: *SENTECH Dünnschicht-Messtechnik Seminar*. Stuttgart, Germany, 2015.

[6] Julijan Cesar, Sujoy Paul, Mohammad Tanvir Haidar, Brian Corbett, A. Chipouline, and Franko Küppers. "Surface Micromachined MEMS-Tunable PIN-Photodiodes around 1550-nm". In: *Conference on Lasers and Electro-Optics*. San Jose, USA, 2017. DOI: 10.1364/CLEO_SI.2017.STu1N.7.

[7] Julijan Cesar, Sujoy Paul, Mohammad Tanvir Haidar, Mohammadreza Malekizandi, Benjamin Kögel, Christian Neumeyr, Markus Ortsiefer, and Franko Küppers. "Thermal Characteristics, Linewidth and Far-field Measurements on High Speed Widely Tunable MEMS-VCSEL". In: *European VCSEL Day*. Darmstadt, Germany, 2016.

[8] Julijan Cesar, Sujoy Paul, Franko Küppers, Benjamin Kögel, Christoph Gréus, Christian Neumeyr, Markus Ortsiefer, Irfan Ibrahim, Henning Schmidt, Jörg Schmidt, and Michael Eiselt. "Weit abstimmbare Sender (MEMS VCSEL) bei 1550 nm für photonische Netze". In: *ITG-Fachtagung Photonische Netze*. Leipzig, Germany, 2016.

[9] Julijan Cesar, Sujoy Paul, Franko Küppers, and Thomas Kusserow. "SiC-SiO-MEMS-DBR-based widely tunable optical filters around 1550 nm with narrow FWHM". In: *Conference on Lasers & Electro-Optics / Europe and the European Quantum Electronics Conference*. Munich, Germany, 2019. DOI: 10.1109/CLEOE-EQEC.2019.8873055.

[10] A. Chipouline, V. S. Lyubopytov, T. von Lerber, M. Lassas, S. Paul, M. F. Schumann, J. Cesar, M. Wegener, and F. Küppers. "Applications of VCSELs in optical transmission lines and vortex generation". In: *ICLO*. St. Petersburg, Russia, 2016. URL: https://tubiblio.ulb.tu-darmstadt.de/85814/.

[24] M. T. Haidar, E. Polat, S. Paul, J. Cesar, C. Gierl, A. Chipouline, and F. Küppers. "SOA-Based Tunable Fiber Ring Laser With Intracavity MEMS-Tunable Fabry-Pérot Filter". In: *Conference on Lasers and Electro-Optics*. San Jose, USA: Optical Society of America, 2016. DOI: 10.1364/CLEO_SI.2016.SM2P.7.

[25] M. T. Haidar, S. Preu, J. Cesar, S. Paul, A. S. Hajo, C. Neumeyr, H. Maune, and F. Küppers. "Systematic characterization of a 1550 nm microelectromechanical (MEMS)-tunable vertical-cavity surface-emitting laser (VCSEL) with 7.92 THz tuning range for terahertz photomixing systems". In: *Journal of Applied Physics* 123.2 (2018). ISSN: 0021-8979. DOI: 10.1063/1.5003147.

[26] Mohammad Tanvir Haidar, Sascha Preu, Sujoy Paul, Christian Gierl, Julijan Cesar, Ali Emsia, and Franko Küppers. "Widely tunable telecom MEMS-VCSEL for terahertz photomixing". In: *Optics Letters* 40.19 (2015). Publisher: Optical Society of America, pages 4428–4431. DOI: 10.1364/OL.40.004428.

[42] Vladimir S Lyubopytov, Alexey P Porfirev, Stansilav O Gurbatov, Sujoy Paul, Martin F Schumann, Julijan Cesar, Mohammadreza Malekizandi, Mohammad T Haidar, Martin Wegener, Arkadi Chipouline, and Franko Küppers. "Simultaneous wavelength and orbital angular momentum demultiplexing using tunable MEMS-based Fabry-Perot filter". In: *Optics Express* 25.9 (2017), pages 9634–9646. DOI: 10.1364/OE.25.009634.

[43] Vladimir Lyubopytov, Aleksey Porfirev, Stanislav Gurbatov, Sujoy Paul, Martin Schumann, Julijan Cesar, Mohammadreza Malekizandi, Mohammad Tanvir Haidar, Martin Wegener, Arkadi Chipouline, and Franko Küppers. "MEMS-based wavelength and orbital angular momentum demultiplexer for on-chip applications". In: *Conference on Lasers and Electro-Optics/Europe and European Quantum Electronics Conference*. Munich, Germany, 2017. DOI: 10.1109/CLEOE-EQEC.2017.8087118.

[44] Vladimir Lyubopytov, Aleksey Porfirev, Stanislav Gurbatov, Martin Schumann, Martin Wegener, Mohammad Tanvir Haidar, Mohammadreza Malekizandi, Julijan Cesar, Sujoy Paul, Arkadi Chipouline, and Franko Küppers. "Orbital Angular Momentum And Wavelength Demultiplexing Using Tunable MEMS-based Fabry-Pérot Filter Integrated With Spiral

Phase Plate". In: *Pacific Rim Conference on Lasers and Electro-Optics*. Singapore, 2017.

[51] Markus Ortsiefer, Christoph Gréus, Jürgen Rosskopf, Sujoy Paul, Julijan Cesar, Christian Neumeyr, and Franko Küppers. "Ultra-Wide Mode-Hop-Free Tuning of Long-Wavelength MEMS VCSELs". In: *International WORKshop on Infrared Technologies*. Olching, Germany, 2016.

[53] Sujoy Paul, Julijan Cesar, Mohammad Tanvir Haidar, Christian Gierl, Benjamin Koegel, Christian Neumeyr, Markus Ortsiefer, and Franko Küppers. "Ultra wide mode-hop free tuning around 1550-nm telecom wavelength using high-speed MEMS-VCSELs". In: 2015. DOI: 10.1109/MOC.2015.7416499.

[54] Sujoy Paul, Julijan Cesar, and Franko Küppers. "Widely Tunable MEMS VCSEL at 1550-nm". In: *European VCSEL Day*. Cardiff, Wales, 2017.

[55] Sujoy Paul, Julijan Cesar, Mohammadreza Malekizandi, Mohammad Tanvir Haidar, Christian Neumeyr, Markus Ortsiefer, and Franko Küppers. "Towards a SFP+ module for WDM applications using an ultra-widely-tunable high-speed MEMS-VCSEL". In: *SPIE Photonics West*. San Francisco, USA, 2017. DOI: 10.1117/12.2252059.

[56] Sujoy Paul, Christian Gierl, Julijan Cesar, Franko Küppers, Benjamin Kögel, Jürgen Rosskopf, Max Görblich, You Xu, Christian Neumeyr, and Markus Ortsiefer. "7-GHz Small-signal Modulation Response of a Surface Micromachined BCB MEMS VCSEL with > 50-nm Continuous Tuning". In: *Conference on Lasers & Electro-Optics / Europe and the European Quantum Electronics Conference*. Munich, Germany, 2015. ISBN: 978-1-4673-7475-0.

[57] Sujoy Paul, Christian Gierl, Julijan Cesar, Quang Trung Le, Mohammadreza Malekizandi, Benjamin Kögel, Christian Neumeyr, Markus Ortsiefer, and Franko Küppers. "10-Gb/s direct modulation of widely tunable 1550-nm MEMS VCSEL". In: *IEEE Journal on Selected Topics in Quantum Electronics* 21.6 (2015). DOI: 10.1109/JSTQE.2015.2418218.

[58] Sujoy Paul, Christian Gierl, Julijan Cesar, Quang Trung Le, Mohammadreza Malekizandi, Franko Küppers, Benjamin Kögel, Jürgen Rosskopf, Christoph Gréus, Markus Görblich, Yan Xu, Christian Neumeyr, and Markus Ortsiefer. "High Speed Surface Micromachined MEMS Tunable VCSEL for Telecom Wavelengths". In: *Conference on Lasers and Electro-Optics*. 2015. DOI: 10.1364/CLEO_AT.2015.AM3K.1.

[59] Sujoy Paul, Mohammad Tanvir Haidar, Julijan Cesar, Mohammadreza Malekizandi, Kögel Benjamin, Christian Neumeyr, Markus Ortsiefer, and Franko Küppers. "Far-field, linewidth and thermal characteristics of a high-speed 1550-nm MEMS tunable VCSEL". In: *Optics Express* 23.5 (2015), pages 6803–6808. DOI: 10.1364/OE.24.013142.

[60] Sujoy Paul, Niels Heermeier, Mohammadreza Malekizandi, Julijan Cesar, Mohammad Tanvir Haidar, Christoph Gréus, Christian Neumeyr, and Franko Küppers. "10-Gbps Direct On-Off-Keying Modulation across 85-nm Continuous Tuning Range Using Telecom MEMS-VCSEL". In: *Conference on Lasers & Electro-Optics / Europe and the European Quantum Electronics Conference*. Munich, Germany, 2017. DOI: 10.1109/CLEOE-EQEC.2017.8086351.

[61] Sujoy Paul, Vladimir S Lyubopytov, Martin F Schumann, Julijan Cesar, Arkadi Chipouline, Martin Wegener, and Franko Küppers. "Wavelength-selective orbital-angular-momentum beam generation using MEMS tunable Fabry-Perot filter". In: *Optics Letters* (2016), pages 3–6. DOI: 10.1364/OL.41.003249.

[62] Sujoy Paul, Vladimir Lyubopytov, Arkadi Chipouline, Martin Schumann, Julijan Cesar, Mohammadreza Malekizandi, Mohammad Tanvir Haidar, Martin Wegener, and Frank Küppers. "Vortex-MEMS filters for wavelength-selective orbital-angular-momentum beam generation". In: *SPIE Photonics West*. San Francisco, USA, 2017. DOI: 10.1117/12.2252494.

[74] Christoph Wagner, Annika Dochhan, Michael Eiselt, Klaus Grobe, Markus Ortsiefer, Christoph Gréus, Christian Neumeyr, Sujoy Paul, Julijan Cesar, Franko Küppers, Vegas Olmos, Juan Jose, and Idelfonso Tafur Monroy. "26-Gbps DMT Transmission using Full C-band Tunable VCSEL for Converged PONs". In: *IEEE Photonics Technology Letters* (2017). DOI: 10.1109/LPT.2017.2710323.

[75] Christoph Wagner, Jim Zou, Markus Ortsiefer, Christoph Greus, Chritian Neumayr, Klaus Grobe, Michael Eiselt, Sujoy Paul, Julijan Cesar, Franko Küppers, Juan Jose Vegas Olmos, and Idelfonso Tafur Monroy. "Full C-band Tunable MEMS-VCSEL for Next Generation G.metro Mobile Front- and Backhauling". In: *Optical Fiber Communication Conference*. Los Angeles, USA, 2017. DOI: 10.1364/OFC.2017.W2A.27.

Supervised Theses

- Bachelor Thesis Stipo Matić: "Herstellung und Charakterisierung von abstimmbaren SiC-MEMS-DBR optischen Filtern bei 1550 nm"
- Bachelor Thesis Fouad Tajjiou: "Wavelength selective photoreceivers based on tunable SiN and SiC-MEMS-DBR technology"

A Chemical Reactions

In this chapter an overview of chemical reactions is given for all wet- and dry-etching recipes used in this thesis.

Depositions

- SiO_x is deposited in a PECVD chamber using silane (SiH_4) and nitrous oxide (N_2O) as precursors and sources for Si and O, respectively. The reaction is as follows.

  $$SiH_4 + 4\,N_2O \longrightarrow SiO_2 + 2\,H_2O + 4\,N_2$$

  Additionally He as carrier gas and is provided in the chamber to reduce plasma energies required for ignition.

- SiN_y is deposited in a PECVD chamber using silane (SiH_4) and nitrogen (N_2) accompanied by He.

  $$3\,SiH_4 + 5\,N_2 \longrightarrow Si_3N_4 + 3\,N_2H_4$$

  Hydrazine (N_2H_4) is gaseous and can be removed by pumping.

- SiC_z is deposited in a PECVD chamber using silane (SiH_4) and methane (CH_4) accompanied by He and Ar carrier gases.

  $$SiH_4 + 4\,CH_4 \longrightarrow SiC_4 + 10\,H_2$$

Wet-Chemical Reactions

The following reactions take place at room temperature if not stated otherwise.

- Etching of **Chromium** with ceric ammonium nitrate solved in perchloric acid ($HClO_4$) which chemically stabilizes it [37, 46].

$$3\,(NH_4)_2Ce(NO_3)_6 + Cr \longrightarrow Cr(NO_3)_3 + 3\,(NH_4)_2Ce(NO_3)_5$$

  Cerium oxidation state is reduced from IV to II, while chromium oxidization increases from II to III. During etching a dark film on the chromium surface is produced. Due to its aqueous solubility it is dissolved in the etchant. Au, Ni and Al are not etched by this solution. Chromium can be etched with a O_2/Cl_2-plasma, which makes it suitable as etch mask during fluorine-based DBR dry-etching [46].

- Etching of **Nickel** is possible with several etchants, like nitric acid (HNO_3), acetic acid ($C_2H_4O_2$ or CH_3OOH_2), iron(III) chloride ($FeCl_3$), sulfuric acid (H_2SO_4) and hydrofluoric acid (HF) as well as mixtures of those [2]. In general etching Ni is a two step process where it is first oxidized and then the oxide is removed [48]. In the following a reaction is shown where nickel nitrate ($Ni(NO_3)_2$) is created with nitric acid diluted in water [70].

$$3\,Ni + 8\,HNO_3 \longrightarrow 3\,Ni(NO_3)_2 + 2\,NO + 4\,H_2O$$

  Nickel nitrate can then be hydrated by water forming $Ni(NO_3)_2 \cdot 6\,H_2O$ which is soluble in water and transported from the sample surface through stirring. To increase the etching rate the solution is heated to 50 °C. Like Cr, Ni is not etched by fluorine-based etchants and is thus suitable as a DBR dry-etching mask.

- Etching of **Gold** with iodine [47].

$$2\,Au + I_2 \longrightarrow 2\,AuI$$

  To improve solubility gold iodide (KI) is added. Moreover, Au can be etched with a mixture of nitric acid (HNO_3) and hydrochloric acid (HCl) where Cl radicals keep Au dissolved [47].

$$HNO_3 + 3\,HCl \longrightarrow NOCl + 2\,Cl + 2\,H_2O$$

  Due to the instability of the mixture and decomposition by formation of nitrogen oxides and Cl_2 the first solution based on iodine is preferred. Dry etching of Au can be performed with Cl or CF_4/CCl_4 plasmas as well as with Ar bombardment [37].

- Silicon oxide (SiO_x) can be wet etched with hydrofluoric acid (HF) [49].

$$SiO_2 + 4\,HF \longrightarrow SiF_4 + 2\,H_2O$$

  Since this reaction consumes a lot of fluoride atoms the etchant is buffered with ammonium fluoride (NH_4F) releasing F^- ions which can react by themselves or create highly reactive HF_2^- ions.

$$NH_4F + H_2O \longrightarrow H_2O^+ + F^- + NH_3$$

  Dry-etching options are presented in appendix A.

Dry-Etching Reactions

The dry-etching method is used to structure dielectric DBR materials.

- Silicon oxide (SiO_x) can be dry-etched in a RIE chamber with fluoroform (CHF_3). Moreover tetrafluoromethane (CF_4) plasma and mixtures of both are listed [37]. Additionally oxygen (O_2) is required so all resulting molecules are in a gaseous state which can be removed by pumping. A simplified overview of the reactions for SiO_2 is shown in the following three lines [67]

$$\begin{aligned} CF_4 &\longrightarrow 2\,F + CF_2 \\ SiO_2 + 4\,F + O_2 &\longrightarrow SiF_4 + 2\,O \\ SiO_2 + 2\,CF_2 &\longrightarrow SiF_4 + 2\,CO \end{aligned}$$

  The resulting molecules are silicon tetrafluoride (SiF_4), carbon monoxide (CO) and oxygen all of which are gaseous.

- Silicon nitride (SiN_y) can be dry-etched in fluoroform/oxygen (CHF_3/O_2), tetrafluoromethane (CF_4) as well as in hexafluorethane (C_2F_6) plasma [39, 38]. The reaction takes place similarly to the dry-etching of SiO_x. Additionally reactions of CHF_3 are considered [28].

$$\begin{aligned} CF_4 &\longrightarrow 2\,F + CF_2 \\ 2\,CHF_3 &\longrightarrow 2\,CF_2 + 2\,H + 2\,F \\ Si_3N_4 + 6\,CF_2 + 6\,O_2 &\longrightarrow 3\,SiF_4 + 6\,CO_2 + 2\,N_2 \\ Si_3N_4 + 12\,F &\longrightarrow 3\,SiF_4 + 2\,N_2 \\ 4\,H + N_2 &\longrightarrow N_2H_4 \end{aligned}$$

  All resulting molecules are gaseous and can be removed by pumping.

- Silicon carbide (SiC_z) can be etched with a fluoroform/oxygen ($CHF_3Ø_2$) plasma [37]. Further combinations include sulfur hexafluoride/oxygen (SF_6/O_2) and bromtrifluoromethane/oxygen ($CBrF_3/O_2$) plasmas.

$$\begin{aligned} CHF_3 &\longrightarrow CF_2 + H + F \\ SiC_4 + 2\,CF_2 + 8\,O_2 &\longrightarrow SiF_4 + 8\,CO_2 \\ SiC_4 + 4\,F + 4\,H &\longrightarrow SiF_4 + 2\,CH_4 \end{aligned}$$

B Additional Graphs

This section shows two further graphs, looking at the reflectivities of SiO_x-SiC_z-DBRs in comparison to SiO_x-SiN_y-DBRs.

Figure B.1 presents the calculated values (TMM) for a perpendicular incidence. A higher number of layer pairs increases the maximum reflectivity, but does not influence the stopband width considerably. An added extinction coefficient for SiC_z layer according to findings from fig. 3.1 reduces the reflectivity by a large amount and is thus responsible for many results, especially for the performance of photodiode and VCSEL devices.

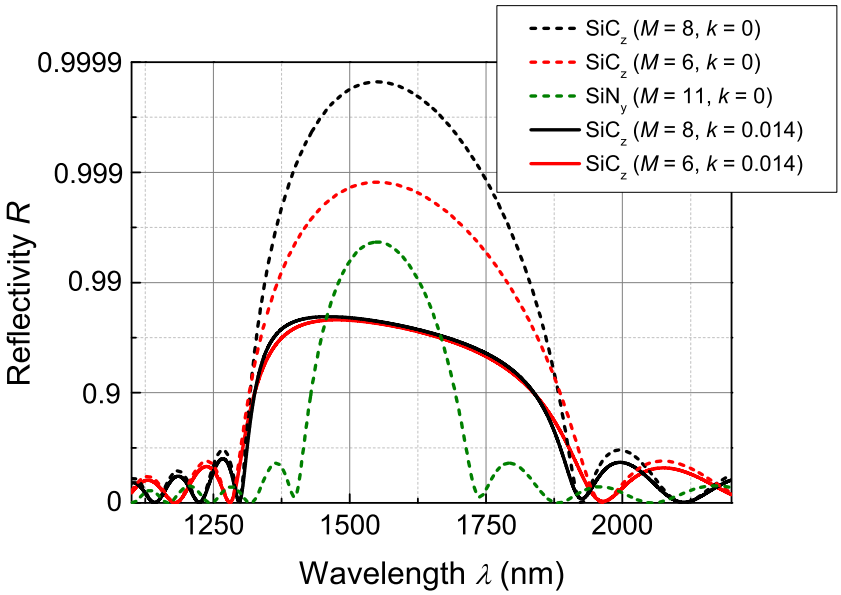

Figure B.1: TMM calculations for SiO_x-SiC_z and SiO_x-SiN_y DBRs on a Si substrate at perpendicular incidence for different numbers of layer pairs M and extinction coefficients k.

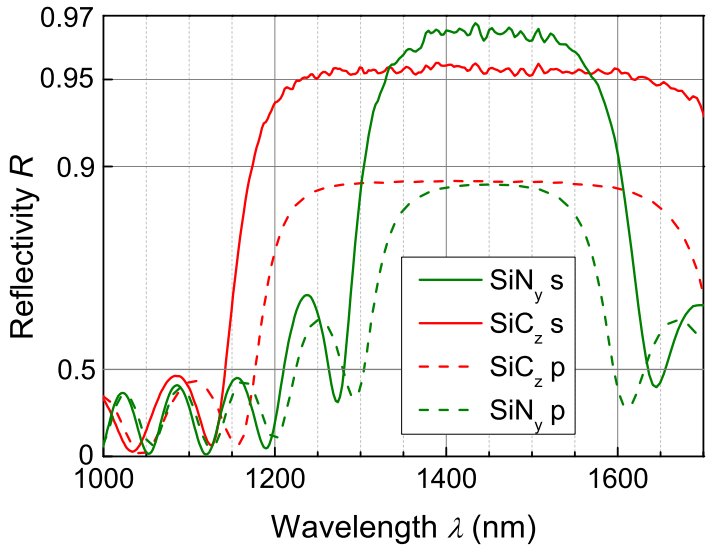

Figure B.2: Measured SiO_x-SiC_z and SiO_x-SiN_y DBR reflectivities on a Si substrate (ellipsometer) at an incidence angle of 40° for s- and p-polarization.

Figure B.2 shows ellipsometry measurements of SiO_x-SiN_y and SiO_x-SiC_z DBRs grown on a Si substrate. Here, the incidence angle is 40° and the maximum wavelength is 1700 nm, both limited by the setup. The s- and p-polarizations differ mainly due to the non-perpendicular incidence. The maximum reflectivity for the SiO_x-SiN_y-DBR ($M = 11$) is higher than for SiO_x-SiC_z-DBR ($M = 6$) corresponding to the findings in fig. B.1. Although each layer of both DBRs has an optical thickness of 1550/4 nm the center-wavelength is blue-shifted because of the incidence angle. Since ellipsometry is not an ideal way to measure very high reflectivities, the absolute values should be disregarded at this point. Only the comparison between the curves is possible here. Moreover the ripples around the centers of the curves probably comes from light source instabilities and should also be omitted here.

C Photolithography Masks

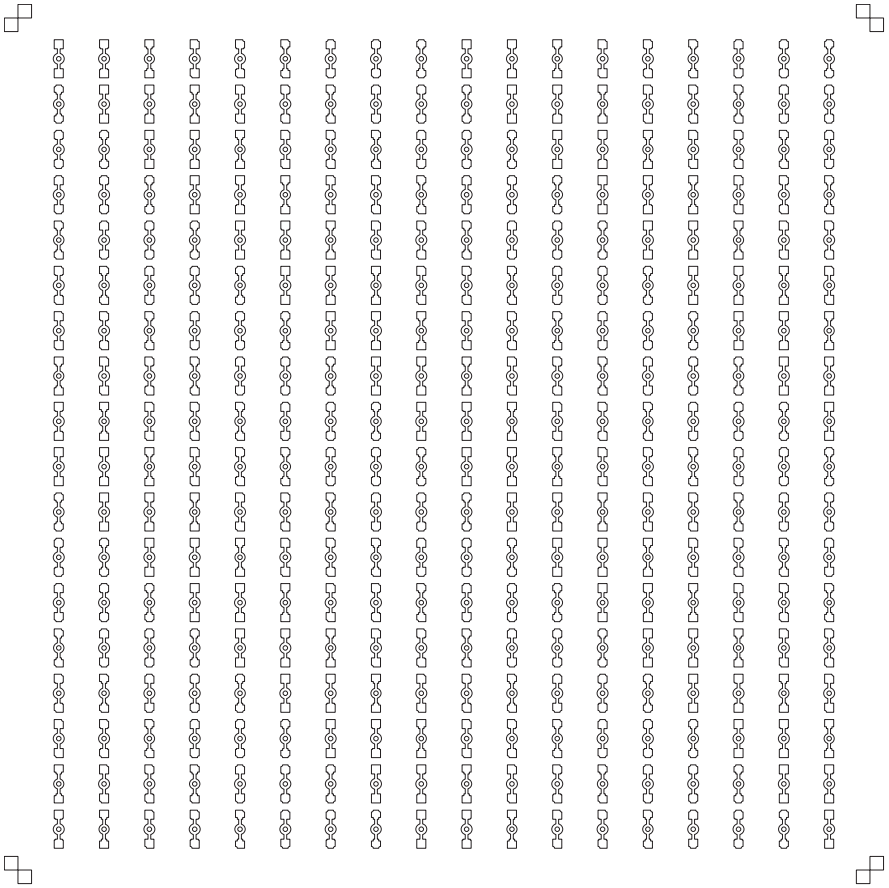

Figure C.1: Photolithography mask design for bottom electrode.

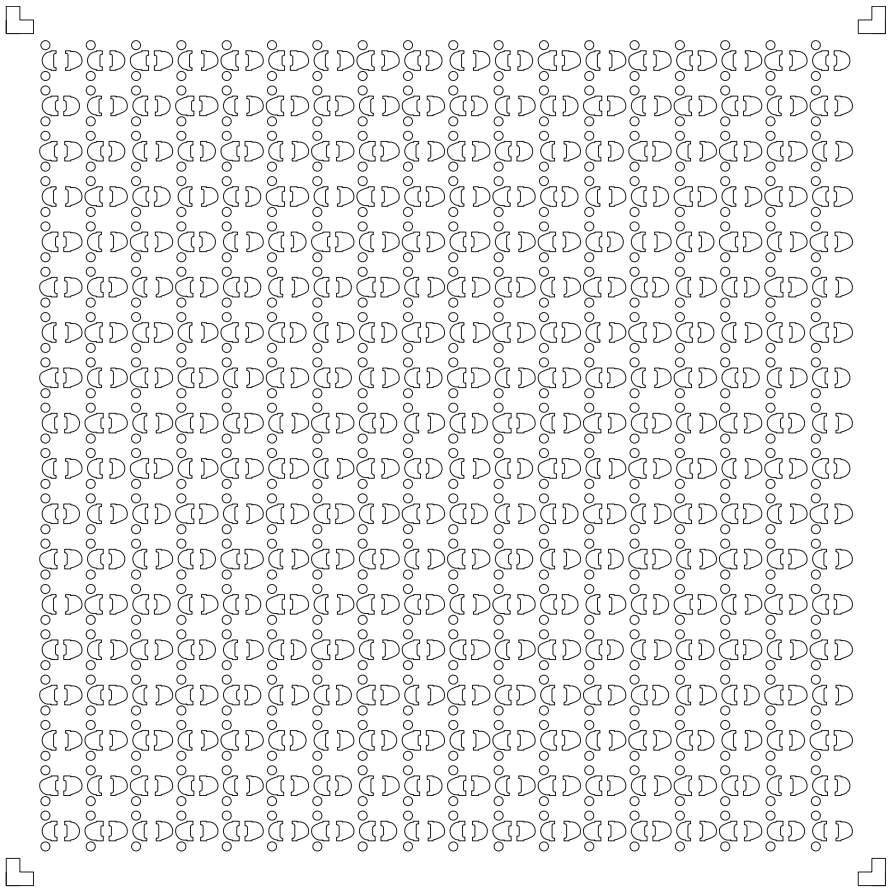

Figure C.2: Photolithography mask design inverse sacrificial layer.

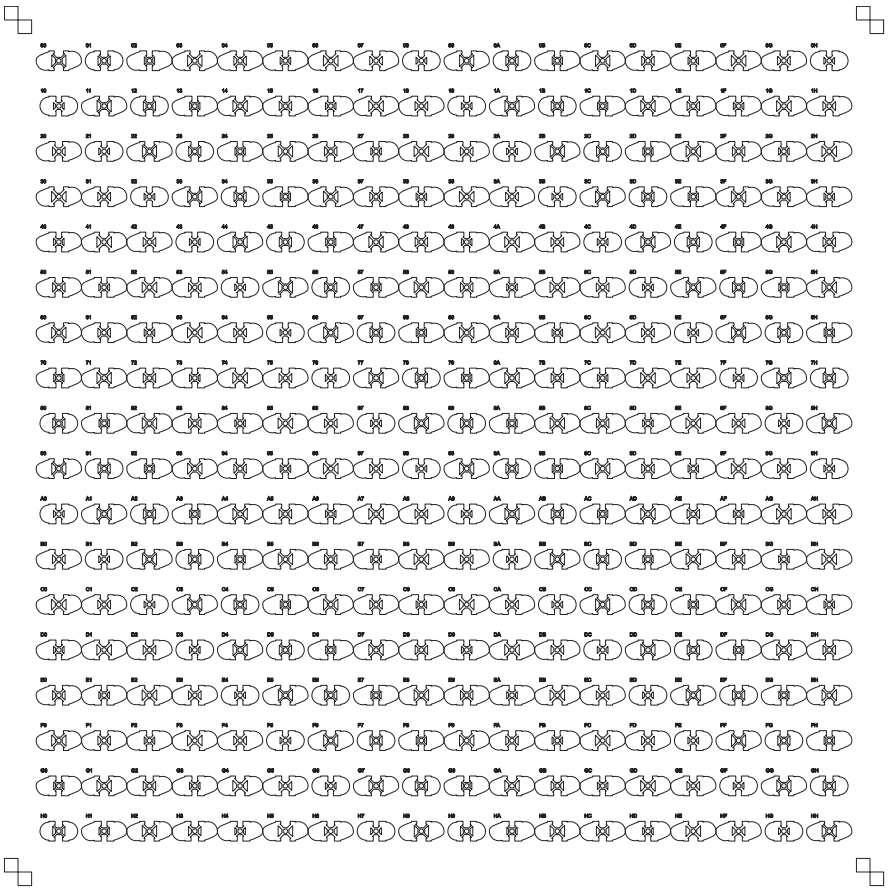

Figure C.3: Photolithography mask design for top electrode with numbering.

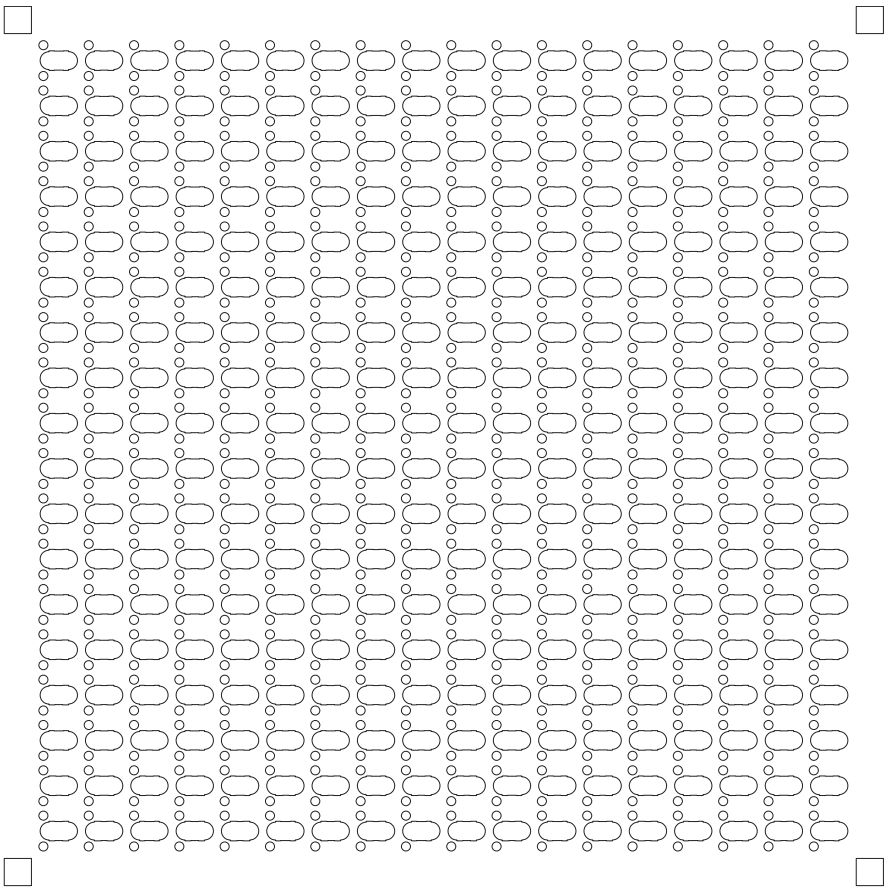

Figure C.4: Photolithography mask design for PD contact protection.

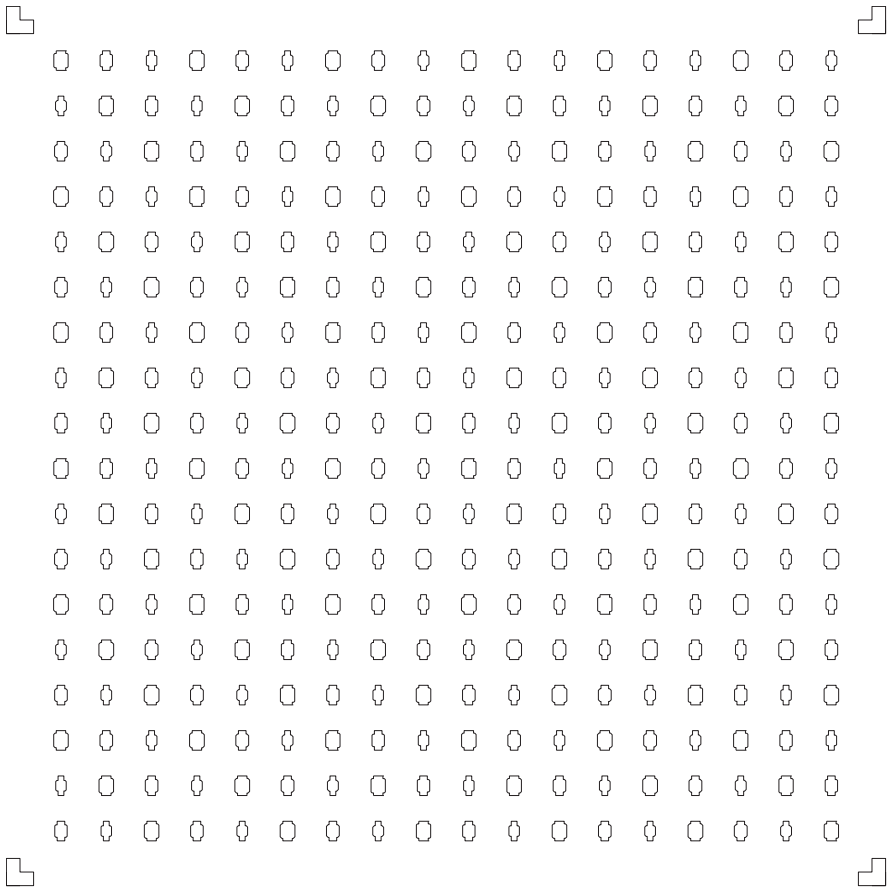

Figure C.5: Photolithography mask design for sacrificial layer.

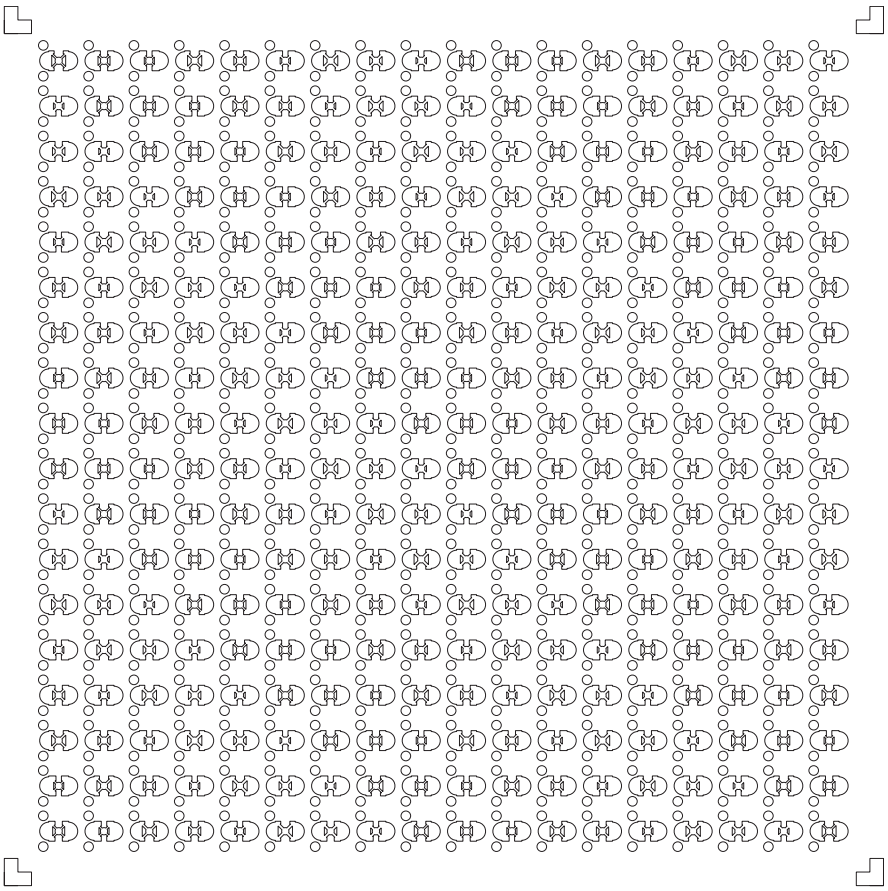

Figure C.6: Photolithography mask design for MEMS etching.